

Approved for public  
distribution unlimited.

AD-A186 105

AFOSR-TR. 87-1261

Absorption, Scattering, and Thermal  
Radiation by Conductive Fibers

DTIC FILE COPY

Final Report

Contract No. F49620-84-C-0045

Prepared by

N. E. Pedersen  
P. C. Waterman  
J. C. Pedersen

July 16, 1987

DISTRIBUTION STATEMENT A

Approved for public release  
Distribution Unlimited

Panametrics, Inc.  
221 Crescent Street  
Waltham, Massachusetts 02254

Submitted to

Major Joseph Hager  
Air Force Office of Scientific Research/NE  
Directorate of Electronic and Material Sciences  
Spacecraft Survivability Program  
Building 410  
Bolling Air Force Base, DC 20332-6448

2  
AIR FORCE OFFICE OF SCIENTIFIC RESEARCH (AFOSR)  
OFFICE OF TRANSDUCERS  
Technical report  
Approved for public release  
Distribution is unlimited  
MATTHEW J. KERR  
Chief, Technical Information Division

DTIC  
ELECTE  
OCT 13 1987  
S D

## REPORT DOCUMENTATION PAGE

1a. REPORT SECURITY CLASSIFICATION <b>UNCLASSIFIED</b>		1b. RESTRICTIVE MARKINGS													
2a. SECURITY CLASSIFICATION OF ABSTRACT <b>UNCLASSIFIED</b>		3. DISTRIBUTION/AVAILABILITY OF REPORT Approved for public release, distribution unlimited													
2b. DECLASSIFICATION/CONTROLLING SKEDON															
4. PERFORMING ORGANIZATION REPORT NUMBER <b>DTIC ELECTE</b> <b>S</b> <b>D</b> <b>B</b>		5. MONITORING ORGANIZATION REPORT NUMBER(S) <b>AFOSR-TR- 87-1261</b>													
6a. NAME OF PERFORMING ORGANIZATION Panametrics Inc		6b. OFFICE SYMBOL (If applicable)													
6c. ADDRESS (City, State and ZIP Code) 221 Crescent Street Waltham, MA 02254		7a. ADDRESS (City, State and ZIP Code) Bldg 410 Bolling AFB, DC 20332-6448													
8a. NAME OF FUNDING/SPONSORING ORGANIZATION AFOSR		8b. OFFICE SYMBOL (If applicable) NE													
8c. ADDRESS (City, State and ZIP Code) Bldg 410 Bolling AFB, DC 20332-6448		9. PROCUREMENT INSTRUMENT IDENTIFICATION NUMBER F49620-84-C-0045													
11. TITLE (Include Security Classification) Absorption, Scattering, and Thermal Radiation by Conductive Fibers		10. SOURCE OF FUNDING NOS. <table border="1"><tr><th>PROGRAM ELEMENT NO.</th><th>PROJECT NO.</th><th>TASK NO.</th><th>WORK UNIT NO.</th></tr><tr><td>61102F</td><td>2306</td><td>C4</td><td></td></tr></table>		PROGRAM ELEMENT NO.	PROJECT NO.	TASK NO.	WORK UNIT NO.	61102F	2306	C4					
PROGRAM ELEMENT NO.	PROJECT NO.	TASK NO.	WORK UNIT NO.												
61102F	2306	C4													
12. PERSONAL AUTHOR(S) Dr. Pedersen															
13a. TYPE OF REPORT Final Report	13b. TIME COVERED FROM 16May84 to 15Jan87	14. DATE OF REPORT (Yr., Mo., Day) 16 July 87	15. PAGE COUNT 115												
16. SUPPLEMENTARY NOTATION															
17. COSATI CODES <table border="1"><tr><th>FIELD</th><th>GROUP</th><th>SUB GR.</th></tr><tr><td></td><td></td><td></td></tr><tr><td></td><td></td><td></td></tr><tr><td></td><td></td><td></td></tr></table>		FIELD	GROUP	SUB GR.										18. SUBJECT TERMS (Continue on reverse if necessary and identify by block number)	
FIELD	GROUP	SUB GR.													
19. ABSTRACT (Continue on reverse if necessary and identify by block number) The present authors have studied the scattering of electromagnetic waves using variational method. Thus, that the work can be regarded as an extension of the work Tai and Cassedy and Fainberg to include both finite conductivity and arbitrary angle of incidence. Differential scattering patterns are then computed, along with the scattering, absorption and extinction. These cross sections are obtained by integrating the normal component of the Poynting vector over the surface of the fiber, enabling us to avoid the integration over the far-field sphere usually employed to compute scattering. In addition, it is found that energy considerations are exactly satisfied: the extinction cross section, which by the optical theorem must equal the imaginary part of the forward amplitude, is identically equal to the sum of the absorption and scattering cross sections. This result is particularly valuable for those applications in which we study the scattering and absorption properties of the cloud of such fiber particles.															
20. DISTRIBUTION/AVAILABILITY OF ABSTRACT UNCLASSIFIED/UNLIMITED <input checked="" type="checkbox"/> SAME AS RPT. <input type="checkbox"/> DTIC USERS <input type="checkbox"/>		21. ABSTRACT SECURITY CLASSIFICATION <b>UNCLASSIFIED</b>													
22a. NAME OF RESPONSIBLE INDIVIDUAL Major Hager		22b. TELEPHONE NUMBER (Include Area Code) (202) 767-4933	22c. OFFICE SYMBOL NE												

## FOREWORD

The formal purpose of this report is to address the Statement of Work of Contract No. F49620-84-C-0045. Considerable additional effort has been expended in Section I to provide a comprehensive presentation of our most recent theoretical results in electromagnetic scattering and absorption. Since this work encompasses over 20 years of effort (see for example, N.E. Pedersen, J.C. Pedersen, H.A. Bethe, "A New Method of Radar Target Concealment," Proc. Tri-Services Radar Symposium, San Diego, 1969), it has not been possible to include many topics, such as comparison of backscatter predictions with experimental results.

In Section II we address the question of electromagnetic absorption and subsequent thermal radiation by very small particles. As in Section I, we have attempted to provide a comprehensive treatment of this subject. The material presented, together with that in the cited references, permits the solution of a wide range of related problems.

During the course of the program, a Hewlett Packard Model 9000/520 computer was provided by AFOSR. Without the use of this fast machine, a large fraction of the computations presented herein would not have been possible. It is presently being used in conjunction with other DoD programs, including AFOSR. We are very grateful for this contribution by AFOSR, and believe that it has contributed greatly to DoD and to our ultimate understanding of many of the phenomena with which we have been dealing.



Accession For	
NTIS CRA&I	<input checked="checked" type="checkbox"/>
DTIC TAB	<input type="checkbox"/>
Unannounced	<input type="checkbox"/>
Justification	
By	
Distribution /	
Assembly Codes	
Dist	Availability for
A-1	

# TABLE OF CONTENTS

	<u>Page</u>
<b>FOREWORD</b>	i
<b>LIST OF ILLUSTRATIONS</b>	iv
<b>LIST OF TABLES</b>	viii
 <b>SECTION I. ELECTROMAGNETIC THEORY</b>	 1
1.1 Introduction	1
1.2 Theory	4
1.3 Quasistatic Model	12
1.4 The Drude Model	15
1.5 The Reduced Conductivity	18
1.6 Numerical Results for Graphite and Iron	20
1.7 Radiative Transfer in Fiber Clouds	35
 <b>SECTION II. THERMAL RADIATION BY SMALL PARTICLES</b>	 43
2.1 Introduction	43
2.2 Classical Radiation Theory	44
2.3 Microscopic Particles	47
2.4 Interpretation	50
2.5 Computational Procedure	53
2.6 Results	55
2.6.1 Graphite	56
2.6.2 Iron	68
2.7 Applications	72
2.7.1 Geometrical Considerations	72
2.7.2 Aggregates of Absorbing Particles: Internally Heated Spherical and Cylindrical Clouds	75
Cylindrical Cloud; External Illumination	77
Slab Geometry; External Illumination	78

## TABLE OF CONTENTS (Cont'd)

	<u>Page</u>
Incident Electromagnetic Pulse	79
Vaporization and Melting	80
Ionization	80
Required Total Mass	81
2.8 Comments	82
 APPENDIX A - SCATTERING BY CURVED CONDUCTIVE FIBERS	 84
Preliminary Survey	84
The Integral Equation	86
Approximation for Special Fibers	94
 APPENDIX B - TARGET OBSCURATION	 96
 APPENDIX C - TAILORING OF PARTICLE PARAMETERS FOR SPECIFIC APPLICATIONS	 100
Constitutive Equations	102
Absorb at 3 cm, Reflect at 300 microns	103
Absorb at 3 cm, Absorb at 300 microns	107
Reflecting Modes	110
Transparent at 3 cm, Absorb at 300 Microns	111
Comments Relative to Particle Parameter Tailoring	113
 REFERENCES	 114

# LIST OF ILLUSTRATIONS

<u>Figure</u>		<u>Page</u>
1-1	Geometry is shown for a conducting fiber of length $2h$ and diameter $2a$ .	8
1-2	Differential scattering pattern is shown vs. scattering angle for a graphite fiber (normal incidence).	21
1-3	Differential scattering pattern is shown vs. scattering angle for a graphite fiber (incidence at 60 deg. from the axis).	21
1-4	Differential scattering pattern is shown vs. scattering angle for a graphite fiber (incidence at 30 deg. from the axis).	23
1-5	Log-log plot is given of the cross sections vs. wavelength for a graphite fiber (length 100 microns).	23
1-6	Log-log plot is given of the cross sections vs. wavelength for a graphite fiber (length 1000 microns).	24
1-7	Log-log plot is given of the absorption cross section vs. wavelength for a graphite fiber, comparing the variational result with the EQS and infinite cylinder approximations.	24
1-8	Log-log plot is given of the absorption cross section vs. wavelength for a graphite fiber, comparing the variational result with the EQS and infinite cylinder approximations.	26
1-9	Differential scattering pattern is shown vs. scattering angle for an iron fiber (normal incidence).	26
1-10	Differential scattering pattern is shown vs. scattering angle for an iron fiber (incidence at 60 deg. from the axis).	27
1-11	Differential scattering pattern is shown vs. scattering angle for an iron fiber (incidence at 30 deg. from the axis).	27
1-12	Log-log plot is given of the cross sections vs. wavelength for an iron fiber of length 5 microns (dashed curves are quasistatic approximations).	29

# LIST OF ILLUSTRATIONS (Cont'd)

<u>Figure</u>		<u>Page</u>
1-13	Log-log plot is given of the cross sections vs. wavelength for an iron fiber of length 10 microns (dashed curves are quasistatic approximations).	29
1-14	Log-log plot is given of the cross sections vs. wavelength for an iron fiber of length 100 microns (dashed curves are quasistatic approximations).	31
1-15	Log-log plot is given of the absorption cross section vs. wavelength for an iron fiber, comparing the variational result with the EQS and infinite cylinder approximations.	31
1-16	Log-log plot is given of the absorption cross section vs. wavelength for an iron fiber, comparing the variational result with the EQS and infinite cylinder approximations.	32
1-17	The reflected and transmitted intensities are plotted vs. $\cos \theta$ ( $\theta$ is the scattering angle) for a cloud of graphite fibers of optical depth 0.5.	37
1-18	The reflected and transmitted intensities are plotted vs. $\cos \theta$ ( $\theta$ is the scattering angle) for a cloud of graphite fibers of optical depth 1.	37
1-19	The reflected and transmitted intensities are plotted vs. $\cos \theta$ ( $\theta$ is the scattering angle) for a cloud of graphite fibers of optical depth 2.	38
1-20	The reflected and transmitted intensities are plotted vs. $\cos \theta$ ( $\theta$ is the scattering angle) for a cloud of graphite fibers of optical depth 4.	38
1-21	The reflected and transmitted intensities are plotted vs. $\cos \theta$ ( $\theta$ is the scattering angle) for a cloud of iron fibers of optical depth 0.5.	40
1-22	The reflected and transmitted intensities are plotted vs. $\cos \theta$ ( $\theta$ is the scattering angle) for a cloud of iron fibers of optical depth 1.	40

# LIST OF ILLUSTRATIONS (Cont'd)

<u>Figure</u>		<u>Page</u>
1-23	The reflected and transmitted intensities are plotted vs. $\cos \theta$ ( $\theta$ is the scattering angle) for a cloud of iron fibers of optical depth 2.	41
1-24	The reflected and transmitted intensities are plotted vs. $\cos \theta$ ( $\theta$ is the scattering angle) for a cloud of iron fibers of optical depth 4.	41
2-1	Absorption efficiency factor vs. wavelength for a 100 Angstrom radius graphite fiber.	58
2-2	Plots of $T_{\text{eff}}$ vs. $I_0$ from Table 2-1. $\lambda_0 = 10.6$ microns.	58
2-3	Radiant emittance of the 100 Angstrom radius graphite fiber. Effective radiating temperature = 2500 deg. K.	60
2-4	Radiant emittance of the 100 Angstrom radius graphite fiber. Effective radiating temperature = 1500 deg. K.	60
2-5	Radiant emittance of the 100 Angstrom radius graphite fiber. Effective radiating temperature = 1000 deg. K.	62
2-6	Radiant emittance of the 100 Angstrom radius graphite fiber. Effective radiating temperature = 500 deg. K.	62
2-7	Radiant emittance of the 100 Angstrom radius graphite fiber. Effective radiating temperature = 300 deg. K.	63
2-8	Absorption efficiency factor vs. wavelength for a 1 micron radius graphite fiber. Note the cusp at $\lambda = 5\mu$ .	65
2-9	Plots of $T_{\text{eff}}$ vs. $I_0$ for the 1 micron radius graphite fiber. $\lambda_0 = 10.7\mu$ .	65
2-10	Radiant emittance of the 1 micron radius graphite fiber. Effective radiating temperature = 2500 deg. K.	66
2-11	Radiant emittance of the 1 micron radius graphite fiber. Effective radiating temperature = 1000 deg. K.	66



# LIST OF ILLUSTRATIONS (Cont'd)

<u>Figure</u>		<u>Page</u>
2-12	Radiant emittance of the 1 micron radius graphite fiber. Effective radiating temperature = 500 deg. K.	67
2-13	Radiant emittance of the 1 micron radius graphite fiber. Effective radiating temperature = 300 deg. K.	67
2-14	Absorption efficiency factor vs. wavelength for a 100 Angstrom radius iron fiber.	69
2-15	Plot of $T_{eff}$ vs. $I_0$ for a 100 Angstrom iron fiber. $\lambda_0 = 10.6\mu$ .	69
2-16	Radiant emittance of the 100 Angstrom radius iron fiber. Effective radiating temperature = 1500 deg. K.	70
2-17	Radiant emittance of the 100 Angstrom radius iron fiber. Effective radiating temperature = 1000 deg. K.	70
2-18	Radiant emittance of the 100 Angstrom radius iron fiber. Effective radiating temperature = 500 deg. K.	71
2-19	Radiant emittance of the 100 Angstrom radius iron fiber. Effective radiating temperature = 300 deg. K.	71
A-1	Geometry of the Curved Fiber	88
C-1	An example of predominant absorption at $\lambda = 3$ cm and predominant scattering at 300 microns. $v$ = variational technique; e.q.s. = Extended Quasistatic Theory.	106
C-2	An example of broadband absorption at 3 cm and 300 microns. $v$ = variational technique; EQS = Extended Quasistatic Theory.	109
C-3	An example of transparency at 3 cm and predominant absorption at 300 microns.	112

# LIST OF TABLES

<u>Table</u>		<u>Page</u>
1-1	The mass of graphite or iron fibers required per square meter of cloud cross section for a 20 db reduction in signal strength (values in parenthesis may be underestimates; see text).	34
1-2	The fractions of (integrated) reflected and transmitted flux are given vs. optical depth for a cloud of graphite fibers (albedo = 0.65).	39
1-3	The fractions of (integrated) reflected and transmitted flux are given vs. optical depth for a cloud of iron fibers (albedo = 0.352).	42
2-1	Radiating temperature vs. incident intensity. Thin graphite fiber.	59

## SECTION I. ELECTROMAGNETIC THEORY

### 1.1 Introduction

The groundwork for the problem of scattering of electromagnetic waves by thin wires was laid by Pocklington<sup>1</sup>, and later Hallén<sup>2</sup>, who developed the governing integral equations. In 1947, the classic paper of Van Vleck, Bloch and Hamermesh presented extensive results for backscattering by perfectly conducting wires, using Hallén's equation.<sup>3</sup> Shortly after that, a variational method based on Pocklington's equation was described by Tai<sup>4</sup>, yielding results for the most part in agreement with those of Van Vleck et al. The variational technique was later extended to wires of finite conductivity by Cassedy and Fainberg, although they continued to consider only backscattering at normal incidence.<sup>5</sup>

In related work, a numerically-oriented solution of the Pocklington equation was carried out by Richmond for both perfectly conducting<sup>6</sup> and finite-conductivity<sup>7</sup> wires. A similar approach was taken by Medgyesi-Mitschang and Eftimia.<sup>8</sup> Applicability of a Wiener-Hopf technique was shown by Chen.<sup>9</sup> An interesting approach in terms of outgoing and reflected waves has been given by Shen, Wu and King, although only limited results are available.<sup>10</sup> Curved wires have also been considered, the circular loop by Kouyoumjian<sup>11</sup> and the more general case by Mei.<sup>12</sup> A good review of the literature is given by Rinarsson.<sup>13</sup>

The present authors have studied this problem in a series of

use the variational method, so that the work can be regarded as an extension of the work of Tai<sup>4</sup> and Cassedy and Fainberg<sup>5</sup> to include both finite conductivity and arbitrary angle of incidence. However, we find it more convenient to derive the basic equations in the context of Galerkin's method, which Jones has shown to be exactly equivalent.<sup>14</sup>

Differential scattering patterns are then computed, along with the scattering, absorption and extinction. These cross sections are obtained by integrating the normal component of the Poynting vector over the surface of the fiber, enabling us to avoid the integration over the far-field sphere usually employed to compute scattering. In addition, we find that energy considerations are exactly satisfied: the extinction cross section, which by the optical theorem must equal the imaginary part of the forward amplitude, is identically equal to the sum of the absorption and scattering cross sections. This result is particularly valuable for those applications in which we study the scattering and absorption properties of a cloud of such fiber particles.

Because of the approximate nature of the variational approach, it is important to back up the results by independent computations wherever possible, in addition to comparison with existing results. In the Rayleigh region, where fiber length is small compared to wavelength, electrostatic considerations would be expected to dominate. A quasistatic model is developed and checked against variational results. At high frequencies, on the other hand, the absorption cross section per unit length must

approach that of the infinitely long fiber. This latter quantity is computed, and agreement is seen to be good.

This work was originally begun for applications in the microwave region. In order that the computations may be extended into the infrared and visible regimes, it is vital to incorporate the optical properties of the fibers. We do this for applicable materials by employing the Drude model for conductivity (or complex dielectric constant), and include as well the dependence of conductivity on both fiber diameter and electron mean free path.

## 1.2 Theory

Consider the thin conductive fiber of radius  $a$  and half-length  $h$ , as shown in Fig. 1-1, having length to diameter ratio  $h/a \gg 1$ . An electromagnetic wave is incident along a direction making an angle  $\theta_i$  with the positive  $z$ -axis, as shown, and we suppose that the fiber radius is very small compared to incident wavelength, i.e.  $ka \ll 1$ , so that the resultant scattered wave has rotational symmetry.

With time-dependence factor  $\exp(-i\omega t)$  suppressed, the problem is described by the integral equation<sup>1, 2, 4, 5</sup>

$$\eta_s I(z) = E_i \sin \theta_i e^{ikz \cos \theta_i} + (ik\eta_0/4\pi) \int_{-h}^{+h} dz' I(z') K(z', z). \quad (1-1)$$

The left hand side of this equation expresses the axial component of the E-vector along the surface of the fiber in terms of an induced line current  $I(z)$  (equal to  $2\pi a$  times the induced surface current) and a surface impedance<sup>2, 5, 15</sup>

$$\eta_s = \frac{+i\omega\mu}{2\pi\kappa a} \frac{J_0(\kappa a)}{J_1(\kappa a)}, \quad (1-2)$$

where

$$\kappa = (\omega^2\mu\epsilon + i\omega\mu\sigma)^{1/2} \quad (1-3)$$

is the complex propagation constant within the fiber (we will assume free-space permeability, however) and  $J_0$ ,  $J_1$  are Bessel functions. It is also tacitly assumed that  $|\kappa/k|^2 \gg 1$ , so that

radial variations of the fields within the fiber are much more rapid than axial ones. The first term on the right hand side of Eq. (1-1) is simply the axial component of the incident E field. Finally, the integral term gives the E field contribution due to the induced current, where the kernel is given by

$$K(z', z) = (1 + \partial^2/k^2 \partial z^2) (1/2\pi) \int_0^{2\pi} d\theta' (1/R) e^{ikR}, \quad (1-4a)$$

$$R^2 = (z-z')^2 + 4a^2 \sin^2 (\theta'/2). \quad (1-4b)$$

The current is now written as a linear combination of the trial functions

$$e^{\pm ikz}, \quad e^{\pm ikz \cos \theta_i}. \quad (1-5)$$

Note that the first two of these represent resonant currents that can exist on the infinite, perfectly conducting fiber with no external field present<sup>1</sup>, and should continue to be appropriate for moderate to large conductivity. The term  $\exp(ikz \cos \theta_i)$  gives precisely the forced response of the infinite fiber regardless of the value of conductivity. Finally, the term  $\exp(-ikz \cos \theta_i)$  is included so that the trial functions can satisfy the boundary condition

$$I(\pm h) = 0 \quad (1-6)$$

of vanishing current at the ends of the fiber and still maintain some flexibility.

Following this prescription, the surface current takes the form

$$\begin{aligned}
 I(z) &= a_e f_e(z) + a_o f_o(z) \\
 &= a_e [\cos kz \cos (kh \cos \theta_i) - \cos kh \cos (kz \cos \theta_i)] \\
 &\quad + a_o [\sin kz \sin (kh \cos \theta_i) - \sin kh \sin (kz \cos \theta_i)]. \quad (1-7)
 \end{aligned}$$

In order to determine the coefficients by the Galerkin method, first substitute Eq. (1-7) into Eq. (1-1), then multiply separately by  $f_e(z)$  and  $f_o(z)$  and integrate over fiber length. From the two resulting equations one finds that

$$a_\sigma = \frac{4\pi i E_i}{k \eta_0} \frac{s_\sigma}{\gamma_\sigma - \lambda_\sigma}, \quad \sigma = e, o \text{ (even, odd)} \quad (1-8)$$

in terms of the (dimensionless) quantities

$$s_\sigma = k \sin \theta_i \int_{-h}^{+h} dz f_\sigma(z) e^{ikz \cos \theta_i}$$

$$\lambda_\sigma = -4\pi i (\eta_s / \eta_o) \int_{-h}^{+h} dz f_\sigma^2(z)$$



$$\gamma_{\sigma} = k \int_{-h}^{+h} dz f_{\sigma}(z) \int_{-h}^{+h} dz' f_{\sigma}(z') K(z', z) \quad (1-9)$$

for  $\sigma = e, o$ .

All of these integrals can be evaluated analytically under the approximation  $ka \ll 1$ ; the results are rather lengthy and we do not give them here. Note that some of these expressions were evaluated by Tai, for a somewhat simpler kernel.<sup>4, 13</sup> As noted earlier, the variational procedure used by Tai<sup>4</sup>, as well as Cassedy and Fainberg<sup>5</sup>, would give identical results.<sup>14</sup>

The scattered field can now be expressed as an integral of the induced current. For far-field scattering in the  $\theta$ -direction (see Fig. 1-1) one has<sup>13</sup>

$$\underline{E}_s = \hat{\theta} E_1 (1/kr) e^{ikr} S(\theta_1, \theta), \quad (1-10)$$

with far-field amplitude given by

$$S(\theta_1, \theta) = (k\eta_0/E_1) \sin \theta \int_{-h}^{+h} dz I(z) e^{-ikz \cos \theta}. \quad (1-11)$$

For the differential (or bistatic) cross section one has

$$\sigma_d = (4\pi/k^2) |S(\theta_1, \theta)|^2, \quad (1-12)$$

and similarly the backscattering or radar cross section is given by (again see Fig. 1-1)

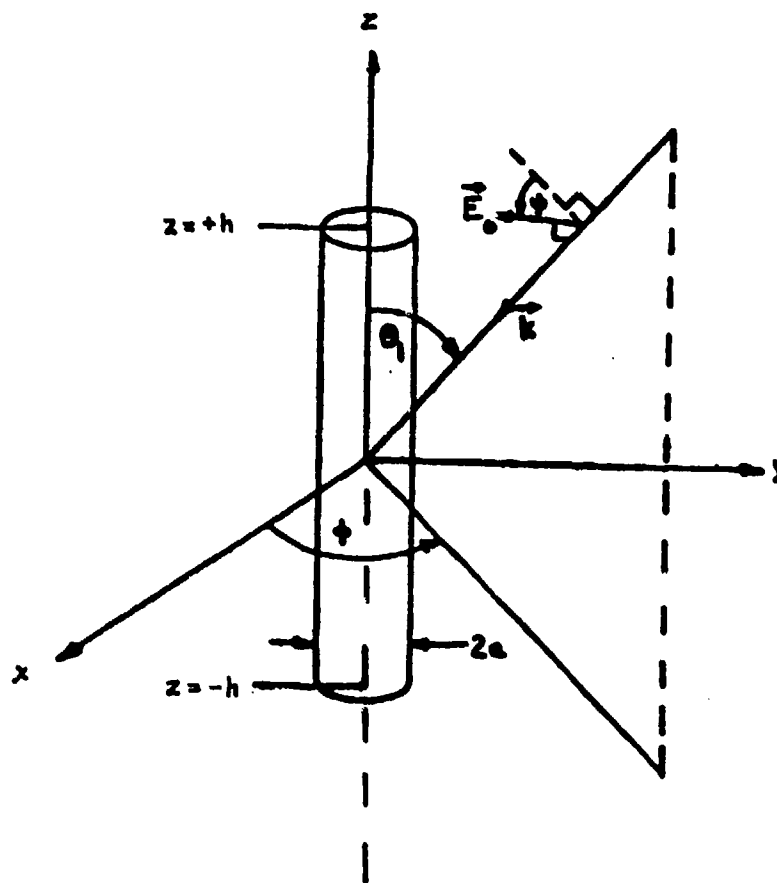


Figure 1-1. Geometry is shown for a conducting fiber of length  $2h$  and diameter  $2a$ .

$$\sigma_b = (4\pi/k^2) |S(\theta_i, \pi - \theta_i)|^2. \quad (1-13)$$

The remaining cross sections are most easily computed by integrating the normal component of the Poynting vector over the fiber surface, neglecting end surface contributions. For the scattered power one has

$$W_s = \frac{1}{2} \operatorname{Re} \int d\vec{S} \cdot (\vec{E}_s \times \vec{H}_s^*). \quad (1-14)$$

We are interested only in effects due to the  $x$ -component of  $\vec{E}_s$ , which is assumed independent of azimuth  $\phi$  because  $ka \ll 1$ . Consequently, only the  $\phi$ -component of  $\vec{H}_s$  is needed, and because the incident magnetic field  $\vec{H}_i$  varies as  $\cos \phi$  it will not contribute to the surface integral. We can thus replace  $\vec{H}_s$  by  $\vec{H} = \vec{H}_i + \vec{H}_s$ . If  $\vec{E}_s$  is also replaced by  $\vec{E} - \vec{E}_i$ , then Eq. (1-14) becomes

$$W_s = \frac{1}{2} \operatorname{Re} \int d\vec{S} \cdot (\vec{E} \times \vec{H}^*) - \frac{1}{2} \operatorname{Re} \int d\vec{S} \cdot (\vec{E}_i \times \vec{H}^*). \quad (1-15)$$

The first term on the right hand side gives total power flow into the fiber, and hence is the negative of the absorbed power. The second term is proportional to the real part of the forward amplitude, or the extinction cross section  $\sigma_e$ . Dividing each term by the incident energy flux density  $E_0^2/2\eta_0$  to get cross sections, Eq. (1-15) becomes

$$\sigma_e = (4\pi/k^2) \operatorname{Re} S(\theta_i, \theta_i) = \sigma_s + \sigma_a. \quad (1-16)$$

which is the optical theorem identifying the extinction cross section with the sum of the scattering and absorption cross sections.

From Eq. (1-14), again substituting for  $\underline{\underline{E}}_z$  as before (but not  $\underline{\underline{E}}_z$ ) and normalizing, one gets

$$\sigma_s = (\eta_0/E_0^2) \operatorname{Re} \int d\Omega \cdot (\underline{\underline{E}}_s \times \underline{\underline{H}}^*).$$

Now

$$d\Omega \cdot (\underline{\underline{E}}_s \times \underline{\underline{H}}^*) = (a \, d\theta dz) (\underline{\underline{E}}_s)_z \, \underline{\underline{H}}_\theta^*,$$

where  $(\underline{\underline{E}}_s)_z$  is given by the integral term of Eq. (1-1), and

$$\underline{\underline{H}}_\theta^* = (1/2\pi a) I^*(z).$$

Putting everything together, and making use of Eq. (1-8), the result is:

$$\sigma_s = \frac{-4\pi}{k^2} \operatorname{Im} \left[ \left| \frac{E_\theta}{\gamma_\theta - \lambda_\theta} \right|^2 \gamma_\theta + \left| \frac{E_\theta}{\gamma_\theta - \lambda_\theta} \right|^2 \gamma_\theta \right]. \quad (1-17)$$

One proceeds similarly with the first term on the right hand side of Eq. (1-15) to obtain the absorption cross section, noting that  $E_z = \eta_s I(z)$ , to get

$$\sigma_a = \frac{4\pi}{k^2} \operatorname{Im} \left[ \left| \frac{E_\theta}{\gamma_\theta - \lambda_\theta} \right|^2 \lambda_\theta + \left| \frac{E_\theta}{\gamma_\theta - \lambda_\theta} \right|^2 \lambda_\theta \right]. \quad (1-18)$$

Finally, in order to show explicitly that the extinction cross section is the sum of these last two expressions, note that the integrand in the last term of Eq. (1-15) may be written

$$d\tilde{E} \cdot (\tilde{E}_1 \times \tilde{E}^*) = (a d\theta dz) E_1 \sin \theta_1 e^{ikz \cos \theta_1} (1/2\pi a) I^*(z).$$

From Eq. (1-9), the  $z$ -integration is seen to involve only the  $s_\sigma$ , and with minor effort one gets

$$\sigma_0 = \frac{4\pi}{k^2} \operatorname{Im} \left[ \left| \frac{s_0}{\gamma_0 - \lambda_0} \right|^2 (\lambda_0 - \gamma_0) + \left| \frac{s_0}{\gamma_0 - \lambda_0} \right|^2 (\lambda_0 - \gamma_c) \right], \quad (1-19)$$

which by inspection is the sum of Eqs. (1-17) and (1-18).

For long fibers, a useful check is provided by computing the absorption cross section resulting from the infinite fiber solution. Again integrating the total field Poynting vector over the lateral surface  $4\pi ah$  of the fiber, using exact field quantities as given by Wait,<sup>16</sup> the rotationally symmetric portion of the field contributes

$$\sigma_a = -\eta_0 |A_0/E_1|^2 \operatorname{Re} [(ik/\omega\mu_0) J_0^*(ka) J_1(ka)] 4\pi ah \quad (1-20a)$$

where in the limit of interest to us

$$\begin{aligned} E_1 \sin \theta_1 / A_0 &\xrightarrow{ka \ll 1} J_0(ka) \\ &+ \sin^2 \theta_1 [\ln(ka \sin \theta_1 / 2) + \gamma + i\pi/2] ka J_1(ka) \end{aligned} \quad (1-20b)$$

with  $\gamma = 0.5772 \dots$  (Euler's constant). Comparisons using these formulas will be shown below.

### 1.3 Quasistatic Model

At low frequencies for which fiber dimensions are small compared with wavelength, an electrostatic treatment is appropriate. The electric field  $E$  inside the fiber, regarded as a Rayleigh particle, may be written

$$E = E_1 - L_4 \pi P, \quad (1-21)$$

where  $L$  is the depolarizing factor,  $P$  is the polarization, and  $E_1$  the homogeneous applied field along the axis. In the case of a long, thin spheroid, which should be a good approximation to the fiber in the present circumstances, the depolarizing factor is

$$L = (a/h)^2 [\ln (2h/a) - 1]. \quad (1-22)$$

The polarization is defined as

$$P = (1/4\pi) (\epsilon - 1) E, \quad (1-23)$$

where  $\epsilon$  is now the relative dielectric constant (normalized by dividing by  $\epsilon_0$ ). From Eqs. (1-21) and (1-23) one has for the internal field

$$E = \frac{E_1}{1 + L (\epsilon - 1)} \quad (1-24)$$

and if  $\epsilon$  is taken to be complex, i.e.,  $\epsilon = \epsilon' + i\epsilon''$ , then

$$E = E_i \left[ \frac{1 + L(\epsilon' - 1) - iL\epsilon''}{[1 + L(\epsilon' - 1)]^2 + (L\epsilon'')^2} \right] \quad (1-25)$$

Note that in the quasistatic approximation there is both an in-phase and a quadrature component of the internal field.

The electric dipole moment of the particle is defined as

$$p = PV_p \quad (1-26)$$

where  $V_p$  is particle volume; the polarizability  $\alpha$  is then defined in terms of the dipole moment by

$$p = \alpha E_i \quad (1-27)$$

From the preceding equations the desired expression for polarizability is given by

$$\alpha = \frac{V_p}{4\pi} \left[ \frac{(\epsilon' - 1) [1 + L(\epsilon' - 1)] + L\epsilon''^2 + i\epsilon''}{[1 + L(\epsilon' - 1)]^2 + (L\epsilon'')^2} \right] \quad (1-28)$$

The absorption and scattering cross sections are simply expressed in terms of  $\alpha$ ; one has, respectively,

$$\sigma_a = 4\pi k \operatorname{Im} \alpha, \quad (1-29)$$

$$\sigma_s = (8\pi/3) k^4 |\alpha|^2. \quad (1-30)$$

These equations have good theoretical justification within the range  $kh \lesssim \pi/2$ . When  $kh$  exceeds this limit, the effective value of the depolarizing factor in Eq. (1-22) is reduced. This is because the dipole field due to the induced charges at the ends of the particle is no longer strictly  $\pi$  out of phase with the applied field. In order to take this discrepancy into account, we have devised a modified depolarizing factor given by

$$L = \left[ \left( \frac{a}{h} \right)^2 + \left( \frac{ka}{\pi} \right)^2 \right] \left[ \ln \left( \frac{h}{a} \right) - 1 \right]. \quad (1-31)$$

At wavelengths for which  $kh > \pi$ , the depolarizing factor increases as  $k^2$ . This is consistent with our reasoning regarding the high frequency behavior of the incoherence of the depolarizing field. It is because of the inclusion of Eq. (1-31) that we refer to this theory as our Extended Quasistatic (EQS) theory. We should note that the factor  $(1/\pi)$  appearing in Eq. (1-31) was arrived at through many comparisons between the EQS and the Variational technique discussed in the previous subsection.

Although the above (EQS) theory is only approximate, it has the very useful properties of being simple and analytic. It can, therefore, be used to provide reasonable approximate predictions for cases of interest. However, such predictions (especially in the regime  $kh > 1$ ) should be ultimately refined using the variational technique. Comparative results will be shown subsequently in this report.



#### 1.4 The Drude Model

In order to apply the above results to the infrared and visible regions, as well as the microwave case, it is necessary to build in the optical behavior of the fibers. In this and the following section we deal with (1) the inclusion of the optical properties, and (2) inclusion of the dependence of electrical conductivity upon particle radius and electron mean free path, in both the Galerkin and quasistatic models.

In a recent paper by Ordal et al.<sup>17</sup>, the application of the Drude model for the prediction of complex optical dielectric constant was compared with measured values of the real and imaginary parts of the optical dielectric constant for a number of metals (Al, Cu, Au, Pb, Ag, and W). Tabular experimental results were also given for Fe, Pt, Co, Ni, Ti and Pd. This model, which is based on the free electron theory of metals, is in surprisingly good agreement with the observed experimental results. We realize that, for certain transition elements such as Fe, the model has drawbacks. For such cases, one must resort to the use of tabular experimental data.

For our present discussion, we choose Cu as the substance comprising our fibers, and will utilize the Drude model in the calculation of the various electromagnetic cross sections. A good exposition of this is given in Wooten's book,<sup>18</sup> in which the real and imaginary parts of the dielectric constant take the form

$$\epsilon' = 1 - \frac{\omega_p^2 \tau^2}{1 + (\omega\tau)^2} \quad (1-32)$$

$$\epsilon'' = \frac{\omega_p^2 \tau}{\omega [1 + (\omega\tau)^2]} \quad (1-33)$$

Using mks units, the plasma frequency  $\omega_p$  is given by

$$\omega_p^2 = ne^2/m\epsilon_0 \quad (1-34)$$

in which  $n$  = electron density ( $m^{-3}$ ),  $e$  = electronic charge,  $m$  = effective mass of the electron, and  $\epsilon_0$  = permittivity of free space =  $(1/36\pi) \times 10^{-9}$  farads/m.

The quantity  $\tau$  is the electron relaxation time, which is the time required for randomization of the momentum vector of an electron in the (metallic) lattice. For our purposes, it is instructive to cast the dielectric constant in terms of the low frequency electrical conductivity  $\sigma$ , given by

$$\sigma = ne^2\tau/m \quad (1-35)$$

Now  $\omega_p^2 = \sigma/\tau\epsilon_0$ , and Eqs. (1-32) and (1-33) may be written as

$$\epsilon' = 1 - \frac{\sigma\tau}{\epsilon_0} \left( \frac{1}{1 + (\omega\tau)^2} \right) \quad (1-36)$$

$$\epsilon'' = \frac{\sigma}{\omega\epsilon_0 [1 + (\omega\tau)^2]} \quad (1-37)$$

Typical values of the relaxation time  $\tau$  are on the order of  $10^{-14}$  sec.

It is easily shown that Eq. (1-36) can be written in terms of  $\epsilon''$ :

$$\epsilon' = 1 - \epsilon''(\omega\tau) \quad (1-38)$$

This equation shows that, for all frequencies significantly below the visible and infrared (i.e., the microwave region),  $|\epsilon'| \ll |\epsilon''|$ . Also, from Eq. (1-37), we see that  $\epsilon''$  goes to its low frequency value  $\epsilon'' = \sigma/\omega\epsilon_0$  for  $(\omega\tau)^2 \ll 1$ .

The reason for the above analysis is to determine whether or not the Drude model can be utilized at low frequencies. Although the low frequency value of  $\epsilon'$  differs significantly from a value of unity, which is normally assumed for metals, the ratio  $|\epsilon''/\epsilon'|$  will always be very large when  $(\omega\tau)^2 \ll 1$ . Therefore, the use of the Drude model throughout the region  $10^{-6} \text{ m} \leq \lambda_0 \leq 10^{-1} \text{ m}$  appears to be justified, and we feel confident in using Eqs. (36) and (37) in the derivation of the electromagnetic cross sections throughout this entire wavelength range for appropriate materials.

### 1.5 The Reduced Conductivity

When one or more dimensions of a conductive material (metal or semiconductor) are on the order of the mean free path of the conduction electrons, electron collisions with the surface will significantly reduce the mean free time, and hence the mean free path  $\Lambda$  given by

$$\Lambda = v_F \tau , \quad (1-39)$$

where  $v_F$  = Fermi velocity and  $\tau$  = relaxation time discussed previously. Since the electrical conductivity is proportional to  $\tau$  (see Eq. -35), the conductivity will also be reduced.

The classic work on this subject was done in 1938 by Fuchs.<sup>19</sup> In a more recent paper, Dingle reviews the subject and provides some useful numerical computations.<sup>20</sup> The key equation in Dingle's paper is his Eq. (2.3) which relates the effective conductivity  $\sigma$  to the bulk conductivity  $\sigma_0$ , as a function of mean free path, wire radius  $a$ , and the quantity  $\epsilon$  that is the probability of an elastic collision at the surface:

$$\sigma = \sigma_0 \left[ 1 - \frac{3}{8} (1 - \epsilon) \left( \frac{\Lambda}{a} \right) \right] . \quad (1-40)$$

A value of  $\epsilon = 1/2$  is frequently used as the surface scattering coefficient. Taking this, we have

$$\sigma = \sigma_0 \left[ 1 - \frac{3}{16} \left( \frac{\Lambda}{a} \right) \right] . \quad (1-41)$$

We have had difficulty in obtaining numerical values for mean free paths from the literature. However, Kittel<sup>21</sup> provides a good background as well as quantitative data for a number of metals. Taking copper as the subject material, a value of  $\lambda = 4.2 \times 10^{-8} \text{ m}$  is given in Table 10.1 of Kittel's book. Using Eq. (1-39), and taking the Fermi velocity  $v_F = 1.6 \times 10^6 \text{ m/sec}$ <sup>21</sup> one obtains a mean free time of  $\tau = 2.6 \times 10^{-14} \text{ sec}$ . This is in fairly good agreement with the accepted value  $\tau = 1.9 \times 10^{-14} \text{ sec}$ .

Utilizing the above value, one gets for copper

$$\sigma = \sigma_0 \left[ 1 - \frac{7.9 \times 10^{-9}}{a} \right] \quad (1-42)$$

where the radius  $a$  has the unit of meters. This equation shows that, if  $a = 1.6 \times 10^{-8} \text{ m}$  (160 Angstroms), the conductivity is roughly half its bulk value. If the radius is 0.1 micron, the conductivity is 92% of the bulk value. This exercise was done to show that, indeed, one must consider the particle size effect upon electrical conductivity, when computing absorptive and extinction properties of thin metallic fibers or films.

## 1.6 Numerical Results for Graphite and Iron

The preceding theory has been reduced to computer codes including graphical outputs, and some numerical results are presented here for the two cases of graphite and iron. It should be noted that, as part of our AFOSR contract, we have received a Hewlett Packard HP 9000 Mod. 520 computer, which is employed for all computations.

Considering first graphite, the sequence of operations is as follows: Taking a bulk conductivity of  $10^5$  mho/m and mean free path of  $1.4 \times 10^{-9}$  m, the reduced conductivity is obtained from Eq. (1-41) upon specifying the fiber radius. Using this result and further assuming an electron relaxation time of  $1.4 \times 10^{-15}$  sec., the complex optical dielectric constant is obtained as a function of frequency from Eqs. (1-36) and (1-37). The surface impedance of the fiber can now be computed from Eq. (1-2), at which point the scattering computations can be carried out.

Some typical E-plane differential scattering patterns for graphite are shown in Figs. 1-2 thru 1-4. The fiber has radius of one micron and length of 110 microns. The incident wavelength is 30 microns, so that  $kh = 12$  and the fiber is several wavelengths long. The angle of incidence ranges progressively from broadside to near end-on aspect in the three figures, and as one would expect a fairly large main lobe is seen in the forward direction in all cases, with much smaller side lobes in other directions.

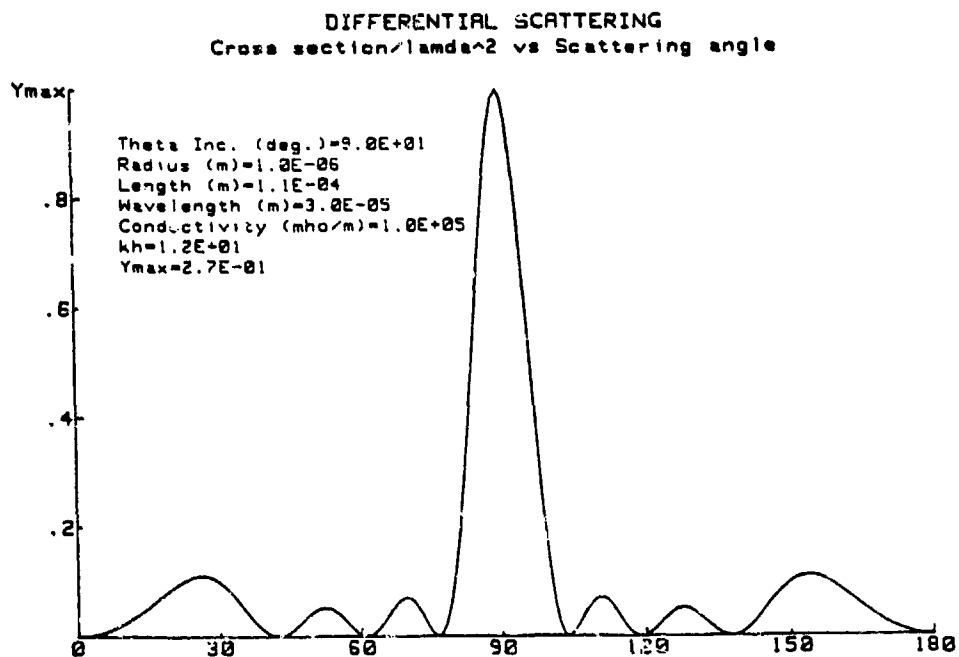


Figure 1-2. Differential scattering pattern is shown vs. scattering angle for a graphite fiber (normal incidence).

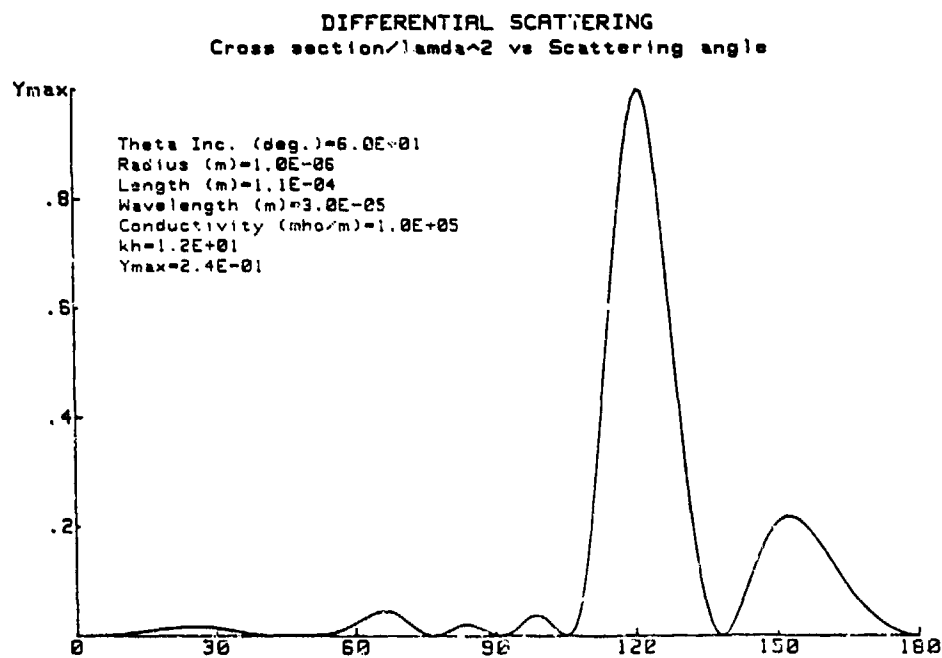


Figure 1-3. Differential scattering pattern is shown vs. scattering angle for a graphite fiber (incidence at 60 deg. from the axis).

The integrated cross sections (scattering, absorption and extinction) are shown for the same graphite fiber in Fig. 1-5, for wavelengths ranging from one micron up to 10 cm. It should be noted that we have done a planar-averaging (fiber axis in the plane formed by the incident and observation directions). The full random orientation results are obtained by reducing the curves in the figures by an additional 3 db. Note that the extinction cross section is precisely equal to the sum of the scattering and absorption cross sections at all wavelengths, as discussed earlier. Low frequency Rayleigh behavior,  $(1/\lambda)^4$  for the scattering and  $(1/\lambda)^2$  for the absorption, is clearly evident at the longer wavelengths. At short wavelengths, the scattering cross section becomes dominant.

The corresponding integrated cross sections for a graphite fiber slightly larger in diameter and about ten times longer are shown in Fig. 1-6 (see figure for precise dimensions). As one would expect, the peak values of all the cross sections now occur at wavelengths ten times greater, although the magnitudes of the peaks are virtually unchanged.

The different methods of computing absorption cross section are compared in Fig. 1-7 for a small graphite fiber (radius = 0.02 microns, length = 16 microns). The Galerkin (or variational) results correspond to the curve with oscillations at the shorter wavelength end of the spectrum, similar to the results seen earlier. The extended quasistatic approximation is seen to match the variational curve identically at the lower frequencies



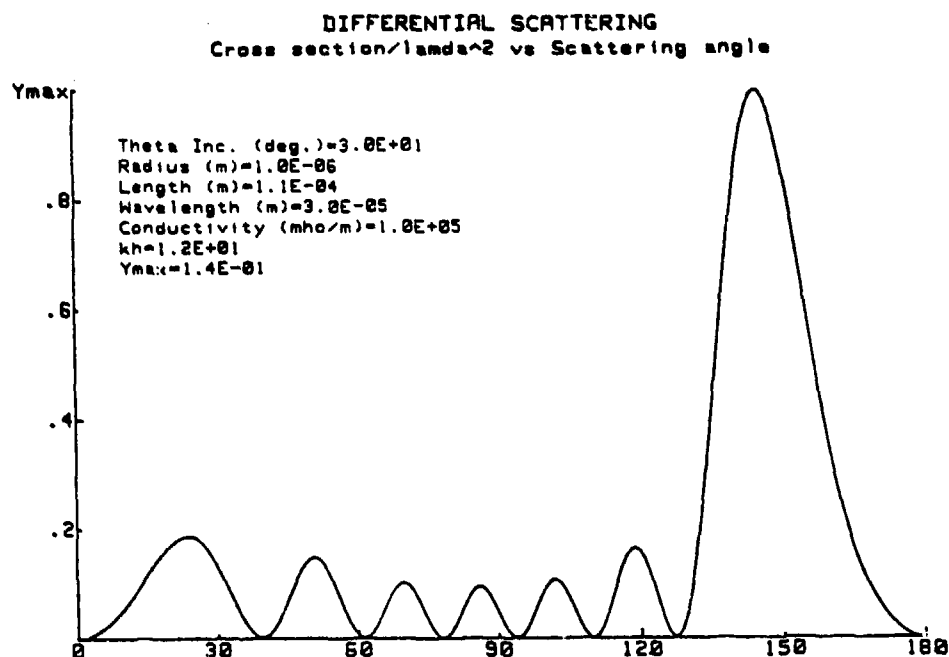


Figure 1-4. Differential scattering pattern is shown vs. scattering angle for a graphite fiber (incidence at 30 deg. from the axis).

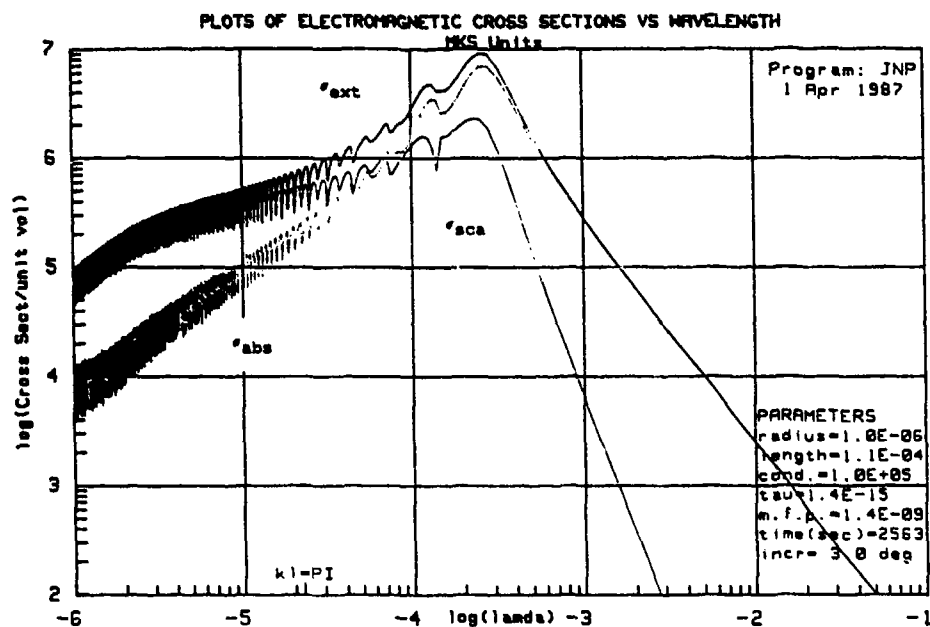


Figure 1-5. Log-log plot is given of the cross sections vs. wavelength for a graphite fiber (length 100 microns).

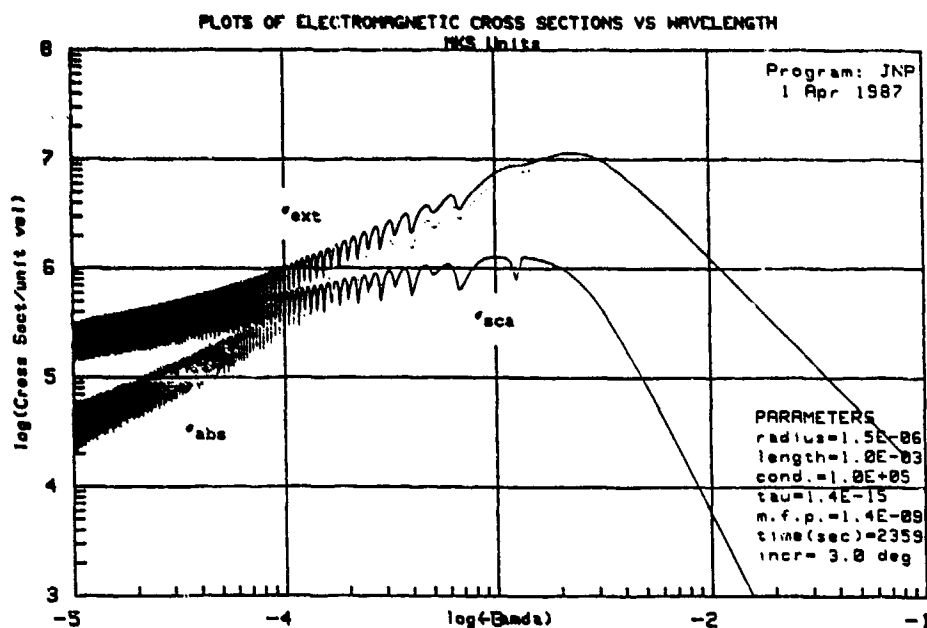


Figure 1-6. Log-log plot is given of the cross sections vs. wavelength for a graphite fiber (length 1000 microns).

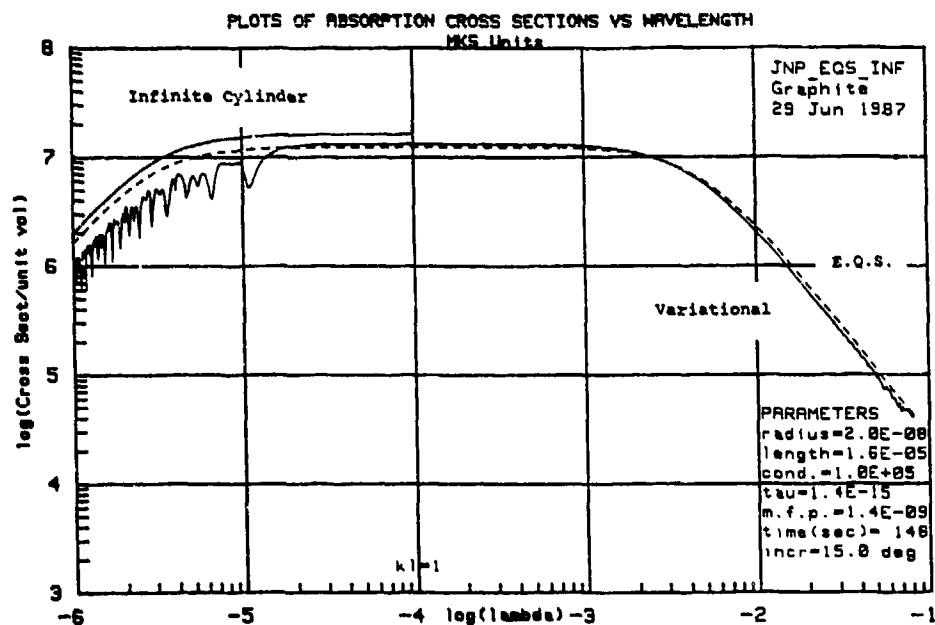


Figure 1-7. Log-log plot is given of the absorption cross section vs. wavelength for a graphite fiber, comparing the variational result with the EQS and infinite cylinder approximations.

up to about  $k\ell = 2\pi$  ( $\lambda = 1.6 \times 10^{-5}$  m) and continues to follow quite well at higher frequencies. The high frequency infinite cylinder approximation (shown beginning at  $k\ell = 1$ ) also gives a good fit to the variational curve, although it is slightly higher.

The corresponding curves are shown in Fig. 1-8 for the same fiber whose length has been increased by a factor of eight. Results are completely analogous to those of Fig. 1-7, although of course the Rayleigh region has now moved offscale to the right, and high frequency oscillations of the variational curve are much more rapid.

Turning now to the case of iron fibers, one has bulk conductivity of  $10^7$  mhos/m and mean free path of  $3 \times 10^{-11}$  m. From Eq. (1-41) one sees that the bulk conductivity requires no correction this time, even for wire radii as small as  $10^{-8}$  m. Choosing an electron relaxation time of  $4.0 \times 10^{-15}$  sec., the complex dielectric constant is again obtained as a function of frequency from Eqs. (1-36) and (1-37).

The differential scattering patterns for iron are shown in Figs. 1-9 thru 1-11 for broadside, 60 and 30 deg. incidence, respectively. Comparing with the earlier Figs. 1-2 thru 1-4 for graphite, the angular distributions are seen to be quite similar. The peak cross sections per square wavelength are seen to be smaller for iron by about  $2 \frac{1}{2}$  orders of magnitude (compare the respective values of  $Y_{\max}$  in the figures), but on the other hand,

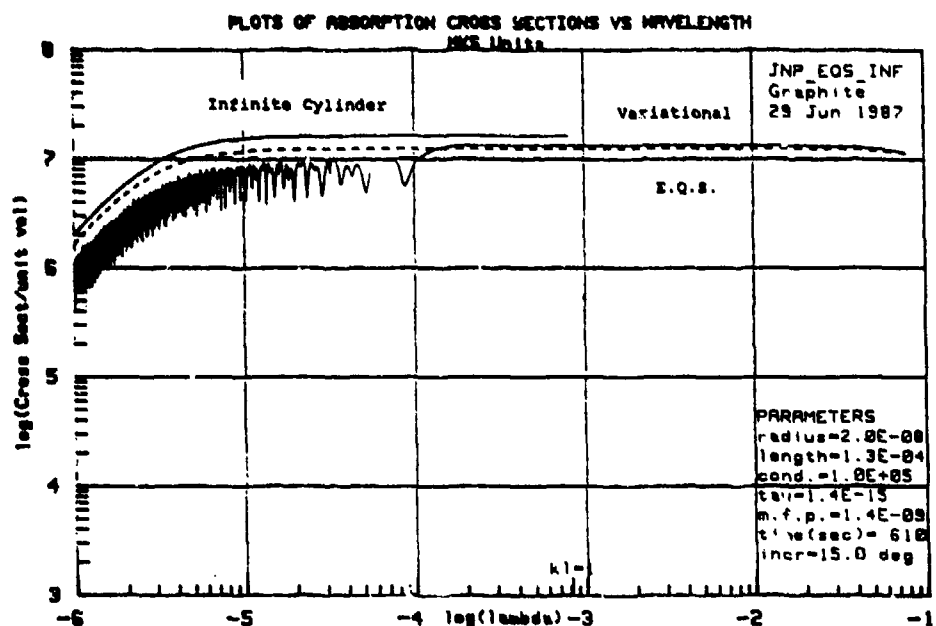


Figure 1-8. Log-log plot is given of the absorption cross section vs. wavelength for graphite fiber, comparing the variational result with the EQS and infinite cylinder approximations.

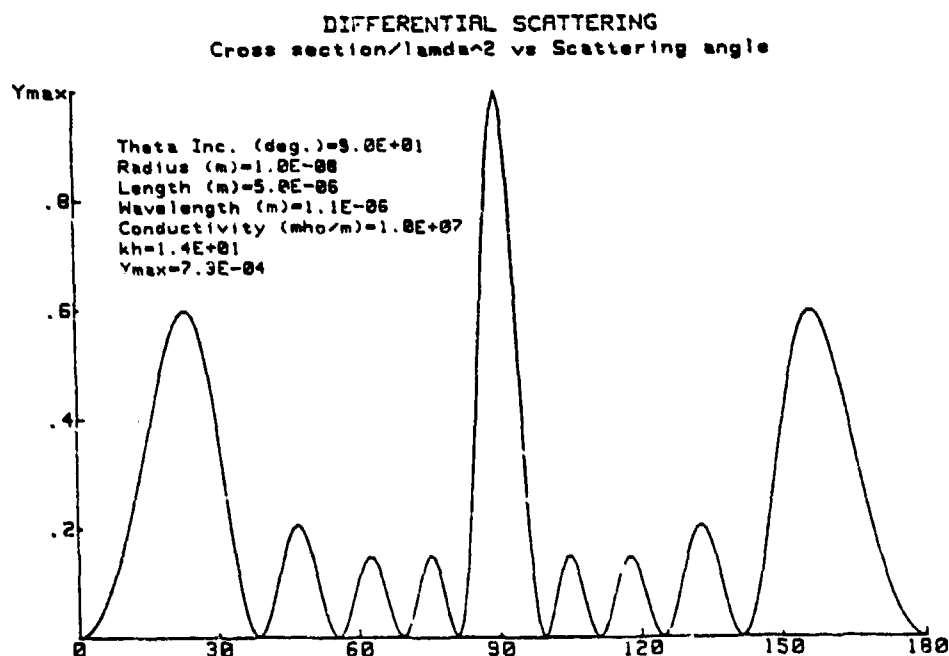


Figure 1-9. Differential scattering pattern is shown vs. scattering angle for an iron fiber (normal incidence).

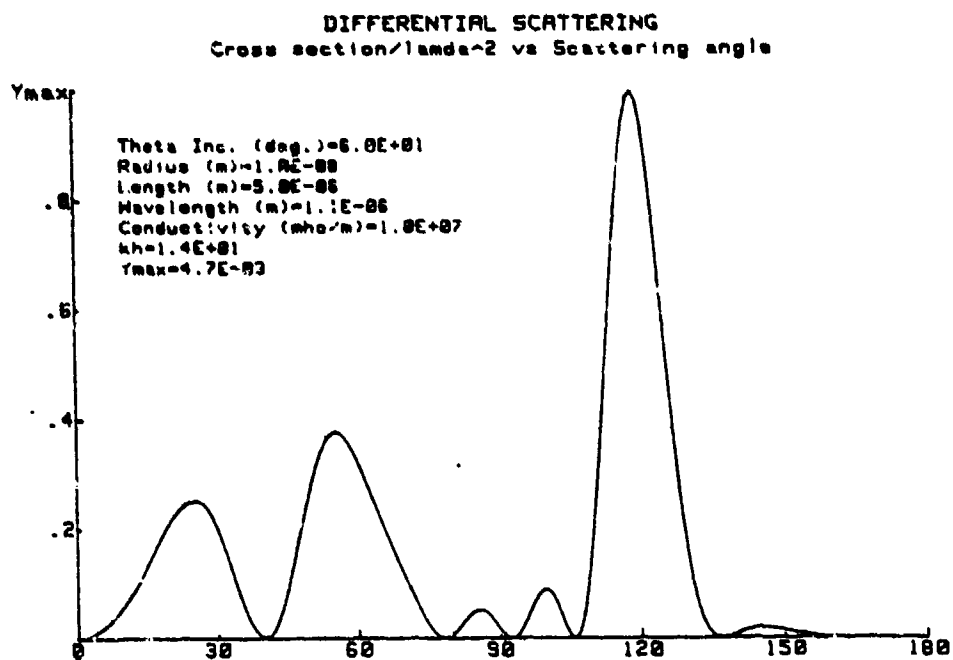


Figure 1-10. Differential scattering pattern is shown vs. scattering angle for an iron fiber (incidence at 60 deg. from the axis).

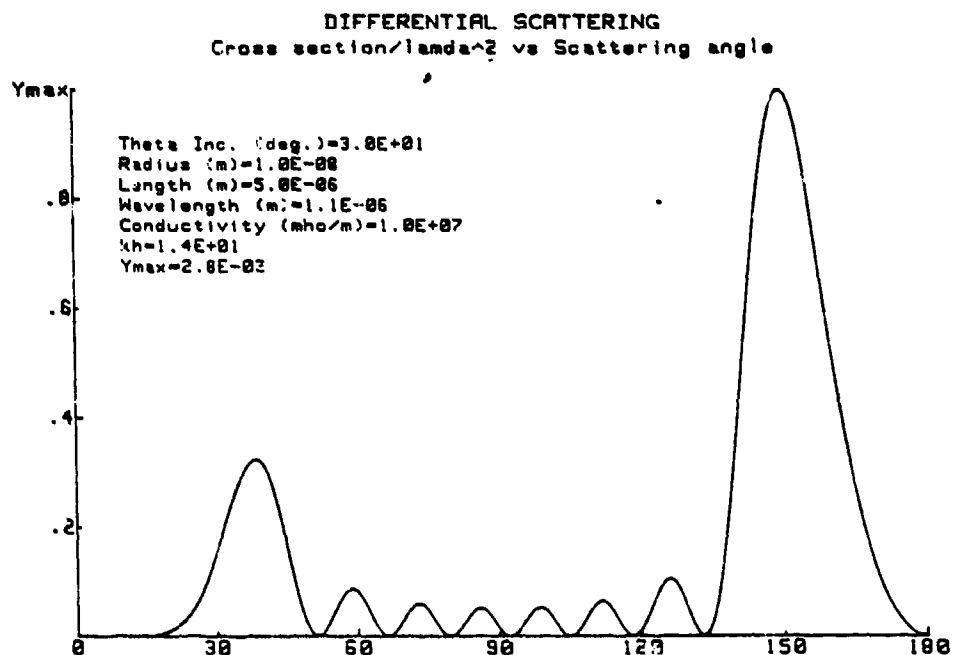


Figure 1-11. Differential scattering pattern is shown vs. scattering angle for an iron fiber (incidence at 30 deg. from the axis).

the actual fiber volume for iron has been reduced by about  $5 \frac{1}{2}$  orders of magnitude, so that on a per unit volume basis iron scatters much more efficiently, as one would expect.

Orientation-averaged cross sections for iron fibers are shown in Figs. 1-12 thru 1-14, for progressively longer fibers again with radius .01 microns. For the shortest fiber, length = 5 microns, shown in Fig. 1-12, the absorption cross section is seen to rise vs. frequency and peak fairly sharply in the vicinity of  $k\ell = \pi$ . The scattering cross section is quite negligible in comparison, except at the shortest wavelengths, and consequently the absorption and extinction curves are practically indistinguishable. The dashed curves give the quasistatic approximations, which are seen to be excellent for  $k\ell \leq \pi$ . The approximate absorption cross section matches the variational computation very well up to about  $k\ell = \pi$ , and is somewhat higher at the shorter wavelengths. Similar comments apply for the approximate scattering cross section, although the latter has been cut off and is not expected to apply beyond  $k\ell = \pi$ .

Results are similar when the fiber length is doubled, as shown in Fig. 1-13, although the peaking of the absorption (and extinction) cross section is not quite so pronounced. When the fiber length is increased by a further order of magnitude (Fig. 1-14), the rise to peak values is seen to occur at much longer wavelengths, as one would of course anticipate, and the absorption (and extinction) cross section now shows a broad plateau extending over more than a decade in frequency.

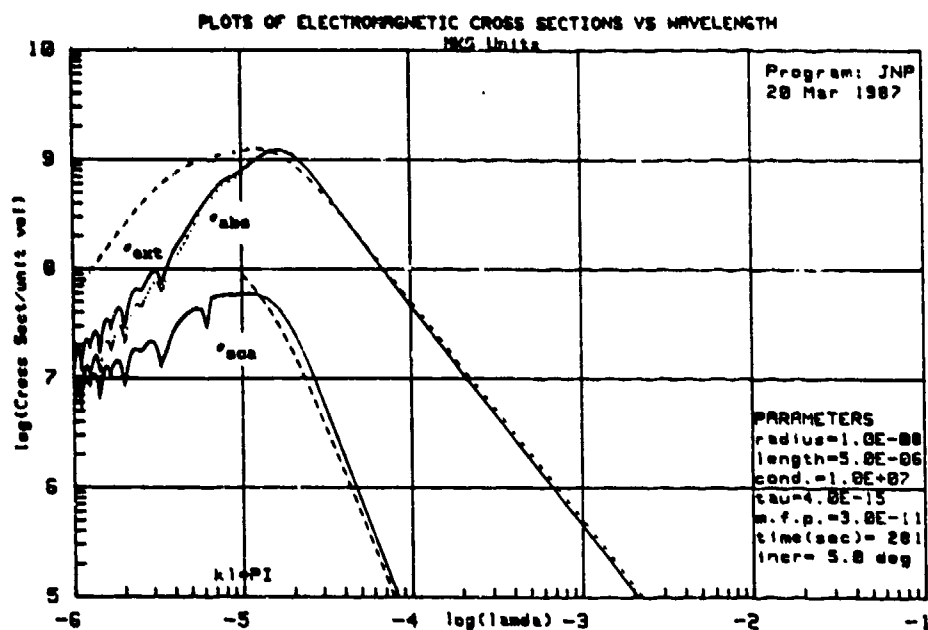


Figure 1-12. Log-log plot is given of the cross sections vs. wavelength for an iron fiber of length 5 microns (dashed curves are quasistatic approximations).

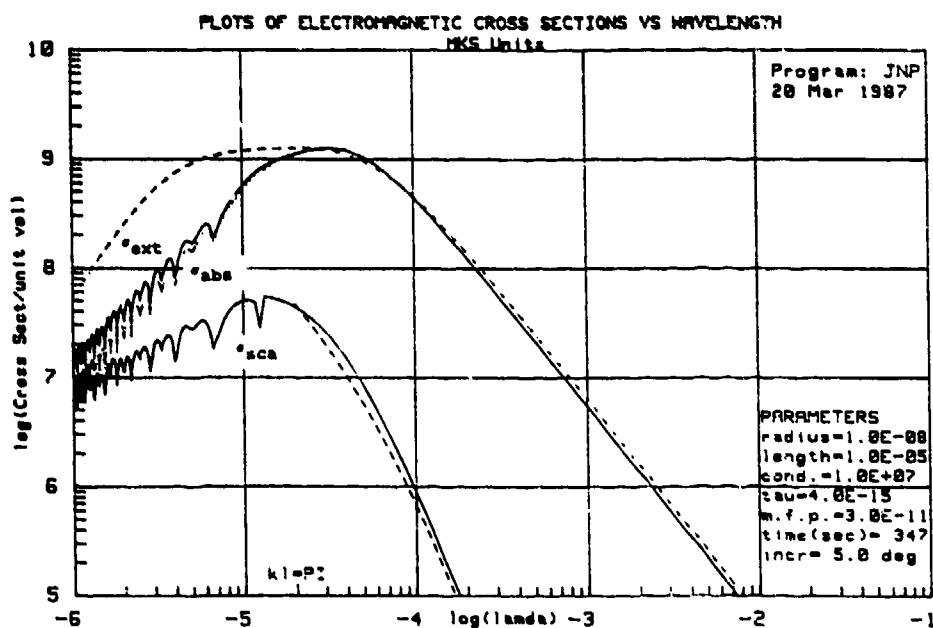


Figure 1-13. Log-log plot is given of the cross sections vs. wavelength for an iron fiber of length 10 microns (dashed curves are quasistatic approximations).

It is interesting that, aside from the more rapid oscillations occurring for the longer fibers in the short wavelength region, due to partial dependence on trigonometric functions of argument  $kl$ , the cross sections are effectively independent of fiber length at the shortest wavelengths.

Some sample computations of absorption cross section for iron are shown in Figs. 1-15 and 1-16. The fiber radii are 2 and 8 microns, respectively, and the length is 64 microns in both cases. The absorption computed by the variational method is similar to results above, showing a peak at a wavelength of about 100 microns. In Fig. 1-15, the extended quasistatic curve tracks the variational results fairly well except at the shorter wavelengths, where it does not decrease as it should (the reason for this discrepancy is not presently understood). The infinite cylinder approximation, on the other hand, does reasonably well at the shorter wavelengths. For the larger fiber radius of Fig. 1-16, both of the approximate computations are seen to be in reasonably good agreement with the variational result.

It is straightforward to compute the cloud mass per square meter required to produce a 20 db target signature reduction, using either graphite or iron particles. The signal decays exponentially within the cloud, and a 10 db reduction on each leg of the round-trip path requires that

$$e^{-n\bar{\sigma}_{\text{ext}}L_c} = 0.1, \text{ or}$$

$$n\bar{\sigma}_{\text{ext}}L_c = 2.3,$$

(1-43)



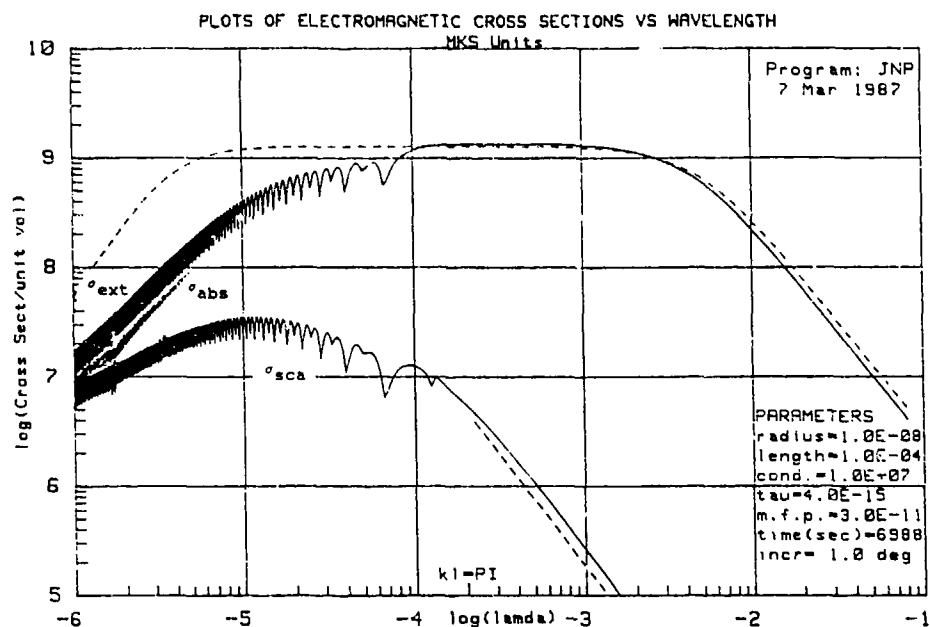


Figure 1-14. Log-log plot is given of the cross sections vs. wavelength for an iron fiber of length 100 microns (dashed curves are quasistatic approximations).

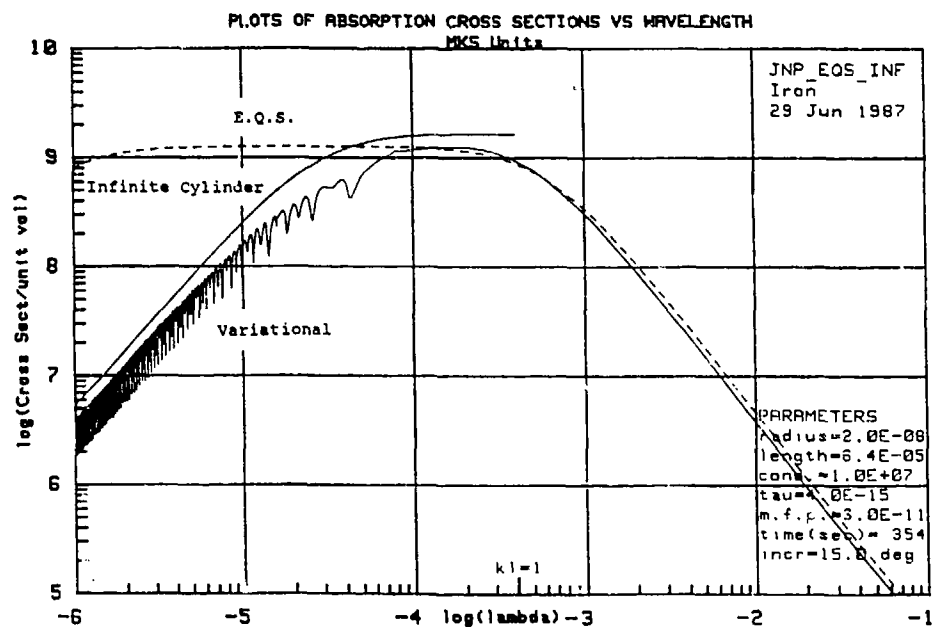


Figure 1-15. Log-log plot is given of the absorption cross section vs. wavelength for an iron fiber, comparing the variational result with the EQS and infinite cylinder approximations.

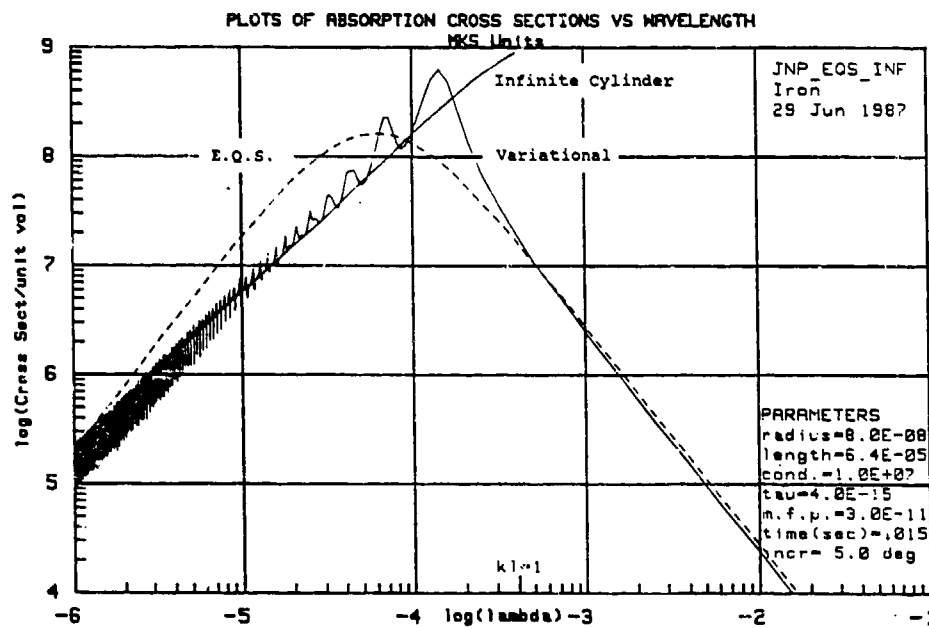


Figure 1-16. Log-log plot is given of the absorption cross section vs. wavelength for an iron fiber, comparing the variational result with the EQS and infinite cylinder approximations.

where  $n$  is the number of fibers per unit volume and  $L_c$  is path length through the cloud. We include an additional factor of  $1/2$  in the extinction cross sections  $\bar{\sigma}_{ext}$  given earlier, so that all polarization and (random) orientation effects are now completely accounted for. Strictly speaking, Eq. (1-43) assumes that absorption dominates over scattering for the single particle. If this is not the case then multiple scattering effects must be more carefully accounted for, using the radiative transfer analysis to be discussed shortly.

For a section of the cloud, having cross-sectional area  $A_c$  and length  $L_c$ , the total mass of fibers  $M$  is given by

$$M = A_c L_c n V_p \rho_p, \quad (1-44)$$

where  $V_p$  is the volume of a single fiber and  $\rho_p$  its density. For the case at hand, setting  $A_c = 1 \text{ m}^2$  and substituting in from Eq. (1-43) gives

$$M = 2.3 \rho_p / (\bar{\sigma}_{ext} / V_p). \quad (1-45)$$

Using this result, from the extinction cross section per unit volume data of Fig. 1-5, and taking a density  $4 \text{ gm/cm}^3$  for graphite, one obtains the mass required at various wavelengths as listed in Table 1-1. Note that the values in parentheses may be underestimates because the fibers are not primarily absorbers at those wavelengths (see Fig. 1-5).

Significantly less mass is required employing iron fibers, as can be seen from the last column of the table. Here we employed the data of Fig. 1-14, assuming  $\rho_p = 7 \text{ gm/cm}^3$  for iron. Note that the increase in density is more than compensated by the higher conductivity, which in turn allows one to employ a greatly reduced fiber radius.

Table 1-1. The mass of graphite or iron fibers required per square meter of cloud cross section for a 20 db reduction in signal strength (values in parenthesis may be underestimates; see text).

<u>Wavelength <math>\lambda</math> (m)</u>	<u>Mass of graphite (gm)</u>	<u>Mass of iron (gm)</u>
$10^{-6}$	(180)	(1.8)
$10^{-5}$	(35)	0.079
$10^{-4}$	(6.3)	0.027
$10^{-3}$	72	0.025
$10^{-2}$	7500	0.16
$10^{-1}$	--	10

### 1.7 Radiative Transfer in Fiber Clouds

In order to compute the transmission and reflection by a cloud of fibers, including multiple scattering effects, we employ radiative transfer techniques, using a computer program developed earlier.<sup>22,23</sup> Essentially, the computation employs the van de Hulst doubling method in a slab geometry, with Taylor series representation for the thin-layer starting values of the transmission and reflection matrices.

For a cloud of identical fibers randomly oriented, as considered here, the required inputs from the single-scattering results are the albedo (ratio of scattering to extinction cross section) and the differential scattering pattern of the single fiber. The calculation has been carried out for both graphite and iron, assuming monochromatic radiation normally incident on a slab region containing the fibers. In each case both wavelength and fiber dimensions are chosen so that the scattering and absorption cross sections are roughly comparable. Results will be given for selected values of the optical depth of the slab (optical depth is obtained by multiplying the thickness by the number of fibers per unit volume and the extinction cross section of one).

Consider first graphite. For an incident wavelength of 30 microns and particle dimensions as listed in Fig. 1-17, the fractions of incident energy reflected from the front (illuminated) face and transmitted through the back (shadowed)

face are shown in the figure as a function of  $\mu = \cos \theta$ , where  $\theta$  is the scattering angle measured from the original incident direction. Optical depth is 0.5 in this instance. Note first the delta-function behavior (truncated at unity for clarity) of the transmitted power in the forward direction  $\mu = 1$ . This represents the coherently transmitted term which has been neither scattered or absorbed. Aside from some minor fluctuations, the balance of the transmitted flux is seen to be essentially isotropic, as is the reflected flux, although both tend to be slightly higher in the grazing directions ( $\mu = 0$ ).

Figures 1-18 thru 1-20 give the corresponding results with successive doublings of the slab thickness, holding all other parameters fixed. The transmitted flux is seen to gradually decrease, as one would expect, and in addition, become concentrated more in the forward direction. Note that the delta-function contribution is difficult to ascertain graphically. This is no problem, however, because we know apriori that the fraction of coherently transmitted flux is given simply by  $e^{-\tau}$  ( $\tau$  = optical depth). The reflected flux distribution is seen to become constant at the largest optical depths; this is of course, just the distribution one would obtain from an infinitely thick slab.

These curves have been integrated to obtain the total fractions of incident flux reflected and transmitted, and the results are listed in Table 1-2. In each case, of course, the balance of the incident flux is absorbed within the fibers. The

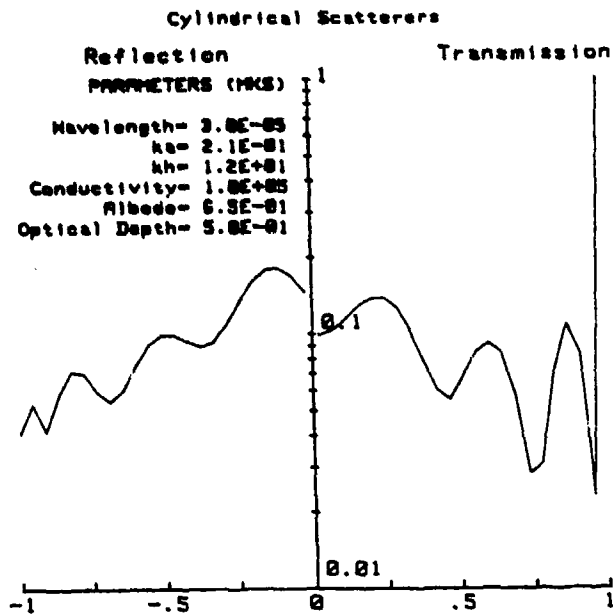


Figure 1-17 . The reflected and transmitted intensities are plotted vs.  $\cos \theta$  ( $\theta$  is the scattering angle) for a cloud of graphite fibers of optical depth 0.5.

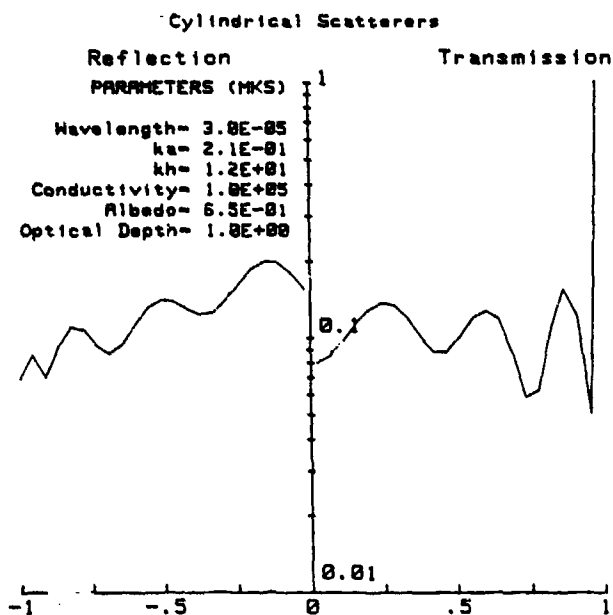


Figure 1-18. The reflected and transmitted intensities are plotted vs.  $\cos \theta$  ( $\theta$  is the scattering angle) for a cloud of graphite fibers of optical depth 1.

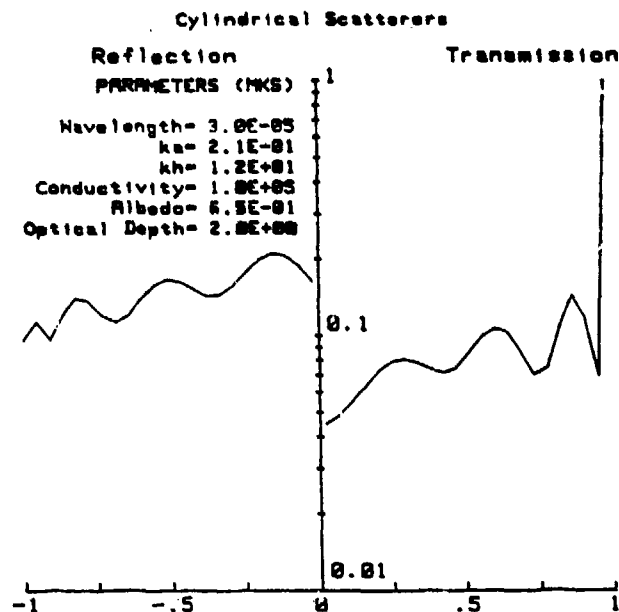


Figure 1-19. The reflected and transmitted intensities are plotted vs.  $\cos \theta$  ( $\theta$  is the scattering angle) for a cloud of graphite fibers of optical depth 2.

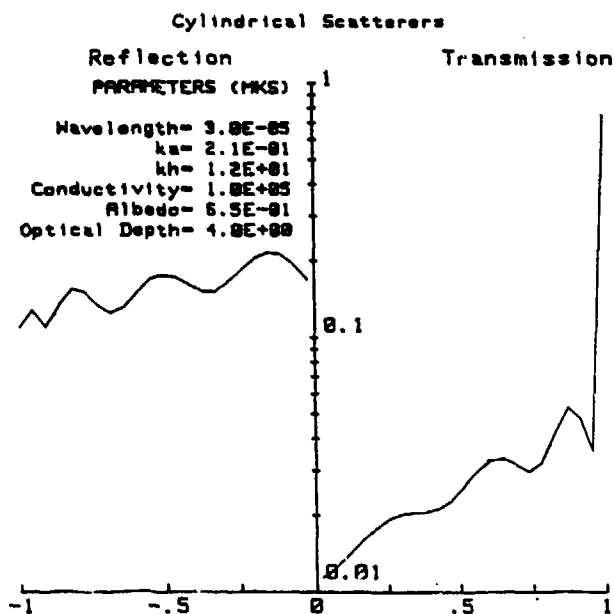


Figure 1-20. The reflected and transmitted intensities are plotted vs.  $\cos \theta$  ( $\theta$  is the scattering angle) for a cloud of graphite fibers of optical depth 4.



Table 1-2. The fractions of (integrated) reflected and transmitted flux are given vs. optical depth for a cloud of graphite fibers (albedo = 0.65).

<u>Optical Depth</u>	<u>Reflected flux</u>	<u>Transmitted flux</u>
0.5	0.083	0.729
1.0	0.120	0.521
2.0	0.145	0.257
4.0	0.151	0.058
8.0	0.152	0.003

total reflected portion is seen to saturate at about 15% for the thicker slabs. It is also interesting to note that for the thickest slab the coherent term makes only a negligible contribution to the total transmitted flux.

The corresponding results for a cloud of iron fibers are shown in Figs. 1-21 through 1-24, this time using an incident wavelength of 1.1 microns and appropriately reduced fiber dimensions, as listed in the figures. Most of the comments made above in connection with graphite are seen to apply here, also, but there are two significant changes. First, the reflected flux pattern is seen to be somewhat weaker and has already become effectively independent of slab thickness at an optical depth of 0.5. Second, the transmitted flux falls off much faster with increasing thickness. Both of these changes are attributable to the smaller albedo encountered, which is of course, just another way of saying that absorption has become dominant over scattering in this case.

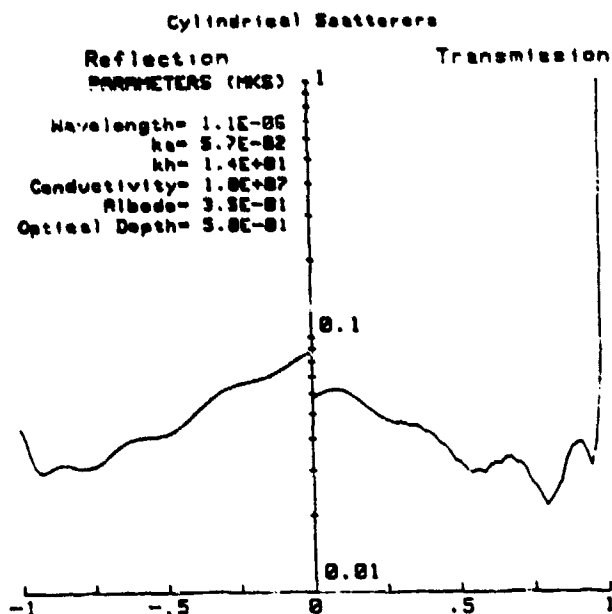


Figure 1-21. The reflected and transmitted intensities are plotted vs.  $\cos \theta$  ( $\theta$  is the scattering angle) for a cloud of iron fibers of optical depth 0.5.

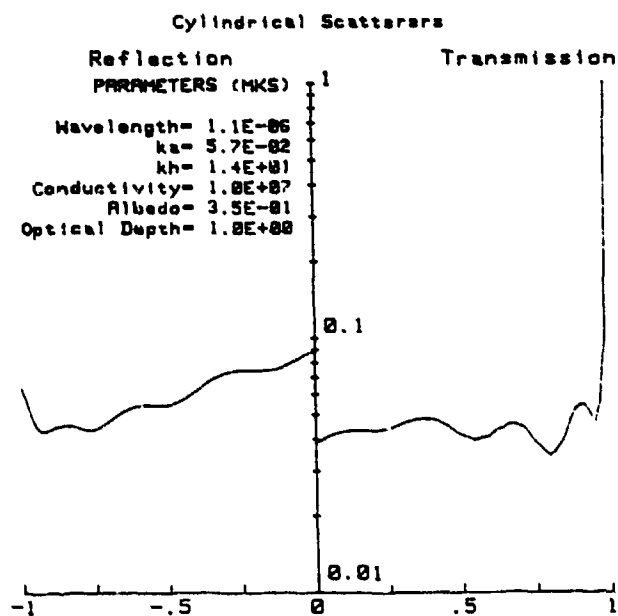


Figure 1-22. The reflected and transmitted intensities are plotted vs.  $\cos \theta$  ( $\theta$  is the scattering angle) for a cloud of iron fibers of optical depth 1.

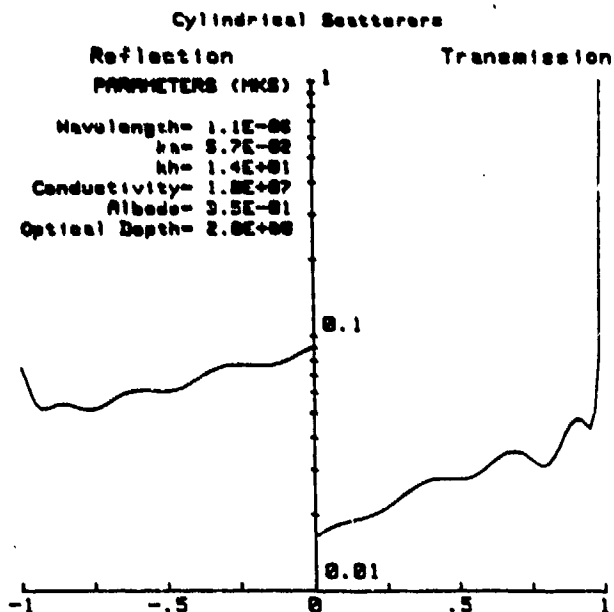


Figure 1-23. The reflected and transmitted intensities are plotted vs.  $\cos \theta$  ( $\theta$  is the scattering angle) for a cloud of iron fibers of optical depth 2.

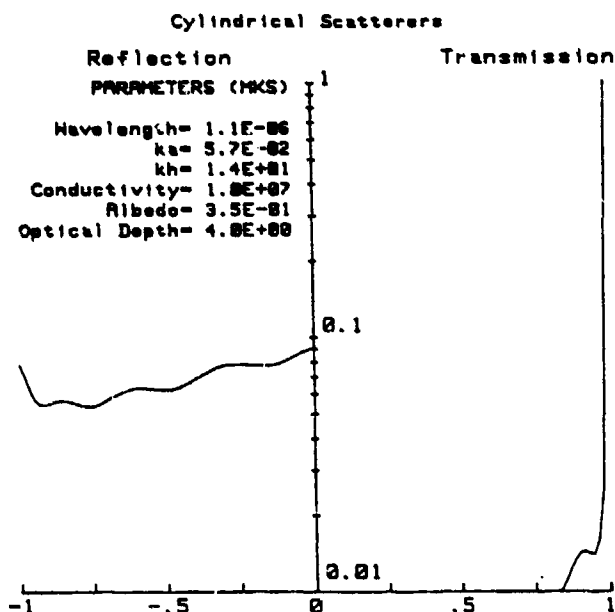


Figure 1-24. The reflected and transmitted intensities are plotted vs.  $\cos \theta$  ( $\theta$  is the scattering angle) for a cloud of iron fibers of optical depth 4.

The corresponding integrated fluxes for iron are listed vs. optical depth in Table 1-3. One sees from the table that the total reflected flux indeed changes very little with increasing slab thickness, and at the same time the transmitted flux is somewhat smaller and falling off more rapidly than in the earlier case.

Table 1-3. The fractions of (integrated) reflected and transmitted flux are given vs. optical depth for a cloud of iron fibers (albedo = 0.352).

<u>Optical Depth</u>	<u>Reflected flux</u>	<u>Transmitted flux</u>
0.5	0.042	0.659
1.0	0.055	0.427
2.0	0.062	0.176
4.0	0.063	0.028

## SECTION II. THERMAL RADIATION BY SMALL PARTICLES

### 2.1 Introduction

In the calculation of electromagnetic scattering and absorption by small particles having at least one dimension on the order of the wavelength of the incident radiation, it is not uncommon that the absorption (as well as the scattering) cross section can be significantly greater than the projected area of such particles. This is easily understood from the electromagnetics point of view and causes no serious concern. However, if we consider the thermal radiation from such a particle, some interesting questions arise with respect to its thermal emissivity, its thermal radiation spectrum, and the connection between such radiation and classical radiation theory. The purpose of this paper is to address these questions and to propose a quantitative model for the calculation of the electromagnetic radiation spectra of small absorbing particles. Of particular interest will be particles of the type discussed in Section I, namely thin conductive cylindrical particles having large absorption efficiency factors.

## 2.2 Classical Radiation Theory

In this section we summarize those aspects of the classical theory of radiation that are pertinent to the discussion to follow.

**Thermal Equilibrium.** Take the classical case of a perfectly insulated spherical cavity whose temperature is  $T$  and whose wall absorbs 100% of all radiation incident upon it. If all elements of the wall are to be in thermal equilibrium, then each element must radiate 100% of the radiation incident upon that element. Since this must be true at all temperatures, it follows that the absorptivity  $\alpha$  and the emissivity  $\epsilon$  of the wall must each be equal to unity. The resulting radiation is well known as blackbody radiation, whose spectral distribution is given by the Planck Radiation Function.

To summarize,

$$\alpha_{bb} = \epsilon_{bb} = 1, \quad (2-1)$$

where  $_{bb}$  is taken to represent blackbody properties.

The Planck Radiation Function is given by:

$$W_{bb}(\lambda, T) = \frac{2\pi c^2 h}{\lambda^5 (e^{hc/\lambda kT} - 1)}, \quad (2-2)$$

where  $c$ =speed of light,  $h$ =Planck's constant,  $k$ =Boltzmann's constant,  $\lambda$ =wavelength, and  $T$ =absolute temperature. With the insertion of an

appropriate constant ( $10^{-10}$ ), the units of  $W_{bb}$  are the usual watts/cm<sup>2</sup>-micron, assuming that Eq. (2-2) is originally evaluated in MKS units.

The intensity of the radiation emitted by a blackbody is the integral over all wavelengths of the Planck Radiation Function:

$$I_{bb}(T) = \int_0^{\infty} W_{bb}(\lambda, T) d\lambda. \quad (2-3)$$

The total power radiated by the blackbody is obviously the product of the radiant intensity and the area  $A_{bb}$  of the blackbody:

$$P_{bb}(\text{rad}) = A_{bb} I_{bb} \text{ watts.} \quad (2-4)$$

**Kirchoff's Law.** Next, place within the cavity a body having area  $A$  and wavelength dependent absorptivity  $\alpha(\lambda)$  and emissivity  $\epsilon(\lambda)$ . Since the radiant flux is uniform within the cavity, the power absorbed by the body is given by

$$P_{\text{abs}} = A \int_0^{\infty} \alpha(\lambda) W_{bb}(\lambda, T) d\lambda. \quad (2-5)$$

which are that these quantities are the ratios of absorptance and emittance, respectively, to those of a blackbody.

Note that, in Eq. (2-5), we have used the same temperature  $T$  as for the (blackbody) walls of the cavity. This is essentially the definition of thermal equilibrium, namely that two bodies in thermal equilibrium must be at the same temperature.

The power radiated by the body is

$$P_{\text{rad}} = A \int_0^{\infty} \epsilon(\lambda) W_{\text{bb}}(\lambda, T) d\lambda. \quad (2-6)$$

The important consequence of the above discussion is that, if the body is in thermal equilibrium with its surroundings, its absorptivity and emissivity must be equal at all wavelengths. This is true because, in thermal equilibrium, Eq.'s (2-5) and (2-6) must be equal for any value of temperature  $T$ .

Therefore,

$$\alpha(\lambda) = \epsilon(\lambda). \quad (7)$$

Equation (2-7) is what we might term the "detailed" statement of Kirchoff's law of thermal radiation. One usually sees this in the form of the average values of  $\alpha$  and  $\epsilon$ . Since (2-7) is crucial to the subsequent treatment, it was developed in what we believe to be a simple but fundamental manner.



### 2.3 Microscopic Particles

**Absorbed power.** The power absorbed by a particle at any specified wavelength  $\lambda$  is, by the definition of the absorption cross section, the product of the incident radiant intensity and the absorption cross section. If wavelength of the incident radiation is  $\lambda_0$ , then

$$P_{abs} = I_0(\lambda_0) \sigma_{abs}(\lambda_0). \quad (2-8)$$

In the more general case, if the incident radiation occurs over a spectrum of wavelengths, we must use the integral form of (2-8):

$$P_{abs} = \int_0^{\infty} \sigma_{abs}(\lambda) W_{inc}(\lambda) d\lambda, \quad (2-9)$$

where  $W_{inc}(\lambda)$  is the intensity spectrum of the incident radiation.

The absorption efficiency factor is defined as the ratio of the absorption cross section of a body to its projected area  $A_p$ :

$$Q_{abs}(\lambda) = \sigma_{abs}(\lambda) / A_p. \quad (2-10)$$

Rewriting Eq. (2-9),

$$P_{abs} = A_p \int_0^{\infty} Q_{abs}(\lambda) W_{inc}(\lambda) d\lambda, \quad (2-11)$$

Note that  $Q_{\text{abs}}(\lambda)$  for the particle in Eq. (2-11) replaces  $\alpha(\lambda)$  for the macroscopic body in Eq. (2-5). We write explicitly,

$$\alpha(\lambda) = Q_{\text{abs}}(\lambda). \quad (2-12)$$

Since, in Eq. (2-7), we have shown that  $\alpha(\lambda) = \epsilon(\lambda)$  for any body, it directly follows that

$$\epsilon(\lambda) = Q_{\text{abs}}(\lambda). \quad (2-13)$$

**Radiated Power.** The power radiated by the particle is therefore given by

$$P_{\text{rad}} = A_p \int_0^{\infty} Q_{\text{abs}}(\lambda) W_{\text{bb}}(\lambda, T) d\lambda, \quad (2-14)$$

where  $A_p$  - total area of the particle.

In the steady state, the power radiated by the particle is equal to the power absorbed. Therefore, Eq.'s (2-11) and (2-14) must be equal. Equating these provides the expression for total radiated power by the particle, as a function of the incident radiation spectrum:

$$P_{\text{rad}} = A_p \int_0^{\infty} Q_{\text{abs}}(\lambda) W_{\text{inc}}(\lambda) d\lambda = A_p \int_0^{\infty} Q_{\text{abs}}(\lambda) W_{\text{bb}}(\lambda, T) d\lambda. \quad (2-15)$$

Using the expression (2-2) for  $W_{bb}$ , we obtain an expression involving only the temperature of the particle, its geometry ( $A$  and  $A_p$ ), and the integrated spectrum of the incident radiation:

$$A \int_0^{\infty} Q_{abs}(\lambda) \frac{2\pi c^2 h}{\lambda^5 (e^{(hc/\lambda k T_{eff})} - 1)} d\lambda = A_p \int_0^{\infty} Q_{abs}(\lambda) W_{inc}(\lambda) d\lambda, \quad (2-16)$$

where we have used  $T_{eff}$  in place of  $T$ , as discussed in the following section.

Equation (2-15) has the units of intensity. In the case of monochromatic incident radiation at wavelength  $\lambda_0$ , we can write:

$$A \int_0^{\infty} Q_{abs}(\lambda) \frac{2\pi c^2 h}{\lambda^5 (e^{(hc/\lambda k T_{eff})} - 1)} d\lambda = A_p Q_{abs}(\lambda_0) I_{inc}(\lambda_0). \quad (2-17)$$

Equations (2-16) and (2-17) can be used to compute the radiating temperature of the body, as a function of its wavelength dependent absorption efficiency factor and the spectral content of the radiation incident upon it. Also, the integrand of these equations is the thermal radiation spectrum of the body.

## 2.4 Interpretation

**Emissivity.** Equations (2-16) and (2-17) are valid, regardless of the numerical values  $Q_{abs}$ . In particular, as we have shown, when  $Q_{abs}$  is larger than unity, the emissivity is correspondingly large. If one considers this from the thermodynamics point of view, some questions arise, such as "How can a radiating body have an emissivity greater than that of a blackbody?" The following is a brief discussion of why this is not an unreasonable circumstance.

In the steady state, the particles comprising the body are elevated to higher energy states by virtue of absorption of power from the incident wave. The body loses energy at this same rate by virtue of the (presumably) random emission of photons as the excited particles drop into lower energy states. In the case of a 'macroscopic' body, all of whose dimensions are very large compared with all wavelengths of importance, it is easy to understand how the emissivity must be dependent only upon the composition of the body. However, in the case of the 'microscopic' body, its geometry also plays an important role in the wavelength dependent probability of emission of photons. Why should this be so?

The answer is that the same geometrical properties that cause the body to absorb electromagnetic energy at a rate proportional to its absorption cross section, similarly influence thermal radiation by the quantum mechanical system of particles. A detailed analysis of this problem would involve the

full quantum mechanical treatment of the system of particles, in which the geometry of the body would necessarily be included.

If we think about the absorption from the point of view of Maxwell's equations, but consider the radiation from the quantum mechanical point of view, the picture can be quite confusing. The particles under consideration here behave in some respects like macroscopic bodies and in other respects like quantum mechanical systems having absorption and emission spectra determined by the modal constraints (which depend upon the composition as well as the geometry) of the specific particle.

From the quantum viewpoint, if the dimensions of the body were all on the order of an optical (radiating) wavelength, only certain wavelengths of absorption and emission would be permitted. As, e.g., one dimension is increased, the modal structure will become more complex. At a sufficiently large dimension, the transition probabilities overlap and the body exhibits a continuum in its emission and absorption spectrum.

The case of coherent incident radiation and incoherent thermally emitted radiation would not pose a problem if the analysis were carried out at a sufficiently fundamental level.

**Temperature.** The temperature appearing in Eq.'s (2-16) and (2-17) can also lead to some questions regarding its precise meaning. We believe that there is no question about its meaning when we consider the thermal radiation from the body. But, is this the "thermodynamic" temperature that one could in

principle measure with a thermometer? This question is analogous to that cited above with respect to the emissivity. The body under consideration has some properties that are most easily considered from the macroscopic thermodynamic point of view and other properties that must be thought of from the quantum point of view. The concept of "temperature" arises from the assumption that one is dealing with a body of sufficiently large dimensions that the use of macroscopic thermodynamic quantities is appropriate. To avoid possible contradiction, we will use the term "effective radiating temperature"  $T_{\text{eff}}$  in the discussions to follow, and as in Eq.'s (2-16), (2-17).

## 2.5 Computational Procedure

In this section, we present computational results obtained through the use of the foregoing theoretical treatment. Note that, in the use of Eq.'s (2-16) and (2-17), one would normally be provided with that information needed to reduce the RHS of (2-16) or (2-17) to a number. The mathematical problem is to find that value of  $T_{\text{eff}}$  in the integral that satisfies the equation.

The procedure in the simpler case of monochromatic incident radiation is as follows:

- (1) Compute  $Q_{\text{abs}}(\lambda_0)$  over a wavelength range sufficiently broad to include  $\lambda_0$ , as well as that of the thermal radiation by the particle.
- (2) Evaluate the RHS of Eq. (2-17).
- (3) Perform successive numerical integrations of the LHS of (2-17) to obtain a table and graph of  $T_{\text{eff}}$  vs  $I_{\text{inc}}(\lambda_0)$ . The wavelength of the incident radiation must be explicitly provided.
- (4) Choose a value of  $T_{\text{eff}}$  from step (2-3) by numerical interpolation or from the graph, that corresponds to the incident intensity  $I_0$ . This value of  $T_{\text{eff}}$ , and the wavelength of the incident radiation, are input to the computer.
- (5) The computer program computes and plots the radiated intensity or

power spectra, the intensity of the incident radiation (watts/cm<sup>2</sup>), and the analogous blackbody ( $Q_{abs}-1$ ) intensity or power spectra.

In the case of illumination over a wavelength spectrum within which  $Q_{abs}(\lambda)$  undergoes substantial variation, Eq. (2-16) would be used to compute  $T_{eff}$  vs  $\int Q_{abs}(\lambda)W(\lambda)d\lambda$  over the incident wavelength spectrum. The latter quantity is the average intensity of the incident radiation, and would be substituted for  $I_0$  in step (3) above.

The accuracy of the numerical integration routines of (3) above is easily checked by letting  $Q_{abs}=1$  (blackbody) and comparing the numerically evaluated integral with the analytic result of the Stephan-Boltzmann Law:

$$\int W_{bb}(\lambda, T) d\lambda = \sigma T^4.$$



## 2.6 Results

In order to carry out the computations outlined above, we must choose a theoretical model for calculating the wavelength dependent absorption efficiency factor  $Q_{abs}(\lambda)$ . For simplicity, we will choose for this discussion the Extended Quasistatic (E.Q.S.) model<sup>\*</sup>, which is described in Section I. This model, although not as exact as the Variational technique (discussed also in Section I), has the advantages of being analytic and of utilizing short computer run times. In the case of engineering applications, the E.Q.S. model would be first used to optimize the various parameters. Having accomplished this, one would then use the Variational technique for the final computations.

We first note that (E parallel to particle axis) in the parameter regime where the absorption cross section is maximized ( $L\epsilon'' < 1$  or  $L'\epsilon'' < 1$ , as the case may be), the expression for the absorption efficiency factor reduces to

$$Q_{abs} \rightarrow \frac{\pi}{2} a \sigma_c \sqrt{\mu_o / \epsilon_o}, \quad (L\epsilon'' \rightarrow 0). \quad (2-18)$$

Note that: (1) in this regime, the absorption efficiency factor is proportional to the particle radius,  $a$ , and is independent of wavelength. This fact can be utilized in the tailoring of the spectral emissivity of a particle cloud e.g. graphite or iron. (2) The ratio  $\sigma_{abs}/Q_{abs}$  is the projected area of the absorbing particle, with respect to the direction of the incident radiation. The results in Fig.(1) were obtained by assuming that the incident E-vector is parallel to the particle axis. The implications of

this will be discussed in a subsequent subsection. (3) For the assumed cylindrical particles, the absorbed power is proportional to  $A_p - 2al$ , while the radiated power is proportional to  $A - 2\pi al$ .

### 2.6.1 Graphite.

Our first examples of small particulate radiation involve particles composed of graphite. The first example will use particles having very small radii of 100 Angstroms. Such particles can be produced by, for example, chemical vapor deposition<sup>2</sup>. The conductivity of these is estimated to be  $10^5$  mho/m. The estimates of mean free time and mean free path of  $1.35 \times 10^{-15}$  sec. and  $4 \times 10^{-15}$  m, respectively, were provided to N. Pedersen by I. Spain, Colorado State University.

Figure 1 is a log-log plot of the absorption efficiency factor vs wavelength for the graphite particles discussed above. The particle length was chosen to be 10 microns. Note that the coordinates each span five orders of magnitude. The wavelength range is from  $0.1 \mu$  to 1 cm. Note that the absorption is a constant over the range from about  $5 \mu$  to about 5 millimeters. Note also that, for this particular particle,  $Q_{abs} < 1$  at all wavelengths shown.

Table 2-1 and Fig.2-2 were computed and plotted\*, as previously outlined, by means of inserting a temperature  $T_{eff}$  in Eq. (2-17) and solving for the incident intensity  $I_0$ . Note that the wavelength of the incident beam was chosen to be  $\lambda_0 = 10.6$  microns. This computation, involving numerical integration of the LHS of Eq. (17), was carried out for each value of  $T_{eff}$  shown in Table 1. Also shown in the Table and in Fig.2-2 are the

corresponding values of  $I_0$  for an equivalent blackbody ( $Q_{abs} = 1$  at all wavelengths). Since, as stated,  $Q_{abs} < 1$ , we would expect that  $T_{eff}$  for this particle would be greater for a given value of  $I_0$  than  $T_{eff}$  for the equivalent blackbody: The efficiency for absorption is greater at 10.6 microns than it is at the shorter wavelengths. Therefore, the particle must be hotter (relative to a blackbody) in order to radiate the same power that it absorbs.

From the above, it is clear that it is only the shape of the  $Q_{abs}(\lambda)$  vs  $\lambda$  curve, and not its magnitude, that determines the curve of  $T_{eff}$  vs  $I_0(\lambda_0)$ . Table 1 and Fig.2-2 are not strictly required for these computations, but are provided to lend insight into the physics of the interactions. .

In Fig.2-3 are shown log-log plots of spectral emittance (in the usual units of watts/cm<sup>2</sup>-micron) vs wavelength in microns. The solid line represents radiation from the graphite particle, and the dashed line is the usual Planck blackbody spectral radiation curve. The input parameters are  $T_{eff} = 2500$  deg.K, and the wavelength of the incident radiation,  $\lambda_0 = 10.6\mu$ . The incident intensity,  $I_0(\lambda_0) = 2600$  watts/cm<sup>2</sup>, is automatically computed.

The blackbody radiates at least an order of magnitude more efficiently than the particle. This is because  $Q_{abs}$  is on the order of 0.1 or less in the radiation wavelength regime shown. The blackbody spectrum is skewed somewhat towards the shorter wavelengths. This is because the absorption efficiency decreases with decreasing wavelength for wavelengths smaller than  $\sim 5\mu$ .

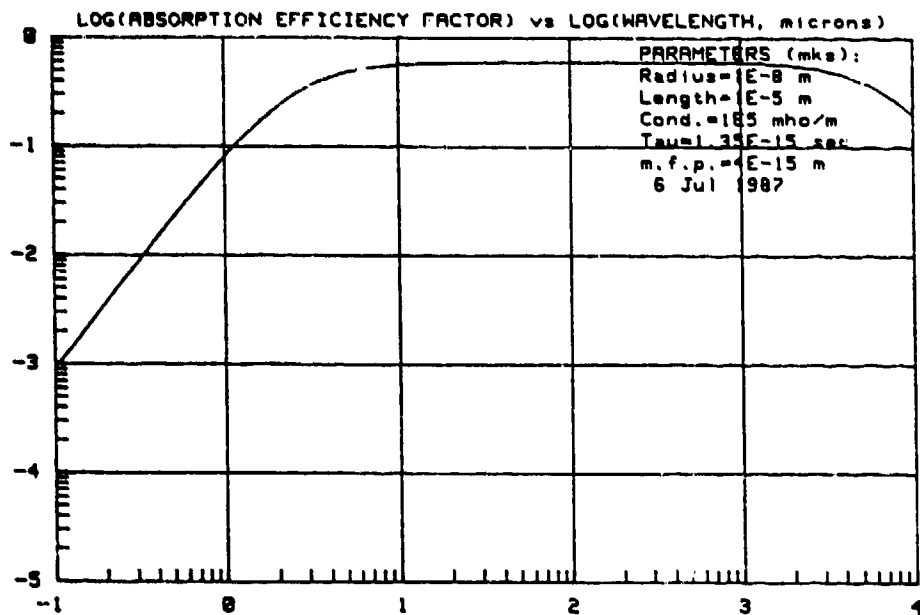


Figure 2-1. Absorption efficiency factor vs wavelength for a 100 Angstrom radius graphite fiber.

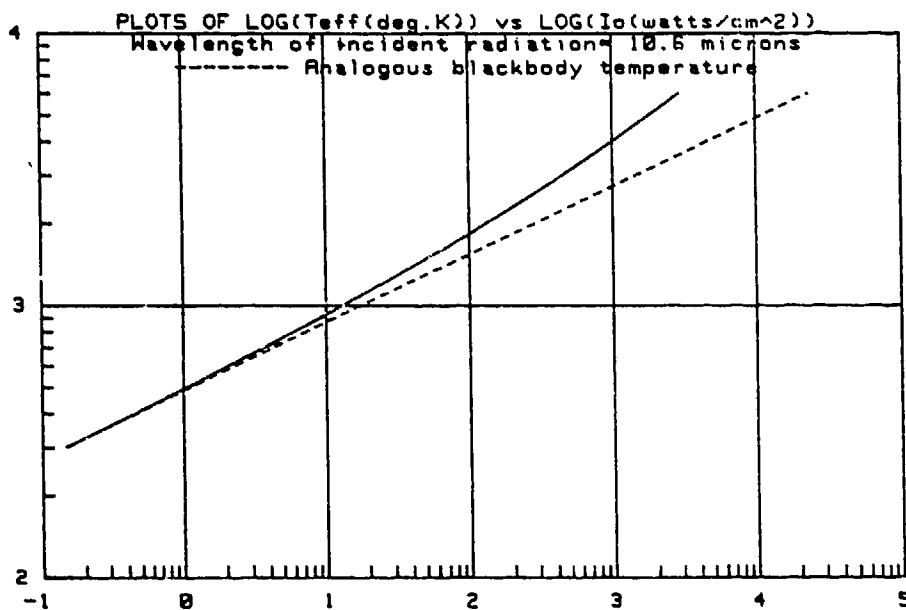


Figure 2-2. Plots of  $T_{eff}$  vs  $I_0$  from Table 2-1.  $\lambda_0 = 10.6$  microns.

Lambda(inc)=10.6 microns  
 Radius=1E-8m  
 Length=1E-5m  
 Bulk cond=1E5w/m  
 m.f.p.=4E-15m  
 Tau=1.35E-15sec  
 6 Jul 1987

Io (watts/cm <sup>2</sup> )	Io(blackbody) (watts/cm <sup>2</sup> )	Teff (deg.K)
1.45E-01	1.44E-01	300
1.85E-01	1.84E-01	319
2.34E-01	2.35E-01	339
2.97E-01	3.01E-01	360
3.76E-01	3.84E-01	383
4.77E-01	4.90E-01	407
6.03E-01	6.26E-01	433
7.62E-01	8.00E-01	460
9.62E-01	1.02E+00	489
1.21E+00	1.30E+00	520
1.53E+00	1.67E+00	553
1.92E+00	2.13E+00	588
2.42E+00	2.72E+00	625
3.03E+00	3.47E+00	664
3.80E+00	4.43E+00	706
4.75E+00	5.66E+00	751
5.93E+00	7.23E+00	798
7.39E+00	9.23E+00	848
9.19E+00	1.18E+01	901
1.14E+01	1.50E+01	959
1.41E+01	1.92E+01	1019
1.75E+01	2.45E+01	1083
2.16E+01	3.13E+01	1151
2.66E+01	4.00E+01	1221
3.27E+01	5.11E+01	1301
4.01E+01	6.53E+01	1383
4.91E+01	8.34E+01	1470
6.00E+01	1.06E+02	1563
7.32E+01	1.36E+02	1662
8.90E+01	1.74E+02	1767
1.08E+02	2.22E+02	1878
1.31E+02	2.83E+02	1996
1.58E+02	3.62E+02	2122
1.90E+02	4.62E+02	2256
2.29E+02	5.90E+02	2398
2.75E+02	7.53E+02	2549
3.29E+02	9.62E+02	2710
3.93E+02	1.23E+03	2881
4.69E+02	1.57E+03	3063
5.59E+02	2.00E+03	3256
6.64E+02	2.56E+03	3461
7.87E+02	3.27E+03	3679
9.31E+02	4.17E+03	3911
1.10E+03	5.33E+03	4158
1.30E+03	6.80E+03	4420
1.53E+03	8.69E+03	4698
1.79E+03	1.11E+04	4995
2.11E+03	1.42E+04	5309
2.47E+03	1.81E+04	5644
2.88E+03	2.31E+04	6003

Table 2-1. Radiating temperature vs incident intensity. Thin graphite fiber.

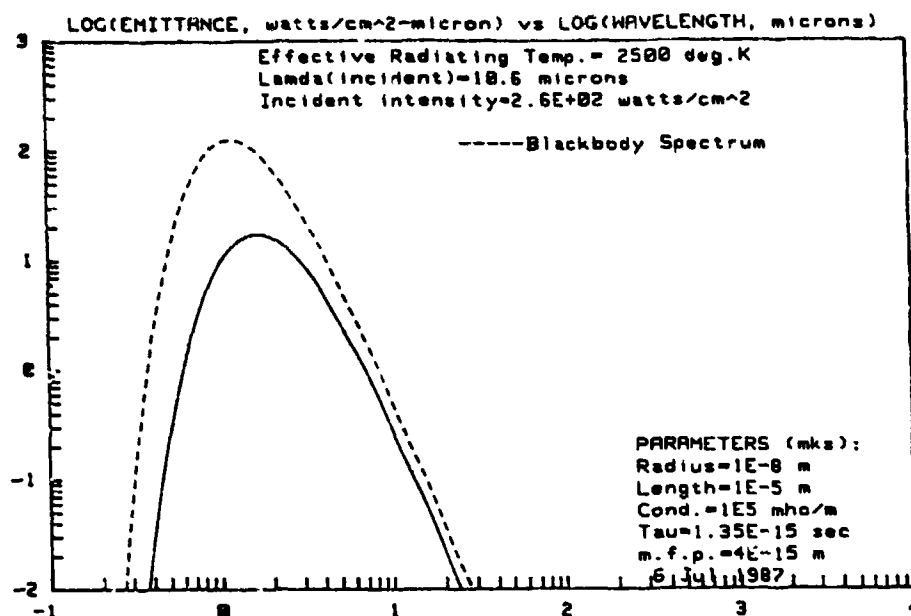


Figure 2-3. Radiant emittance of the 100 Angstrom radius graphite fiber.  
 Effective radiating temperature = 2500 deg. K.

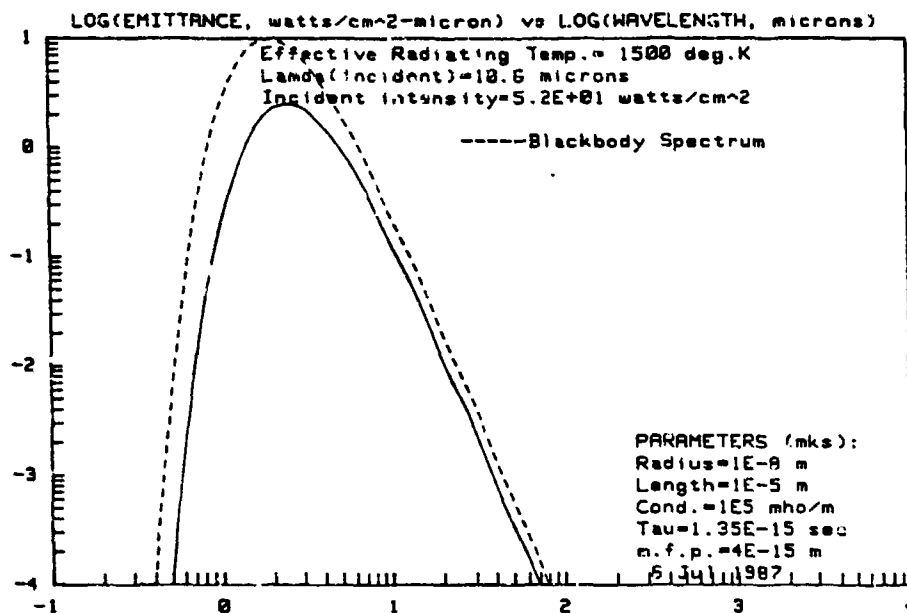


Figure 2-4. Radiant emittance of the 100 Angstrom radius graphite fiber.  
 Effective radiating temperature = 1500 deg. K.

We next lower the temperature  $T_{\text{eff}}$  to 1500 deg.K (Fig.4). The required incident intensity at  $\lambda_0=10.6\mu$  is correspondingly reduced from 2600 to 52 watts/cm<sup>2</sup>. The radiation spectra of the particle and the equivalent blackbody are significantly reduced in magnitude and are shifted towards the longer wavelengths. The curves are more nearly equal in magnitude because  $Q_{\text{abs}}(\lambda)$  is more nearly equal to unity for these radiating wavelengths than in the case of  $T_{\text{eff}}=1500$  deg.

Figures 2-5, 2-6, and 2-7 are similar to Figures 2-3 and 2-4, except that the values of  $T_{\text{eff}}$  (and the corresponding  $I_0(\lambda_0)$ ) are lowered to 1000, 500 and 300 deg.K, respectively. The ratio of particle emittance to that for the blackbody is essentially the same for  $T_{\text{eff}}=500$  deg.K and 300 deg.K. This is because  $Q_{\text{abs}}$  is essentially constant over the radiation spectra for both values of  $T_{\text{eff}}$ .

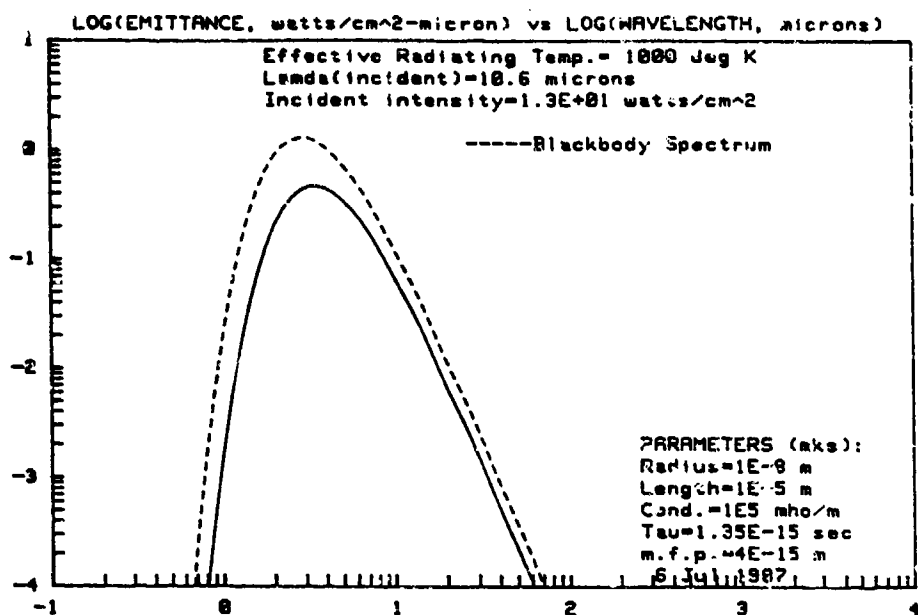


Figure 2-5. Radiant emittance of the 100 Angstrom radius graphite fiber.  
 Effective radiating temperature = 1000 deg. K.

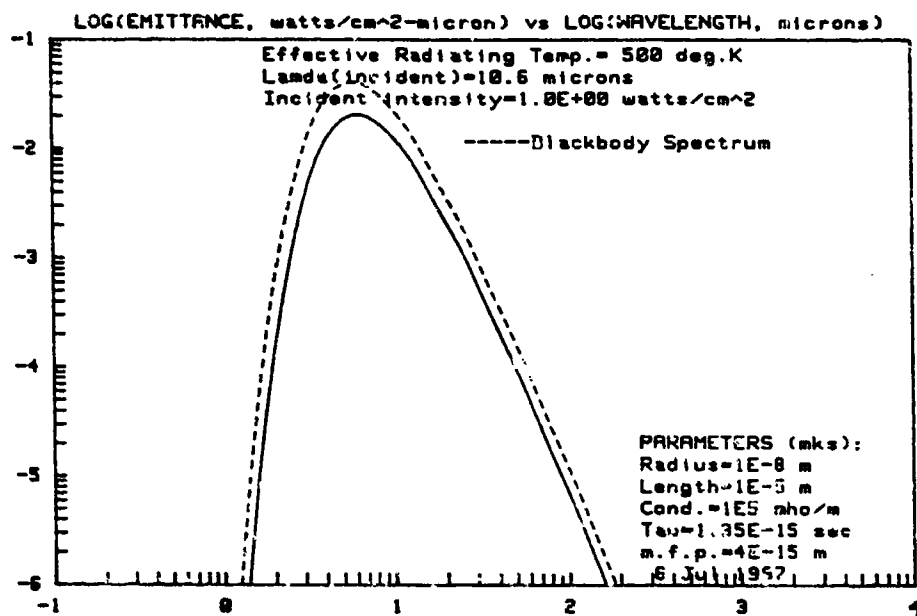


Figure 2-6. Radiant emittance of the 100 Angstrom radius graphite fiber.  
 Effective radiating temperature = 500 deg. K.



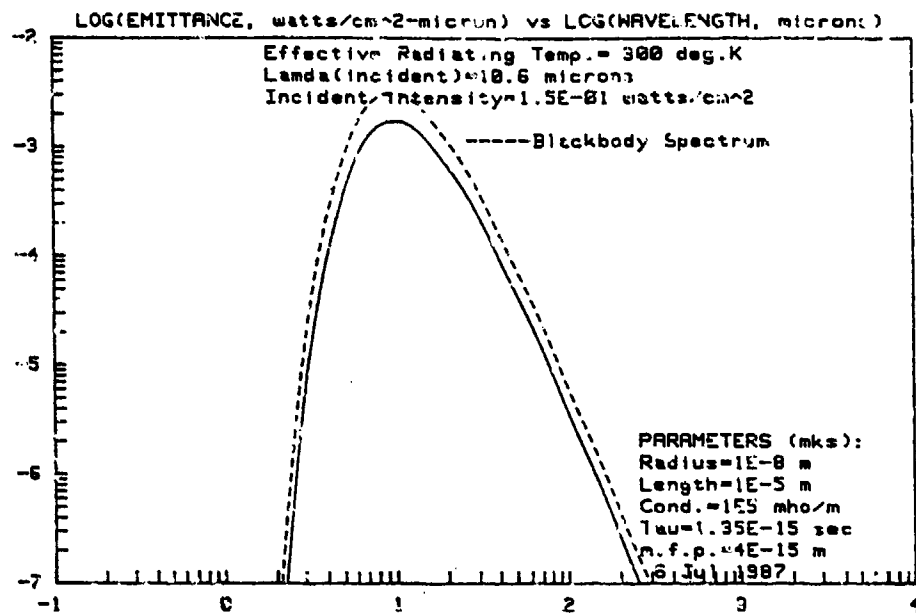


Figure 2-7. Radiant emittance of the 100 Angstrom radius graphite fiber.  
 Effective radiating temperature = 300 deg. K.

It is next instructive to see what happens to the thermal radiation spectrum when  $Q_{abs}(\lambda)$  exhibits more structure than that shown in Fig.2-1. For this purpose, we choose a graphite particle of the more conventional variety, having a length of 1 millimeter and a radius of 1 micron. At the short wavelengths, the correspondingly large values of  $(ka)$  give rise to the resonance shown in Fig.2-8. Note also that the enhancement of  $Q_{abs}$ , as predicted by Eq.(18) is seen at  $\lambda=3$  millimeters.

Figure 2-9 ( $I_o$  vs  $T_{eff}$ ) is analogous to Fig.2-2, but shows, as expected, a much larger deviation from the blackbody curve of Fig.2-2.

The plots of radiation spectra for this particle, with  $T_{eff}$  (and therefore  $I_o$ ) as the incremented parameter are shown in Figs 2-10 through 2-13. In the case of this particle, it is easy to see how the form of  $Q_{abs}(\lambda)$  is reflected in the radiation spectrum. It is particularly interesting to observe that, at the highest temperature, i.e.  $T_{eff}=2500$  (Fig.2-10), the particle radiates as though it were much cooler, as compared with the equivalent blackbody. At the lower temperatures, e.g.  $T_{eff}=500$  (Fig.9), the radiation spectrum (neglecting the cusp) has essentially the same shape as a blackbody at the same radiating temperature.

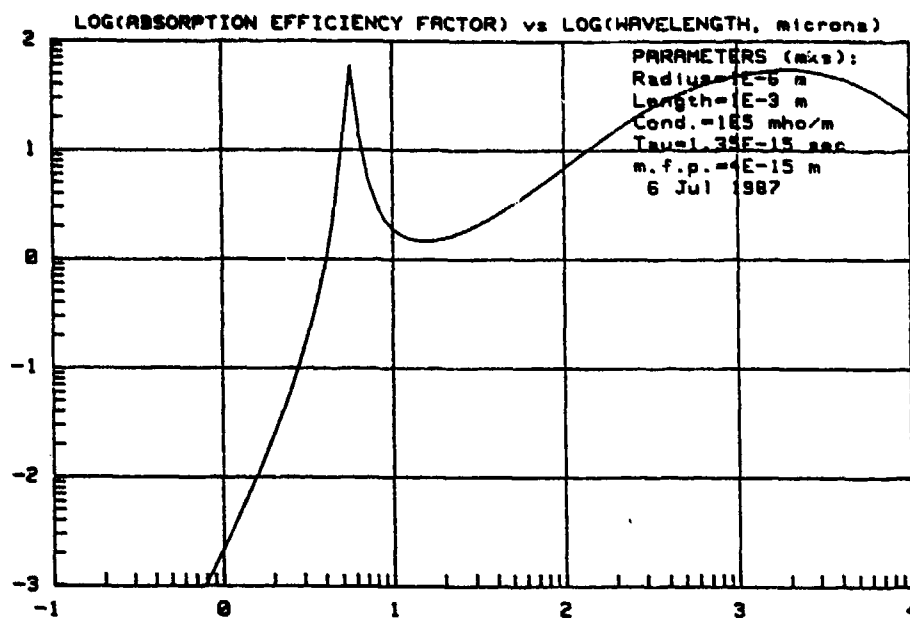


Figure 2-8. Absorption efficiency factor vs wavelength for a 1 micron radius graphite fiber. Note the cusp at  $\lambda = 5\mu$ .

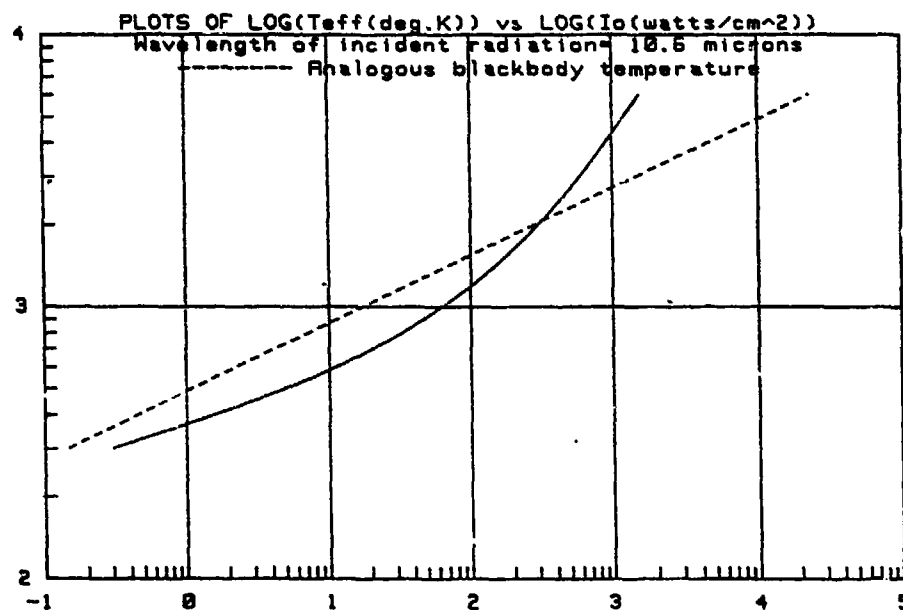


Figure 2-9. Plots of  $T_{eff}$  vs  $I_o$  for the 1 micron radius graphite fiber.  
 $\lambda_o = 10.7\mu$ .

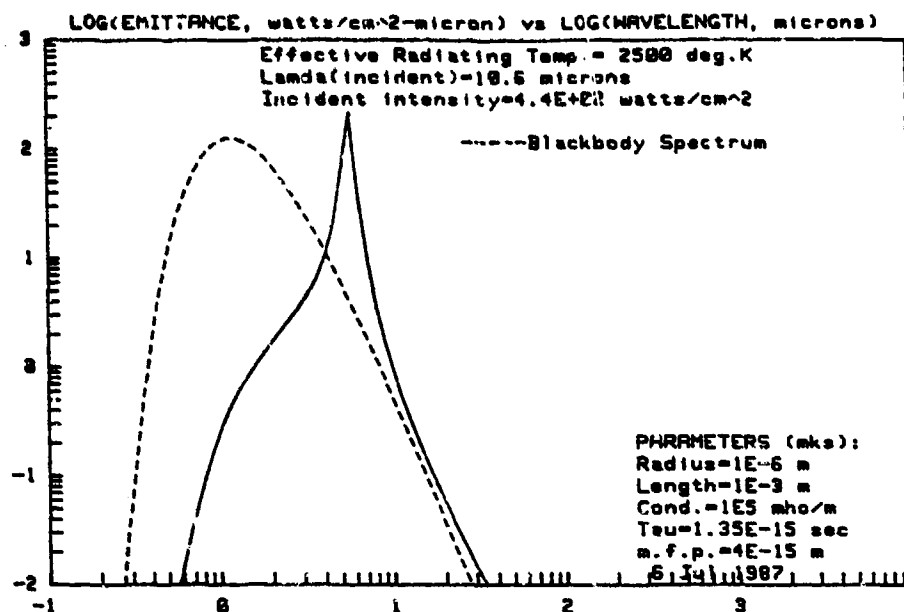


Figure 2-10. Radiant emittance of the 1 micron radius graphite fiber.  
 Effective radiating temperature = 2500 deg. K.

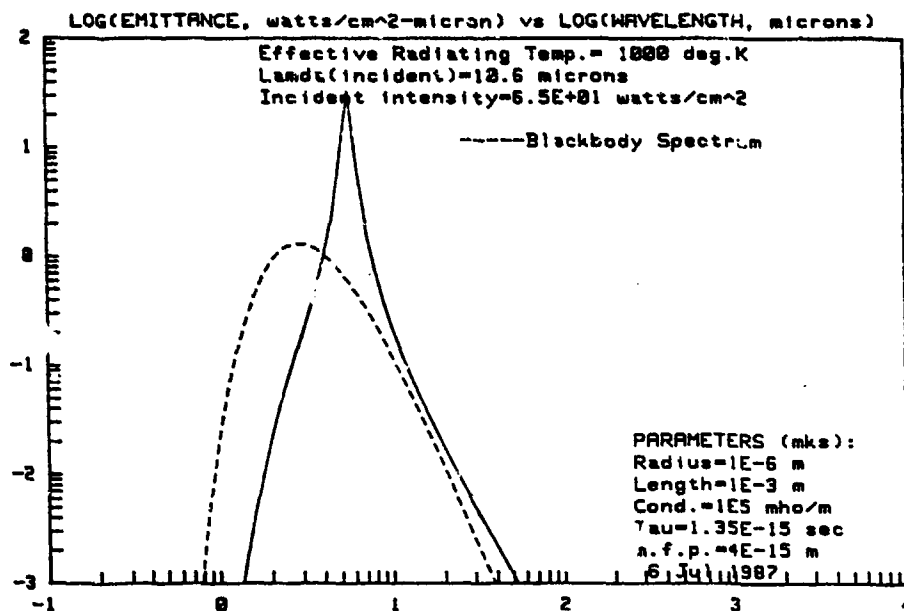


Figure 2-11. Radiant emittance of the 1 micron radius graphite fiber.  
 Effective radiating temperature = 1000 deg. K.

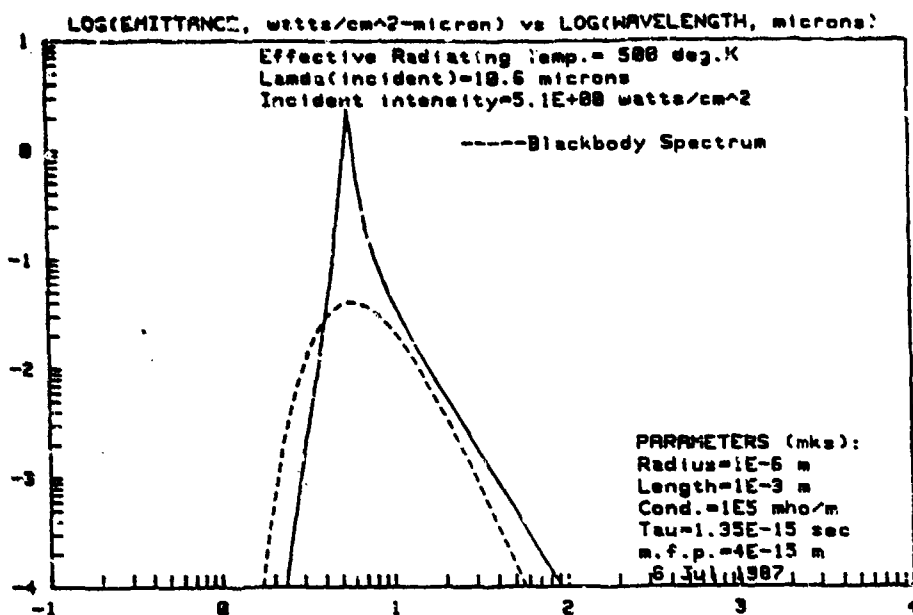


Figure 2-12. Radiant emittance of the 1 micron radius graphite fiber.  
 Effective radiating temperature = 500 deg. K.

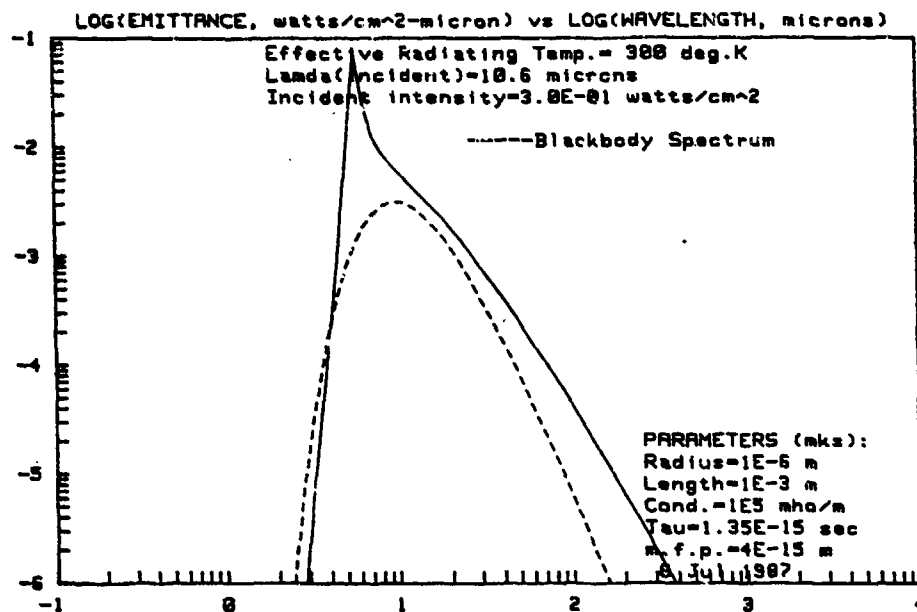


Figure 2-13. Radiant emittance of the 1 micron radius graphite fiber.  
 Effective radiating temperature = 300 deg. K.

### 2.6.2 Iron

Also of interest are very fine filaments of iron. We therefore include herein an example of the radiative properties of such a particle having a radius of 100 Angstroms. For purposes of illustration of the potential for broadband screening (via absorption), we have selected a filament length of 100 microns.

Figure 2-14 displays the absorption efficiency as a function of wavelength. Note that the curve is quite similar to that for 100 Angstrom radius graphite (see Fig.2-1), except that the maximum value of  $Q_{abs}$  is 100X that for graphite. This is because the electrical conductivity of the iron is taken to be  $\sigma_c = 10^7$  mho/m, while that for graphite was assumed to be  $10^5$  mho/m.

In Fig.2-15, we see that the plot of  $T_{eff}$  vs  $I_0$  is essentially the same as that for the 100 Angstrom radius graphite. This is because, as mentioned previously, the shapes of the  $Q_{abs}(\lambda)$  curves (but not their magnitudes) are the same.

In Figs 2-16, 2-17, 2-18, and 2-19 the values of  $T_{eff}$  are 1500 (the maximum permissible), 1000, and 500 deg.K, respectively. The following comments are of interest: (1) The shapes of the radiation spectra are essentially the same as for the thin graphite example (Figs 2-4 through 2-7). (2) The required incident intensity  $I_0$  is nearly the same in the iron vs graphite cases (38 vs 52 watts/cm<sup>2</sup> at  $T_{eff} = 1500$  deg.K). The reason for this is apparent from inspection of Equation (2-17). (3) The magnitude of the emittance is greater by a factor of ~100X for the iron vs the graphite.

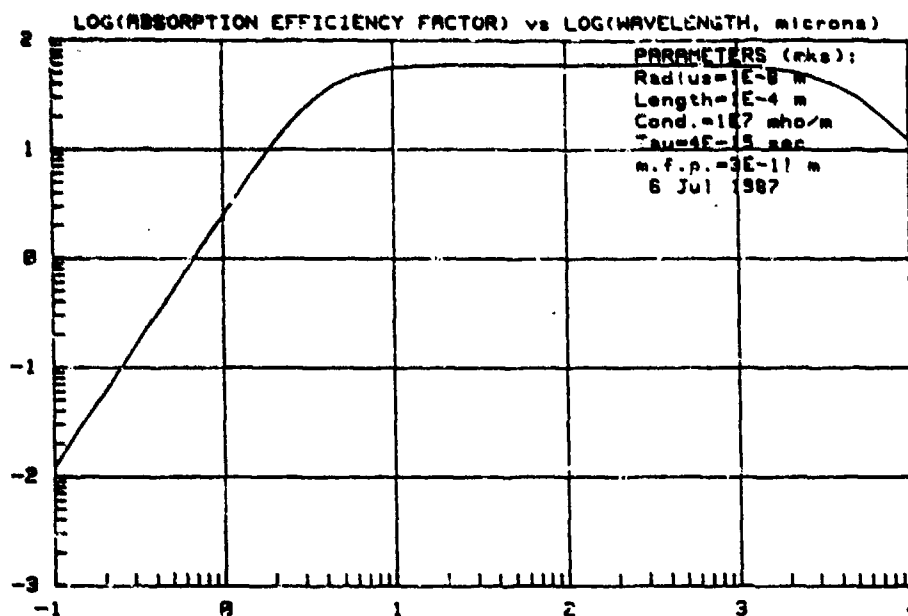


Figure2-14. Absorption efficiency factor vs wavelength for a 100 Angstrom radius iron fiber.

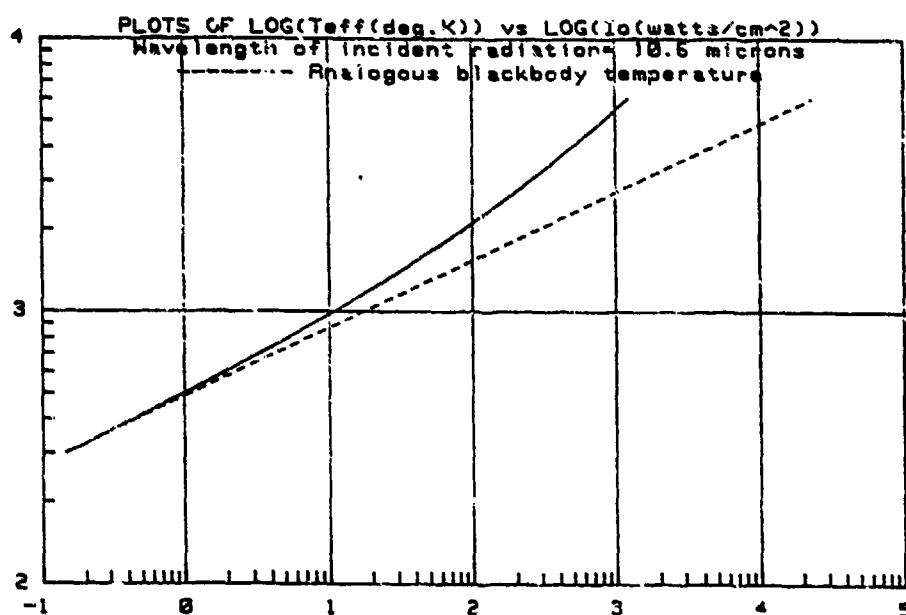


Figure 2-15. Plot of  $T_{\text{eff}}$  vs  $I_0$  for a 100 Angstrom iron fiber.  $\lambda_0=10.6\mu$ .

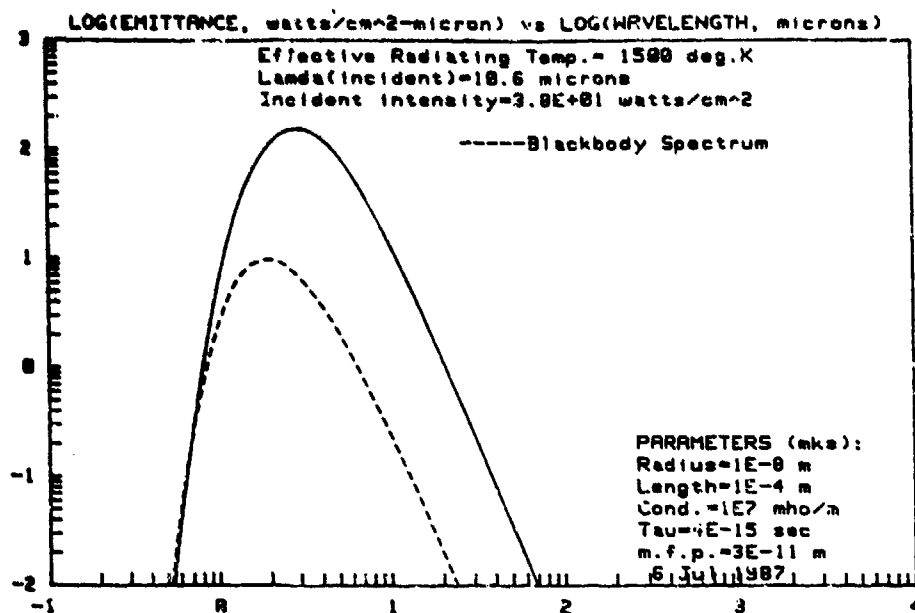


Figure 2-16. Radiant emittance of the 100 Angstrom radius iron fiber.  
 Effective radiating temperature = 1500 deg. K.

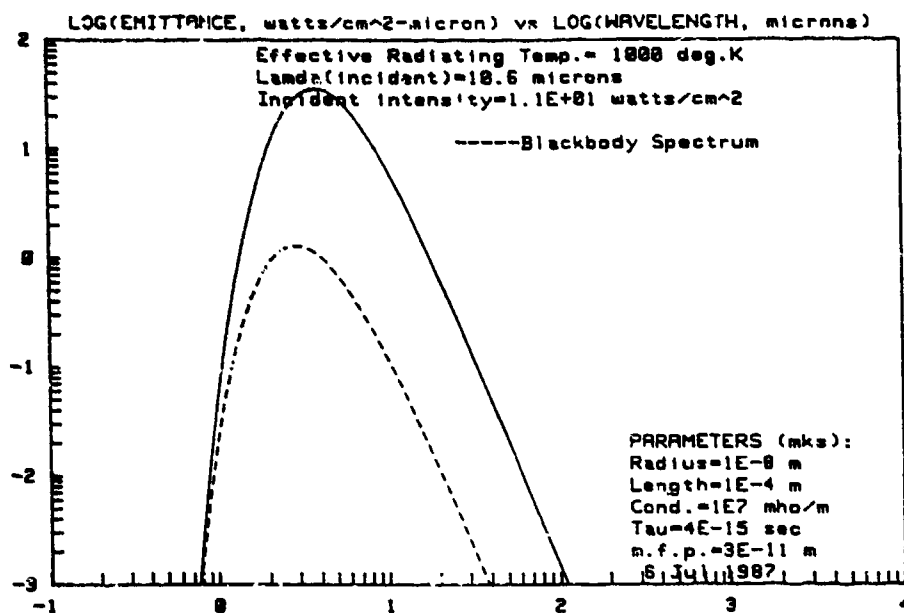


Figure 2-17. Radiant emittance of the 100 Angstrom radius iron fiber.  
 Effective radiating temperature = 1000 deg. K.



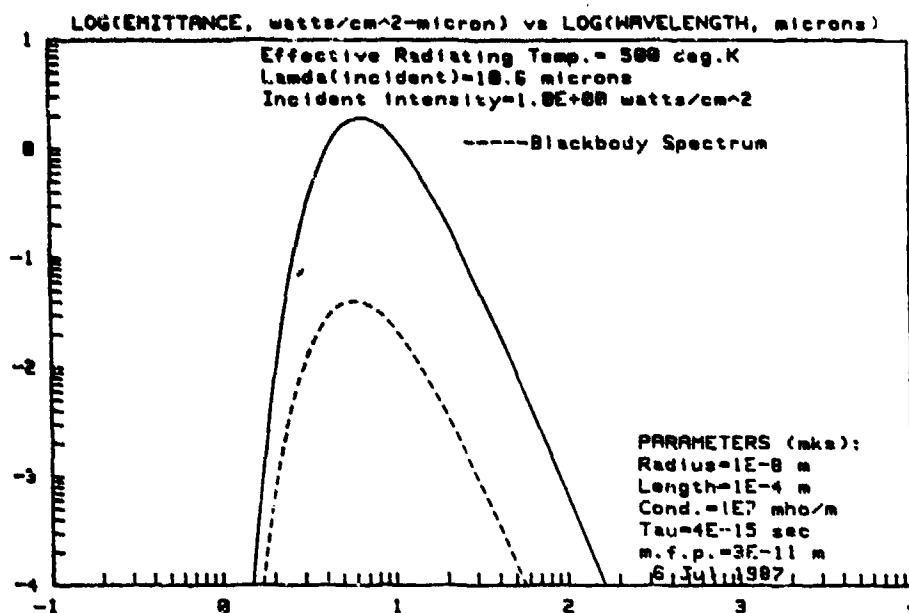


Figure 2-18. Radiant emittance of the 100 Angstrom radius iron fiber.  
 Effective radiating temperature = 500 deg. K.

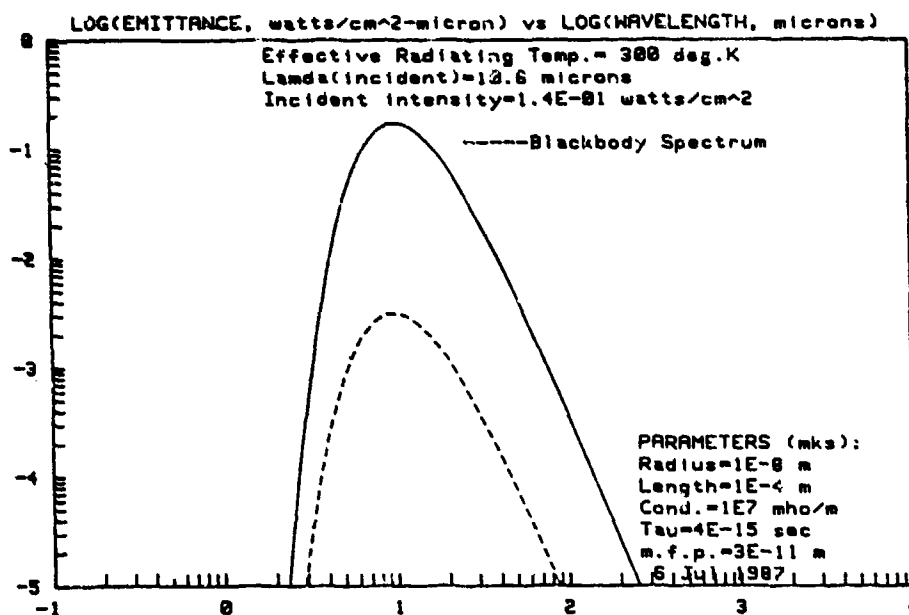


Figure 2-19. Radiant emittance of the 100 Angstrom radius iron fiber.  
 Effective radiating temperature = 300 deg. K.

## 2.7 Applications

In this subsection, we consider some interesting applications of the foregoing treatment. These include various radiative and absorptive effects associated with electromagnetic radiation incident upon aggregates of microscopic absorbing particles. We will also consider the conditions required for vaporization and/or melting of such particles. The environment is assumed to be exoatmospheric. Before addressing these subjects, however, it is necessary that we discuss the geometrical considerations which arise when the absorbing particles are nonspherical and randomly oriented.

### 2.7.1 Geometrical Considerations

As already mentioned, the foregoing analyses were carried out under the tacit assumption that the particle axis is aligned parallel to the electric field vector  $E_0$  of the incident wave. This of course presents no problem for spherically symmetric particles. However, in the case of nonspherical particles, we are interested in the absorption efficiency factor, as a function of the angle of incidence, as well as the polarization angle. We are not permitted to take the average value of  $Q_{abs}(\lambda, \theta_i)$ . Instead, the absorbed power must be calculated using the quantity  $\cos^2(\alpha)Q_{abs}(\lambda, \theta_i) = \cos^2(\alpha)\sigma_{abs}(\lambda, \theta_i)/2a \sin \theta_i$ , where  $\theta_i$  - angle of incidence and  $\alpha$  - polarization angle. The thermal radiation on the other hand, must be calculated as before, using the total particle area  $2\pi al$ . Each value of  $\theta_i$  will therefore give rise to a different radiation spectrum.

As can be seen, the precise calculation of thermal radiation from a small ensemble of randomly oriented nonspherical particles involves a somewhat different treatment than that of Section 2.3. The following accounts for arbitrary particle orientation in the case of our E.Q.S. theory:

We first note that the absorption cross section is proportional to the square of the component of the incident E-field that is projected on the particle axis. Thus, including polarization angle  $\alpha$  and the angle of incidence  $\theta_i$ , the absorption cross section becomes

$$\sigma_{\text{abs}}(\lambda, \alpha, \theta_i) = \sigma_{\text{abs}}(\lambda, 0, \pi/2) \cos^2(\alpha) \sin^2(\theta_i). \quad (2-19)$$

The absorption efficiency factor is inversely proportional to the area of the particle, projected in the plane perpendicular to the incident  $k$  vector. Thus,

$$Q_{\text{abs}}(\lambda, \alpha, \theta_i) = \sigma_{\text{abs}}(\lambda, \alpha, \theta_i) / 2al \sin(\theta_i). \quad (2-20)$$

Combining Eq.'s (2-19) and (2-20), the absorption efficiency factor for arbitrary particle orientation (E.Q.S. theory) is

$$Q_{\text{abs}}(\lambda, \alpha, \theta_i) = \sigma_{\text{abs}}(\lambda, 0, \pi/2) \cos^2(\alpha) \sin(\theta_i) / 2al. \quad (2-21)$$

In the case of monochromatic incident radiation, the absorbed power is

$$\begin{aligned} P_{\text{abs}} &= I_o(\lambda_o) A_p Q_{\text{abs}}(\lambda_o, \alpha, \theta_i) \\ &= I_o(\lambda_o) A_p \sigma_{\text{abs}}(\lambda_o, 0, \pi/2) \cos^2(\alpha) \sin(\theta_i) / 2al, \end{aligned} \quad (2-22)$$

and, in the present nomenclature, the radiated power is

$$P_{\text{rad}} = A \int_0^{\infty} Q_{\text{abs}}(\lambda, 0, \pi/2) \frac{2\pi c^2 h}{\lambda^5 (e^{(hc/\lambda k T_{\text{eff}})} - 1)} d\lambda. \quad (2-23)$$

For cylindrical particles,  $A/A_p = 2\pi a l / 2a l = \pi$ . For monochromatic illumination, an expression, analogous to Eq. (2-17), results from equating Eq.'s (2-22) and (2-23):

$$Q_{\text{abs}}(\lambda_0, 0, \pi/2) \cos^2(\alpha) \sin(\theta_i)$$

$$= \pi \int_0^{\infty} Q_{\text{abs}}(\lambda, 0, \pi/2) \frac{2\pi c^2 h}{\lambda^5 (e^{(hc/\lambda k T_{\text{eff}})} - 1)} d\lambda. \quad (2-24)$$

We see that Eq. (2-24) is transcendental with respect to the variables  $\alpha$  and  $\theta_i$ .

The problem can be solved numerically as follows:

- (1) Assume values of the intensity and wavelength of the incident beam. i.e. assume that we know  $I_0(\lambda_0)$ .
- (2) Successively increment the angles  $\alpha$  and  $\theta_i$  to include all possible orientations of the particle with respect to the incident E-vector.
- (3) For each of the above angular increments, calculate L.H.S. of Eq. (2-24).
- (4) For each above angular increment, solve Eq. (2-24) (by numerical iterative

means) to compute the correct value of  $T_{\text{eff}}$ .

(5) Having obtained  $T_{\text{eff}}$ , compute the radiation spectrum for that specific combination of  $\alpha$  and  $\theta_1$ .

(6) Repeat steps (1) through (5) for each angular incrementation. Add the spectral intensities (watts/cm<sup>2</sup>) according to wavelength for all angles.

The above procedure, using appropriate angular weighting ( $\sin(\theta_1)$ ) and normalization for the numerical integration of (6), will yield the orientation-averaged thermal radiation spectrum from our cylindrical particles. With modification, the more exact Variational technique for calculating  $Q_{\text{abs}}$  can be used in the above method.

### 2.7.2 Aggregates of Absorbing Particles

#### Internally Heated Spherical and Cylindrical Clouds

We now consider the case of a cylindrical cloud of particles. Assume that the source of illumination is uniformly distributed along the cylinder axis, and that, for all wavelengths of interest, the product  $\gamma(\lambda)R \gg 1$ , where  $R$ -radius of the cylinder, and  $\gamma$ -absorption coefficient of the cloud given by

$$\gamma(\lambda) = n\sigma_{\text{abs}}(\lambda) \quad \text{m}^{-1}, \quad (2-25)$$

where  $n$ -number density of absorbing particles ( $\text{m}^{-3}$ ).

In this case, the input radiation per unit axial length is simply  $P_{in}(tot)/L$ , where  $P_{in}(tot)$ -total input power and  $L$ -length of the cylinder. The radiated power must equal the input power, and is emitted over a surface, or "skin" whose depth is approximately  $\gamma^{-1}$ . The effective value of the emissivity of the cylindrical cloud is just that of a blackbody. This is because of the following argument: (1) Within the cloud ( $r \ll (R - \gamma^{-1})$  and  $r \gg \gamma^{-1}$ ), the particles are essentially in thermal equilibrium with their neighbors and the radiation spectrum in such regions is essentially blackbody radiation. (2) The effective number of particles that are radiating at the surface at any wavelength is  $N = nA_c \gamma(\lambda)^{-1}$ , where  $A_c$ -total cloud area. Thus, the larger  $Q_{abs}(\lambda)$  is at some wavelength, the smaller the number of radiating particles that are radiating from the "surface" at that wavelength. (3) Therefore, the radiation from the surface of the cloud will be essentially blackbody radiation and the effective emissivity of the cloud will be unity.

The radiating temperature  $T_{eff}$  of the cloud can therefore be found from the following equation.

$$P_{in} = 2\pi RL \int_0^{\infty} \frac{2\pi c^2 h}{\lambda^5 (e^{(hc/\lambda k T_{eff})} - 1)} d\lambda. \quad (2-26)$$

Knowing  $T_{eff}$ , we can then calculate the radiation spectrum from the integrand of Eq. (2-26).

If the cloud were spherical, and the illuminating source were placed at the

center of the sphere, then the same procedure can be used by replacing the factor  $2\pi RL$  in Eq. (2-26) by  $4\pi R^2$ , where in this case  $R$ =sphere radius.

This equation demonstrates an interesting (and potentially useful) circumstance that an optically thick ( $\gamma R \gg 1$ ) absorbing cloud of particles will radiate essentially as a blackbody whose surface temperature, and therefore its radiation spectrum, can be controlled by its surface area.

### Cylindrical Cloud; External Illumination

We next consider the case of an axially illuminated cylindrical cloud of absorbing particles. This problem only has meaning if  $\gamma R \ll 1$ . If, in addition,  $\gamma L > 1$ , then the incident radiation within the cloud is given by

$$I_{inc}(z) = I_0 e^{-\gamma z}, \quad (2-27)$$

where  $z$  is along the cylinder axis. The particles will radiate with emissivity  $Q_{abs}(\lambda)W_{bb}(\lambda, z)$ . Thus, the radiation spectra of all surface elements of length  $dz$  would be added according to wavelength. As long as the above criteria on  $\gamma R$  and  $\gamma L$  obtain, the overall spectrum from the cylindrical cloud will depend only upon  $Q_{abs}(\lambda)$ .

If the  $\gamma(\lambda)L$  were  $\ll 1$ , then all particles would radiate in accordance with Eq. (2-17), using  $I_{inc} = I_0(\lambda_0)$ , and  $\epsilon = Q_{abs}(\lambda)$ . In the case of axial solar illumination, Eq. (16) is applicable here for computing the radiation spectrum.

### Slab Geometry; External Illumination

The case of external illumination of a slab composed of absorbing particles can be treated simply (see Ref. 24, p.513) using the diffusion approximation. This is appropriate when  $\gamma r \gg 1$  and when  $\sigma_{abs} \gg \sigma_{sca}$ , where  $r$  = slab thickness. We further assume that  $Q_{abs}(\lambda)$  is fairly uniform over the wavelength ranges of interest. The problem is to find the temperatures at the illuminated front surface  $T_{eff}(1)$  and at the back surface  $T_{eff}(2)$ , which is assumed to be not illuminated.

Siegel and Howell provide a simple calculational procedure for the computation of the above temperatures. Their results can easily be used in conjunction with our computational methods to determine the radiation spectrum emanating from both surfaces.

We first note that, if  $\gamma r \rightarrow \infty$ , no thermal radiation will occur at surface 2 and the incident intensity  $I_{inc}$  must therefore be radiated from surface 1, which will radiate as a blackbody. Therefore, the Stefan-Boltzmann law ( $I_{rad} = I_o - \sigma T^4$ ) to calculate the maximum temperature at surface 1. Let this be  $T_{eff}(max)$ .

We now let  $\gamma r$  be fairly large but finite. The temperatures at the two surfaces are then given by<sup>24</sup>

$$T_{eff}(1) = T_{eff}(max) [((1/2) + (3/4)\gamma r) / (1 + (3/4)\gamma r)]^{1/4}, \quad (2-28)$$

and

$$T_{eff}(2) = T_{eff}(max) [(1/2) / (1 + (3/4)\gamma r)]^{1/4}. \quad (2-29)$$



Equation (2-2) can now be used to calculate the blackbody spectra emanating from the two surfaces. As long as the slab absorbs virtually all of the incident radiation, the spectral distribution of this will not sensibly effect the spectra emanating from the two surfaces.

#### Incident Electromagnetic Pulse

There is interest in the interaction between an absorbing particle cloud and a strong electromagnetic pulse (EMP). Assume that the pulse shape is square and has a duration of 10 microseconds. This means that the predominant power in the pulse is in the frequency range of from 100 kHz to ~500kHz ( $300\text{m} > \lambda \approx 60\text{m}$ ). In order for the particles to be strongly absorbing at these and higher frequencies, the electrical conductivity should not be excessive, and the aspect ratio of the particle must be quite large. For example, if we were to select the 100 Angstrom radius particle of Fig. (2-1) for this purpose, its length would (from the E.Q.S. theory) have to be  $\geq 2\text{ mm}$  and the filament would have an aspect ratio of  $10^5$ . If this could be accomplished, and if the filaments were not agglomerated, this pulse would be strongly absorbed by a cloud of such particles. The scattering would be negligible. The temperature would, because of the small radius, be uniform throughout the volume of each particle.

### Vaporization and Melting

Under conditions of extremely intense incident illumination, particles composed of graphite will vaporize. Taking the vaporization temperature of graphite to be 4200 deg.C = 4473 deg.K, and using our first example (e.g. Fig. (2-1)) of a thin absorbing graphite fiber, we find that the intensity of an incident beam, of wavelength  $\lambda_0 = 10.6\mu$ , is 1300 watts/cm<sup>2</sup>.

Sufficiently thin iron particles will melt under much lower illumination levels than give rise to the vaporization of the above graphite fiber. This is because (1) the melting point of iron is lower (1808 deg.K vs 4473 deg.K), and (2) a sufficiently thin filament of iron has a much larger absorption efficiency factor. If we take the iron particle discussed in Section 2.6.2 as our example, and  $\lambda_0 = 10.6\mu$ , we find that an incident intensity of only 65 watts/cm<sup>2</sup> is required to melt the subject particle in a space environment.

We believe that, upon melting, the iron filament would (due to surface tension) form a spherical droplet. If this is correct, the spherical particle would no longer be highly absorbing and would cool and solidify. It is therefore not at all likely that any vaporization would occur in the case of the iron particle, except in the case of extremely high intensity levels.

### Ionization

For the vaporized graphite fiber, we would have (we believe) a gas of neutral carbon atoms. Assuming this to be the case, a field strength on the order of  $10^8$  to  $10^9$  volts/cm would be required to give rise to field ionization of the carbon atoms.

If either of the above particles were present in a gaseous environment (e.g. the atmosphere), field ionization of neutral molecules would occur at very much lower incident field strengths. This is due to the fact that very substantial enhancements of the incident E-field will occur very near the tips of the filaments. This interesting topic has been the subject of considerable in-house work at Panametrics. We might also note that, if conductive highly elongated particles were embedded in a solid dielectric, we predict that the incident intensity level required to initiate dielectric breakdown would be very substantially reduced.

#### Required Total Mass

Also of interest is the mass required to accomplish a given (dB) reduction in intensity of an incident beam. This calculation is straightforward in the case of a slab geometry: The total mass,  $M_{tot}$ , in the aggregate is

$$M_{tot} = A_c n r V_p \rho, \quad (2-30)$$

where  $A_c$ -illuminated cloud area,  $n$ -number density of particles ( $m^{-3}$ ),  $r$ -depth of the cloud (m),  $V_p$ -particle volume, and  $\rho$ -mass density of the material comprising the particle. We note that (1)  $n = \gamma / \sigma_{abs}$ , and (2) the one way (dB) attenuation (absorption) is given by  $(dB) = (2.3/10) \gamma r$ . Combining these and Eq. (2-28), we have the expression for the cloud mass per unit area required to cause a given (dB) reduction of an incident beam:

$$M_{tot}/A_c = (2.3/10) (dB) \rho V_p / \sigma_{abs}(\lambda_o). \quad (2-31)$$

## 2.8 Comments

The foregoing discussions relating incident electromagnetic energy, microscopic particle parameters, and the resulting thermal radiation were undertaken to provide a general understanding of the important processes as they relate to the physical parameters of the particles. The specific problems discussed were chosen for mathematical simplicity and ease of physical understanding. The standard texts (e.g. Ref's. 24 and 25) on Radiation Theory can be used in conjunction with the work of this Section in the solution of more complicated problems - and there are many.

The thermal emissivity of small particles has been discussed by Kattawar and Eisner<sup>26</sup> who also, we note with pleasure, discuss the quantum mechanical aspects of the emissivity for small particles. Pluchino<sup>27</sup> has computed emissivities (equal to  $Q_{abs}$  and less than unity) of small layered spherical particles. Our initial objective herein has been to address the question of  $\epsilon(\lambda) - Q_{abs}(\lambda) \gg 1$ . We also note, however, that Bohren and Huffman<sup>26</sup> have addressed this question and are in agreement with our conclusions that this circumstance is perfectly reasonable. They also provide some interesting historical aspects of the subject.

Other objectives of this Section have been to compute the appropriate radiation spectra for various specific particles of interest, and to determine means of computing the radiative properties of aggregates of broadband highly absorbing particles under conditions of intense illumination.

In connection with the work in this Section, we are most pleased to acknowledge many interesting discussions with J. Yos, Avco/Textron Systems Division, with F. Morgenthäler, Massachusetts Institute of Technology, and with I. Spain, Colorado State University; G. Kattawar, Texas A&M University, and with A. Pluchino, Aerospace Corporation.

## Appendix A

### SCATTERING BY CURVED CONDUCTIVE FIBERS

#### Preliminary Survey

All the numerical results obtained by Panametrics to the present time for scattering and absorption by conductive fibers have dealt with straight fibers. The question naturally arises then as to the effects of curvature of the fibers on the scattering and absorption efficiency.

A search of the literature reveals very little work on curved wires; all of that, with two exceptions, involving perfectly conducting wires. The curved, perfectly conducting wire was apparently first considered by Aharoni in 1946.<sup>28</sup> His equations were applied to circular loop and spiral antennas by Mei.<sup>12</sup> In 1956 Kouyoumjian considered back-scattering from perfectly conducting circular loops.<sup>11</sup> The two exceptions to the perfectly conducting case are the work of Philipson, who considered lossless dielectric rings,<sup>29</sup> and Acquista, who considered wavy cylinders.<sup>30</sup> In both of these latter cases, however, the scatterer was taken to be only a perturbation on its surroundings, so that a full integral equation approach was not required.

We have derived the integral equation for curved fibers, having finite conductivity, from first principles. The usual thin-wire analysis invariably assumes that the electric field can be expressed in terms of a current filament concentrated on the

axis of the fiber, and this is physically somewhat unsatisfactory especially when, as in the present case, we must work with both electric and magnetic fields at the surface of the fiber. We use instead an approach based on Huygen's principle,<sup>31</sup> which states that fields generated by the tangential components of  $E$  and  $H$  (distributed along the surface of the fiber) must precisely cancel the axial components of the incident electric field along the fiber axis.

This results in an equation involving integrals of the two unknown functions  $E$  and  $H$  along the fiber. Taking the thin-wire limit where fiber radius is very small compared to incident wavelength, the second of these integrals is fairly straightforward, and for good conductors is interpretable as the field due to a distribution of surface currents. The first integral behaves differently, however. The kernel reduces to a delta-function, resulting in a term in  $E$  at the field point of evaluation of the integral equation. Surface values of  $E$  and  $H$  can then be related by a surface impedance concept to finally give a pure integral equation for the current.

## The Integral Equation

When an incident electromagnetic field  $\underline{E}^{inc}$  illuminates a body in free space, the resulting fields are related by Huygens' principle, which states rigorously that<sup>31</sup>

$$\begin{aligned} \underline{E}^{inc}(\underline{r}) - (1/4\pi) \nabla \times \int d\sigma' \hat{k} \hat{n}' \times \underline{E}_+(\underline{r}') g(kR) \\ - (1/4\pi) \nabla \times \nabla \times \int d\sigma' i \hat{n}' \times \underline{H}_+(\underline{r}') g(kR) = \begin{cases} \underline{E}(\underline{r}) & \text{outside} \\ 0 & \text{inside} \end{cases} \quad (A-1) \end{aligned}$$

The left-hand side (LHS) of this equation consists of the sum of the electric fields due to the incident wave and surface distributions over the body of magnetic and electric dipoles, respectively.

Here

$$g(kR) = (1/kR) e^{ikR}, \quad R = |\underline{r} - \underline{r}'|, \quad (A-2)$$

where  $\underline{r}'$  and  $\underline{r}$  are the source point and field point, respectively.

Equation (A-1) states that the  $\underline{E}$  field is given by the LHS for all field points outside the surface. On the other hand, for all field points within the surface the LHS vanishes identically, i.e. the surface field distributions must precisely cancel the incident wave. This latter statement is sometimes known as the extinction theorem, or the extended boundary condition.



The extinction theorem is applied to the curved fiber, shown in Fig. A-1, as follows. Let  $a$  = fiber radius, and  $\rho(s)$  = radius of curvature as a function of position  $s$  along the axis of the fiber. We assume that

$$a/\rho_{\min} \ll 1 \quad (\text{A-3})$$

$$a/b \ll 1 \quad (\text{A-4})$$

$$ka \ll 1, \quad (\text{A-5})$$

i.e., the fiber radius is much less than the minimum radius of curvature, the fiber half-length  $b$ , and free space wavelength  $k = 2\pi/\lambda$ , respectively. We also assume the fiber to have moderate to large conductivity, so that axial currents will be induced and guided along the fiber.

Now requiring that the axial component of Eq. (A-1) vanish along the fiber axis gives

$$\begin{aligned} (1/4\pi) \hat{s} \cdot \nabla \times \nabla \times \int d\sigma' \hat{n}' \times \underline{H}_+(\underline{r}') g(kR) \\ + (1/4\pi) \hat{s} \cdot \nabla \times \int d\sigma' k \hat{n}' \times \underline{E}_+(\underline{r}') g(kR) = \hat{s} \cdot \underline{E}^{\text{inc}}(s). \end{aligned} \quad (\text{A-6})$$

Note that this equation is still exact, although we have only used a portion of the information available. The curl operators may be taken under the integral sign, because the field point need never approach the fiber surface.

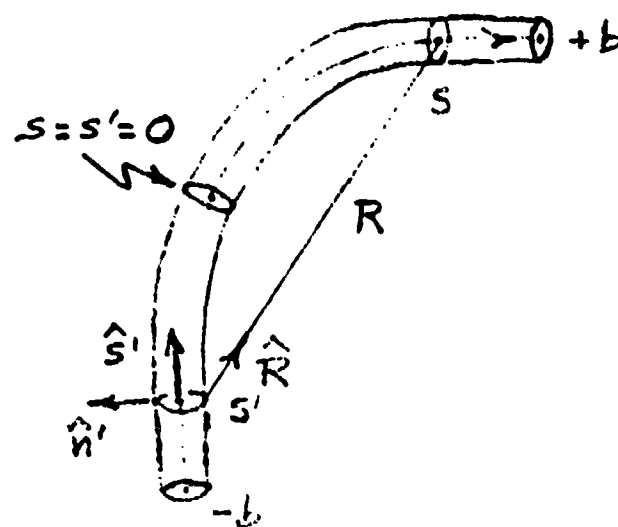


Figure A-1. Geometry of the Curved Fiber.

We suppose the magnetic field on the surface to be purely azimuthal, so that

$$\underline{H}_t(\underline{r}') = \hat{\phi}' H(s') , \quad (A-7)$$

$$\underline{n}' \times \underline{H}_t(\underline{r}') = \hat{s}' H(s') .$$

Using the identity  $\text{curl curl} = \text{grad div} - \text{div grad}$ , the first integrand of Eq. (A-6) takes the form

$$\begin{aligned} \hat{s} \cdot \nabla \times \nabla \times \hat{n}' \times \underline{H}_t(\underline{r}') g(kR) &= \hat{s} \cdot (\nabla \nabla - \nabla \cdot \nabla) \hat{s}' H(s') g(kR) \\ &= H(s') \hat{s} \cdot \nabla \nabla \cdot \hat{s}' g(kR) + k^2 (\hat{s} \cdot \hat{s}') H(s') g(kR) \\ &= H(s') (\hat{s} \cdot \nabla) (\hat{s}' \cdot \nabla) g(kR) + k^2 (\hat{s} \cdot \hat{s}') H(s') g(kR) \\ &= -H(s') [\partial^2 / \partial s \partial s' - k^2 (\hat{s} \cdot \hat{s}') g(kR)] , \end{aligned} \quad (A-8)$$

where in the last step we have used the formal notation  $\hat{s} \cdot \nabla = \partial / \partial s$  and  $\hat{s}' \cdot \nabla = -\partial / \partial s'$  for directional derivatives. The minus sign arises in the latter case because the primary variable has the form

$$\underline{R} = \underline{r}(s) - \underline{r}(s')$$

For the second integral of Eq. (A-6), the electric field on the surface is assumed to be purely axial, i.e.

$$\underline{E}_+(\underline{r}') = \hat{s}' E(s') . \quad (A-9)$$

Now

$$\begin{aligned} \hat{s} \cdot \nabla \times \hat{n}' \times \underline{E}_+(\underline{r}') g(kR) &= -\hat{s} \cdot (\hat{n}' \times \underline{E}_+) \times \nabla g \\ &= (\hat{n}' \times \underline{E}_+) \cdot (\hat{s} \times \nabla g) \\ &= E(s') (\hat{n}' \times \hat{s}') \cdot (\hat{s} \times \nabla g) \\ &= -E(s') (\hat{s} \cdot \hat{s}') (\hat{n}' \cdot \nabla g) \\ &= -E(s') (\hat{s} \cdot \hat{s}') (\hat{n}' \cdot R) k g' \\ &= -E(s') (\hat{s} \cdot \hat{s}') (a/R) k g' . \quad (A-10) \end{aligned}$$

Here in the fourth step we used the identity

$$(\underline{a} \times \underline{b}) \cdot (\underline{c} \times \underline{d}) = (\underline{a} \cdot \underline{c}) (\underline{b} \cdot \underline{d}) - (\underline{a} \cdot \underline{d}) (\underline{b} \cdot \underline{c})$$

then noted that the scalar product  $\hat{n}' \cdot \hat{s}$  vanishes identically under the azimuthal portion of the surface integration. In the last step above  $g'(kR) = dg/d(kR)$  and we have assumed that

$$\hat{n}' \cdot \hat{R} = a/R . \quad (A-11)$$

Note from Fig. A-1 that this equality only holds when  $|s-s'| \ll \rho$ , i.e., for points sufficiently close together along the axis that the curvature of the fiber has not come into play. No

approximation is involved here, however, because the integral is entirely negligible otherwise, as we will now see.

Using Eq. (A-10), the second term of Eq. (A-6) becomes

$$\begin{aligned}
 & -(k^2/4\pi) \int_0^{2\pi} a d\theta' \int_{-b}^{+b} ds' E(s') (\hat{s} \cdot \hat{s}') (a/R) g'(kR) \\
 & = -(k/2) (ka)^2 \int_{-b}^{+b} ds' E(s') (\hat{s} \cdot \hat{s}') (1/kR) g'(kR) \\
 & \approx (1/2) a^2 E(s) \int_{-\infty}^{+\infty} ds' [(s-s')^2 + a^2]^{-3/2} = E(s) . \quad (A-12)
 \end{aligned}$$

From the first step one notes that because  $ka \ll 1$  only that portion of the integral of order  $(1/ka)^2$  will contribute to the final result. Noting that

$$(1/kR) g'(kR) \approx -(1/kR)^3 = -(1/k)^3 [(s-s')^2 + a^2]^{-3/2} ,$$

for  $kR \ll 1$ , the remaining steps of Eq. (A-12) are straightforward.

Putting the results of Eqs. (A-8) and (A-12) back in Eq. (A-6) and carrying out the azimuthal integration, one finds that

$$(ia/2) \int_{-b}^{+b} ds' H(s') [\partial^2 / \partial s \partial s' - k^2 (\hat{s} \cdot \hat{s}')] g(s, s') = E(s) \\ = -\hat{s} \cdot \underline{g}_{inc}(s) . \quad (A-13)$$

We can express this result as an integral equation for total line current  $I(s)$  by writing

$$I(s) = 2\pi a i H(s) , \quad (A-14)$$

and introducing a surface impedance per unit length given by<sup>15</sup>

$$Z = -(\omega\mu/2\pi a k_f) J_0(k_f a) / J_0'(k_f a) . \quad (A-15)$$

Here  $k_f = (\omega^2 \mu \epsilon + i\omega\mu\sigma)^{1/2}$  is the complex propagation constant within the fiber.  $J_0$  is the Bessel function of the first kind, and we have assumed that both  $E$  and  $H$  within the fiber vary much more rapidly in the radial than the axial direction. This assumption is consistent with the requirement of moderate to large conductivity. Note, however, that if one were to represent  $I(s)$  as a Fourier expansion, then eventually the axial variations of such terms would dominate, with the result that  $k_f$  in Eq. (A-

15) would have to be modified.<sup>15</sup> That is, the surface impedance becomes dependent on the rate of axial variation of current when that rate is large.

The tangential E field can now be expressed as

$$E(s) = ZI(s) , \quad (A-16)$$

and using this result, along with Eq. (A-14), one finally obtains

$$\begin{aligned} (1/4\pi) \int_{-b}^{+b} ds' I(s') [\partial^2 / \partial s \partial s' - k^2(\hat{s} \cdot \hat{s}')] g(s, s') - ZI(s) \\ = -\hat{s} \cdot \underline{E}_{inc}(s) . \end{aligned} \quad (A-17)$$

Note that for straight fibers  $\hat{s} \cdot \hat{s}' = 1$  and this equation reduces to the usual formula.<sup>5</sup> Also for curved, perfectly conducting wires  $Z \rightarrow 0$  and one again finds the accepted formula.<sup>12</sup>

### Approximation for Special Fibers

For the general case, as described by the integral Eq. (A-17), it is clear that detailed numerical computations are required in order to obtain any explicit results. If the fiber axis has radius of curvature large compared to wavelength, or is made up of a zigzag series of straight line segments, however, then the absorption cross-section is readily approximated using earlier results.

First, consider the case where the fiber axis curves only slowly and is relatively long, compared with wavelength. Then we can use the infinite cylinder result to obtain the absorption cross-section per unit length  $\sigma_a/\ell$ , where this ratio is given by Eq. (1-20). Note that  $\sigma_a$  will be a function of position  $s$  along the curved fiber, in that  $\sigma_a$  depends on the angle  $\theta_0$  formed by the incident E vector and the local tangent to the fiber axis. The total absorption cross-section  $\Sigma_{abs}$  is then given by

$$\Sigma_{abs} = \int_{-b}^{+b} ds [\sigma_a(s)/\ell] . \quad (A-18)$$

It is now straightforward to obtain results for toroidal or C-shaped fibers, or other configurations meeting the slowly-curving limitation, by numerical integration of Eq. (A-18).

For a fiber made up of zigzag line segments, it is more appropriate to employ the quasi-static approximation to the absorption cross-section  $\sigma_{abs}$  as given by Eq. (1-29). We have



already seen by comparison with other computations that this formula is quite accurate for all fiber lengths provided the modified depolarization factor  $L'$  of Eq. (1-31) is used for  $k_0 l > 1$ .

Now for a fiber of  $N$  segments, having individual lengths  $l_n$ ,  $n = 1, 2, \dots, N$ , the total absorption cross-section  $\Sigma_{abs}$  is given simply by

$$\Sigma_{abs} = \sum_{n=1}^N \sigma_{abs}(l_n) \sin^2 \theta_n, \quad (A-19)$$

where the factor  $\sin^2 \theta_n$  (angle between incident  $E$  vector and  $n$ th segment axis) is included because the original Eq. (1-29) was specifically for broadside incidence.

It is useful to note that for both Eqs. (A-18) and (A-19) the cross-section  $\Sigma_{abs}$  is a linear sum of the cross-sections of individual segments. Because each such segment behaves precisely as a straight fiber under orientation averaging, one concludes that the orientation-averaged cross-section  $\overline{\Sigma}_{abs}$  for the curved fiber will be just equal to that of a straight fiber of the same total length.

## Appendix B

### TARGET OBSCURATION

In this section, taking into consideration both the diffuse cloud scattering properties and the beam extinction properties, one requires the optimum conditions for target obscuration from a mass efficiency standpoint, over a wavelength range where the theory is believed to be most accurate. It is appropriate to employ the quasistatic approximation, in which particles are assumed to be small in comparison with sensor wavelength.

Consider the situation when a target of (radar or optical) cross-section  $\sigma_T$  is partially concealed by a cloud of particles, the cloud having an incoherent cross-section  $\Sigma_c$ . Because of this incoherence, the cross-sections are additive and one has

$$\text{Observed cross-section} = \Sigma_c + \sigma_T e^{-2\gamma\tau} \quad , \quad (\text{B-1})$$

where  $\gamma$  and  $\tau$  are the decay constant and thickness of the cloud, respectively.

We now assume that the sensor cannot detect the target if

$$\Sigma_c \geq K\sigma_T e^{-2\gamma\tau} \quad (\text{B-2})$$

where  $K$  is a figure of merit, e.g. for  $K = 0.1$  the signal from the target would be 10 dB down in the "noise" of the cloud

return. The diffuse scattering from the cloud has earlier been computed to be  $32.33$

$$\Sigma_c = \frac{A_c}{\sqrt{3}} \left( \frac{k_o^2}{8\pi} \right) V_p \sigma_c' \quad (B-3)$$

where  $V_p$  is single-particle volume, the reduced conductivity is given by  $\sigma_c' = k_o \epsilon = \sqrt{\mu_o/\epsilon_o} \sigma_c$  (in terms of conductivity, or the imaginary part of the relative dielectric constant), and  $A_c$  is the geometrical cross-section of the cloud, or the sensor beam cross-section at the cloud, if the latter should be smaller. Using this result, and taking the equality in Eq. (B-2) then gives

$$\frac{A_c}{\sqrt{3}} \left( \frac{k_o^2}{8\pi} \right) V_p \sigma_c' = K \sigma_T e^{-2\gamma r} \quad (B-4)$$

The decay constant for the cloud is given by

$$\gamma = K \bar{\sigma}_{ext} \quad (B-5)$$

in terms of the number density of particles and the orientation-averaged extinction cross-section per particle. Assuming that absorption effects dominate, one has

$$\bar{\sigma}_{ext} \approx \bar{\sigma}_{abs} \approx \frac{\sigma_c' V_p}{3[1 + (L_e)^2]} \approx \sigma_c' V_p/3 \quad (B-6)$$

where in the next-to-last step the quasistatic approximation was employed, and in the last step we noted that optimum absorption will occur when

$$Ls'' = 4(a/\ell)^2 [ \pi(\ell/a) - 1 ] s'' \ll 1 \quad (B-7)$$

(L is the depolarizing factor). Note also that the total mass M of particles can be written

$$M = \rho V_p \pi A_c . \quad (B-8)$$

Employing Eqs. (B-5), (B-6) and (B-8) in Eq. (B-4), and taking the logarithm of the result determines the required mass to be

$$M = \frac{3\rho A_c}{2\sigma_c'} \ln \left[ \frac{2\sqrt{3}\pi}{k_o^2 V_p \sigma_c'} \left( \frac{K\sigma_T}{A_c} \right) \right] . \quad (B-9)$$

The quantities K,  $\sigma_T$  and  $A_c$  are prescribed by the logistics of the task at hand. Thus, to minimize M one first must seek a material with smallest possible value of the ratio  $\rho/\sigma_c'$ . In addition, it is desirable to obtain as large a value of the product  $k_o^2 V_p \sigma_c'$  as possible, in order to minimize the logarithmic term in Eq. (B-9).

For concreteness, suppose that

$$Ls'' = 0.1 ,$$

$$k_o \ell = 0.1 . \quad (B-10)$$

From Eq. (B-7) we then find that

$$a = \frac{0.01 (\ell/a)}{4 \sigma_c [\ln(\ell/a) - 1]} \quad (B-11)$$

This equation can be used to determine particle radius, once the length and conductivity are known. Typical particle design parameters can now be listed:

a) microwave region

$$\gamma = 3 \times 10^{-2} \text{ m}$$

$$\ell = 4.8 \times 10^{-4} \text{ m}$$

$$\sigma_c = 5 \times 10^6 \text{ mho/m}$$

$$a = 2.2 \times 10^{-8} \text{ m}$$

b) infrared region

$$\gamma = 3 \times 10^{-5} \text{ m}$$

$$\ell = 4.8 \times 10^{-7} \text{ m}$$

$$\sigma_c = 1 \times 10^4 \text{ mho/m}$$

$$a = 1.0 \times 10^{-8} \text{ m}$$

## Appendix C

### TAILORING OF PARTICLE PARAMETERS FOR SPECIFIC APPLICATIONS

(The discussion in this Appendix was done during 1985 as part of the effort of the first year of the Program. The theoretical and computational techniques, as described in Section 1 of the present report, have been significantly improved since that time. However, this Appendix is included in order to demonstrate the approach we have devised for this application.)

It is the purpose of this section to demonstrate the techniques by which the parameters (length, radius, and conductivity) of thin conductive fibers can be adjusted so that a cloud of these particles will have selected specified spectral characteristics. These characteristics are: (1) large absorption and small scattering, (2) large scattering and low absorption, and (3) transparency. Two frequencies were arbitrarily chosen for the cases to be analyzed. These are  $f_1 = 10^{10}$  Hz and  $f_2 = 10^{12}$  Hz, corresponding to wavelengths of 3 cm (microwave) and 300 microns (infrared).

The analyses to be discussed will be based on our "extended quasistatic model", the basis of which is described in Section 1.3. As demonstrated in Section 1, this analytical model produces results which are in surprisingly good agreement with the results obtained using the much more rigorous variational

technique of Section 1.2. To be more explicit, the quasistatic model can be used to calculate the absorption cross section over a very wide range of  $k_0 l$ , including  $k_0 l \gg 1$ . The scattering cross section computations resulting from the quasistatic model are valid only in the range  $k_0 l \leq \pi$ .

In all of the cases analyzed, the results of the quasistatic calculations are directly compared with the corresponding results of the variational technique. We find these comparisons to be quite remarkable.

## Constitutive Equations

In addition to the equations of Sections 1.2, 1.4 and 1.5, the following equations are utilized in the foregoing analyses:

Orientation-averaged absorption cross-section

(see Eq. 1-29):

$$\bar{\sigma}_{abs} = \left(\frac{1}{3}\right) \sigma_{abs} \quad (C-1)$$

Orientation-averaged scattering cross-section (see

Eq. 1-30):

$$\bar{\sigma}_{sca} = \left(\frac{1}{3}\right) \sigma_{sca} \quad (C-2)$$

High frequency depolarizing factor (see Eq. 1-31):

$$L' = 4 \left(\frac{k_o a}{\pi}\right)^2 \left[\ln\left(\frac{\pi}{k_o a}\right) - 1\right] \quad (k_o l \leq \pi) \quad (C-3)$$

The inclusion of the above equation permits extension of the calculation of absorption cross section well into the  $k_o l \gg 1$  regime. Due to this, we refer to the present theory as the "extended quasistatic theory."

In this treatment, we are using the Drude (free electron) model for the complex dielectric constant (Section 1.4) and the Fuchs model for the dependence of conductivity on particle dimensions, and we have purposely chosen frequencies  $\omega_1$  and  $\omega_2$  such that possible anomalies due to these do not appear. Also, for purposes of analysis, we can make the simplification  $\epsilon = \epsilon'$ . The computer program, however, does not utilize this simplification.



Absorb at 3 cm, Reflect at 300 microns

These criteria lead to the following mathematical statements:

At frequency  $\omega_1 = 2\pi \times 10^{10}$  Hz

$$\frac{\sigma_{sp}(1)}{\sigma_{sp}(2)} \ll 1 \quad (C-4)$$

Let  $\frac{\sigma_{sp}(1)}{\sigma_{sp}(2)} = .01 \quad (C-5)$

$$(L_s''(1))^2 \ll 1 \quad (C-6)$$

Let  $L_s''(1) = 0.1 \quad (C-7)$

Equation (C-7) ensures that the absorption cross section will be at its maximum value at frequency  $\omega_1$ , but will be reduced by a large factor at frequency  $\omega_2 = 2\pi \times 10^{12}$  Hz. Also, we know that the scattering cross section will be at least as great at  $\omega_2$  as at  $\omega_1$ . This will cause  $\sigma_{sca}(2)/\sigma_{abs}(2)$  to be large, which is what we seek at  $\omega_2$ .

From Eqs. (C-5), (C-7), (C-1), and (C-2), we obtain (with the appropriate definitive equations of Section 1.3) equations for the conductivity  $\sigma_0$ , radius  $a$  and length  $\ell$ :

$$\sigma_0 = \frac{\epsilon_0 c^2 (.03)^{2/3}}{\omega_1 a^2 \{10 [\ln(\frac{\ell}{a}) - 1]\}^{1/3}} \quad (C-8)$$

$$a = \frac{c (.03)^{1/3} (\frac{\sigma_0}{\omega_1})^{1/2}}{(\omega_1)^{1/2} [10 [\ell_n (\frac{\ell}{a}) - 1]]^{1/6} (\sigma_0)^{1/2}} \quad (C-9)$$

$$\ell = 2a \cdot 10 \left\{ [\ell_n (\frac{\ell}{a}) - 1] \left( \frac{\sigma_0}{\omega_1 \epsilon_0} \right) \right\}^{1/2} \quad (C-10)$$

when Eqs. (C-8) and (C-9) are equivalent, i.e., we can choose a conductivity and solve for a, or choose a radius, a, and solve for the conductivity  $\sigma_0$ . We will do the former. Knowing both a and  $\sigma_0$ , we then calculate the length from (C-10). Note that the term in square brackets in (C-8), (C-9), and (C-10) is very insensitive to large variations in  $(\ell/a)$ . This is especially true when it is raised to fractional powers in (C-8) and (C-9). Therefore, we can come quite close to the desired results if we simply let  $[ ] = 2.5$ . This permits direct estimation of a and  $\ell$ , given a preselected value of  $\sigma_0$ .

Table I

Cond = 1.00E+04	Radius = 8.68E-06
Length = 3.71E-03	$k_0(1)\ell/2 = 3.88E-01$
Cond = 1.00E+05	Radius = 2.75E-06
Length = 3.71E-03	$k_0(1)\ell/2 = 3.88E-01$
Cond = 1.00E+06	Radius = 8.68E-07
Length = 3.71E-03	$k_0(1)\ell/2 = 3.88E-01$
Cond = 1.00E+07	Radius = 2.75E-07
Length = 3.71E-03	$k_0(1)\ell/2 = 3.88E-01$
Cond = 1.00E+08	Radius = 8.68E-08
Length = 3.71E-03	$k_0(1)\ell/2 = 3.88E-01$
Cond = 1.00E+09	Radius = 2.75E-08
Length = 3.71E-03	$k_0(1)\ell/2 = 3.88E-01$

The above procedure leads to sets of permissible parameter values, as exemplified in Table I. Substitution of the various parameter sets into the computer program yields graphs such as shown in Fig. C-1. Since these graphs are identical over the wavelength range 300 microns to 3 cm, only one is shown. This figure is representative of a fairly highly conducting metal (bulk conductivity =  $10^7$  mho/m). The relaxation time  $\tau$  is that of copper.

From Fig. C-1, we see that (1) indeed, the absorption cross section peaks at very nearly the wavelength  $\lambda_1 = 3$  cm, (2) that, in the case of absorption, the extended quasistatic theory is in excellent agreement with the variational theory for wavelengths greater than about 50 microns, and (3) the scattering as calculated from both theories is in excellent agreement when  $k_0 \ell \lesssim 1$ .

We further conclude that the mathematical "design" procedure demonstrated in this sub-section, although not analytically exact, provides good parametric sets for the solution of the stated problem, since the objectives are met at the two specified wavelengths.

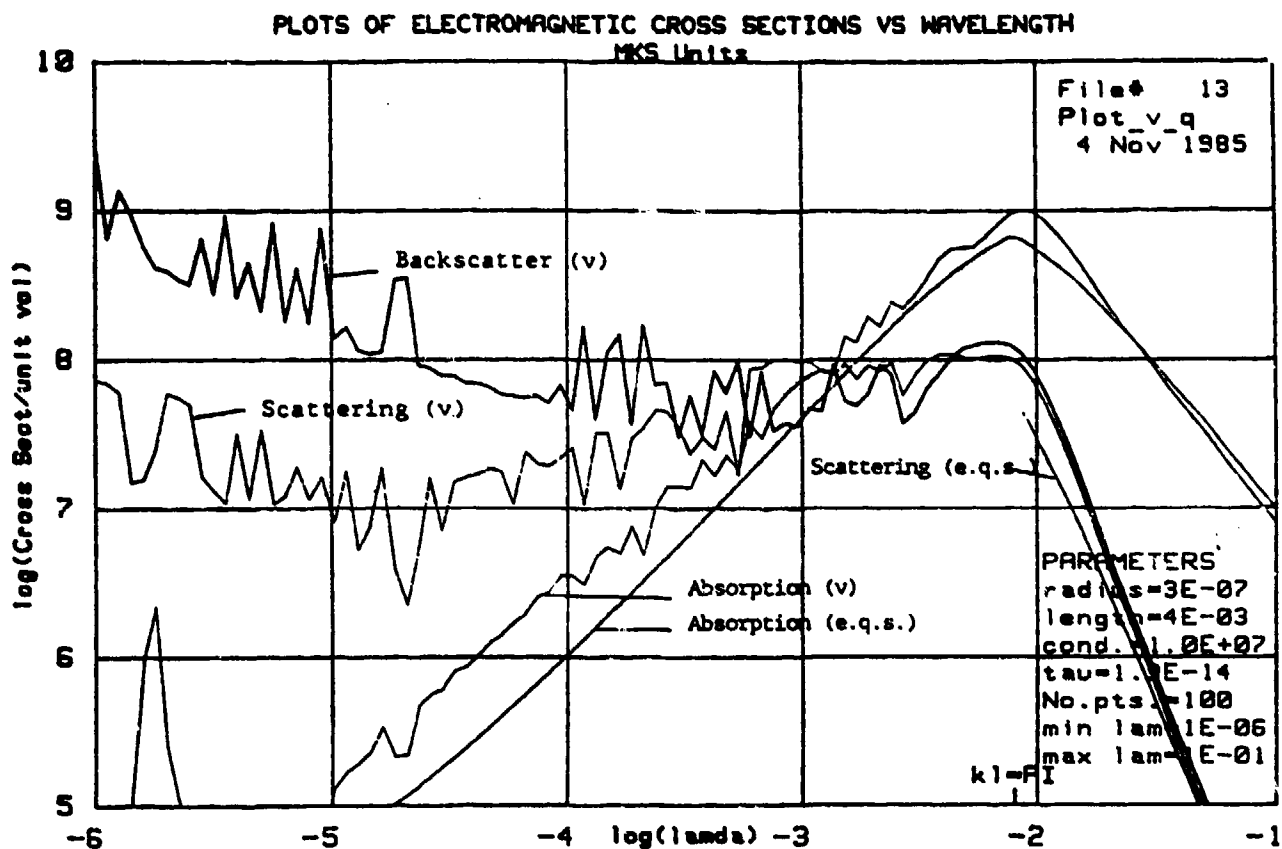


Figure C-1. An example of predominant absorption at  $\lambda = 3$  cm and predominant scattering at 300 microns. v = variational technique; e.q.s. = Extended Quasistatic Theory.

### Absorb at 3 cm, Absorb at 300 microns

We have quite different criteria for this problem as compared with the preceding problem. Here, we wish to have a very highly absorbing cloud which has low scattering cross section.

In this case, the cloud scattering cross section  $\Sigma_c$ , is given by

$$\Sigma_c = A_c \left( \frac{\sigma_{scat}}{2 \cdot \sigma_{abs}} \right) , \quad (C-11)$$

where  $A_c$  = projected area of the cloud or that portion thereof which occupies the solid angle of the incident beam.

Obviously, we wish to make the absorption cross section of the particle much larger than its scattering cross section. This must be true over at least the wavelength range from 300 microns to 3 cm.

The above considerations lead to the following mathematical criteria:

- (1) In order to have maximum absorption over the specified wavelength range, we want  $L_e''(1) \ll 1$  and  $L_e''(2) \ll 1$ . This means that the particles should be very thin and (perhaps) not too highly conducting.

- (2) Since, under the above conditions,  $\bar{U}_{scat} \sim k_0^2 V_p^2 \sigma_0^2$  and  $\sigma_{abs} \sim V_p \sigma_0$ , the ratio  $(\bar{U}_{scat}/\bar{U}_{abs})$  is proportional to  $k_0^2 V_p \sigma_0$ . Therefore, in order to maintain high cloud absorption and low cloud scattering, we wish to keep the product  $V_p \sigma_0$  low (we have no control over  $k_0$ ).

A little bit of experimenting with the extended quasistatic (EQS) computer program yields appropriate sets of parameters. The parameter set corresponding to minimal total mass is  $a = 100$  Angstroms,  $l = 100$  microns, and  $\sigma_0 = 10^6$  mho/m as the bulk conductivity. The results of using these parameters in the EQS and variational codes are shown in Fig. C-2. One can trade off a larger radius for a lower conductivity and achieve similar results, but with a somewhat higher ratio of  $(\bar{U}_{scat}/\bar{U}_{abs})$ .

Note again the remarkable agreement between the computations based on the two independent theories!

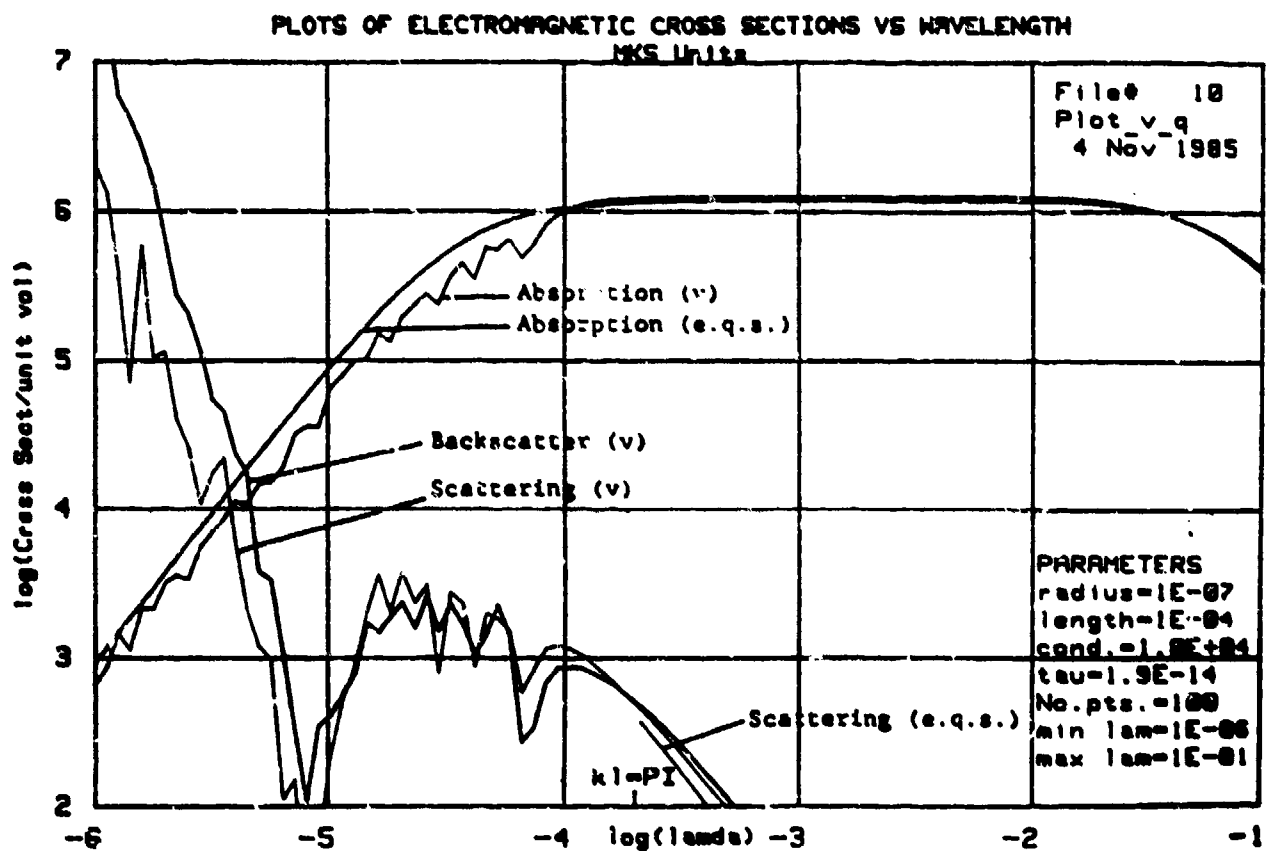


Figure C-2. An example of broadband absorption at 3 cm and 300 microns. v = variational technique; e.q.s. = Extended Quasistatic Theory.

## Reflecting Modes

It is easy to design particles having very low absorption and relatively high scattering. Experience has shown us that if, for example, we choose a highly conducting metal such as copper or aluminum, and select a radius of one micron or greater, the particle will be essentially completely reflecting for at least all wavelengths below 30 microns. We can tailor the scattering cross section to become proportional to  $\omega^4$  at wavelengths significantly below that for which  $k_0 \ell \approx 1$ , which of course, represents Rayleigh scattering from "perfectly conducting" wires. Thus, the aggregate of particles can easily be made to be reflecting at one wavelength and essentially transparent at some (significantly) lower wavelength. Chaff clouds behave in this way.



### Transparent at 3 cm, Absorb at 300 Microns

In this case, we want the scattering cross section to be much lower than the absorption cross section at all wavelengths under consideration. The requirements due to this and the transparency criterion at  $\omega_1$  are given below:

- (1) Make  $V_p \sigma_0$  as small as possible, consistent with the other criteria.
- (2) Make  $L_s'' = 1$  at  $\omega_2$ .
- (3) Make  $k_0 \ell < 1$  at  $\omega_2$ .

Application of these criteria leads to the parameters listed in Figure C-3. Note that, at  $\lambda = 3$  cm, the absorption is three orders of magnitude lower than that at  $\lambda = 300$  microns. The scattering throughout the  $\omega_1$  to  $\omega_2$  spectrum is much lower than the absorption.

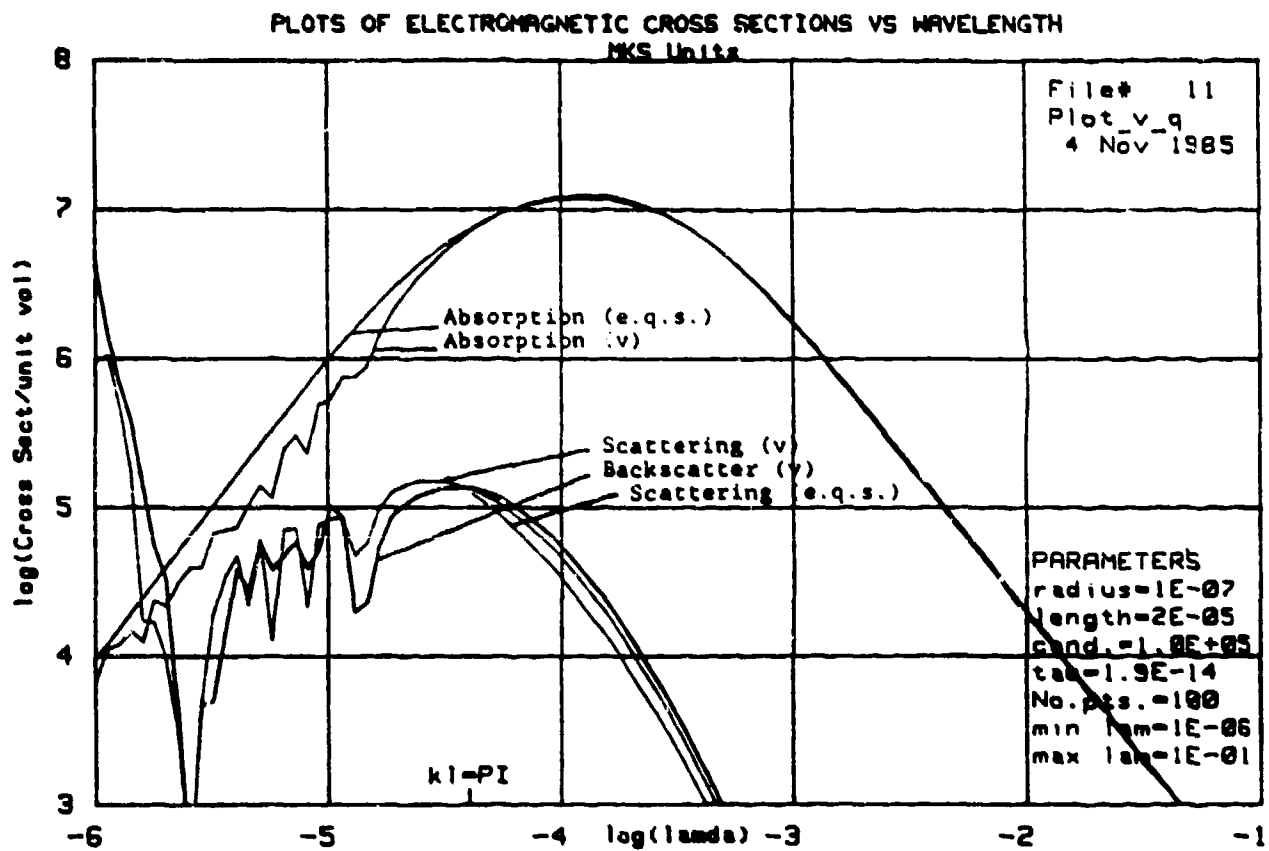


Figure C-3. An example of transparency at 3 cm and predominant absorption at 300 microns.

## Comments Relative to Particle Parameter Tailoring

- (1) Our extended quasistatic treatment provides a very useful tool in the design of particles for specified applications. In some instances, the EQS theory does not yield accurate quantitative data and should be used primarily as a first step to be followed by the full computation using our Variational method.
- (2) The calculation of scattering cross sections using the EQS theory is limited to the range  $k_0 \ell / 2 \leq 1$ , so the variational technique must be employed beyond that point.
- (3) We have included backscatter cross section computations in Figures C-1, C-2 and C-3 for those applications that require this.
- (4) Within the bounds of present technology, it is possible to create particle parameters that could provide useful spectral characteristics over a wide wavelength range.

## REFERENCES

1. H.C. Pocklington, Camb. Phil Soc. Proc. 2, 324 (1897).
2. E. Hallén, Nova Acta Regiae Soc. Sci. Upsaliensis 11, 1 (1938).
3. J.H. Van Vleck, F. Bloch and M. Hamermesh, J. Appl. Phys. 18, 274 (1947).
4. C.T. Tai, J. Appl. Phys. 23, 909 (1952).
5. R.S. Cassedy and J. Fainberg, IRE Trans. Antennas and Prop. 8, 1 (1960).
6. J.H. Richmond, Proc. IEEE 53, 796 (1965).
7. J.H. Richmond, IEEE Trans. Antennas and Prop. 15, 802 (1967).
8. L.N. Medgyesi-Mitschang and C. Eftimiu, IEEE Trans. Antennas and Prop. 30, 628 (1982).
9. C.-L. Chen, Radio Sci. 3, 585 (1968).
10. L.C. Shen, T.T. Wu and R.W.P. King, IEEE Trans. Antennas and Prop. 16, 542 (1968); L.C. Shen, IEEE Trans. Antennas and Prop. 18, 112 (1970).
11. R.G. Kouyoumjian, Appl. Sci. Res. B 6, 165 (1956).
12. K.K. Mei, IEEE Trans. Antennas and Prop. 13, 374 (1965).
13. O. Einarsson in Electromagnetic and Acoustic Scattering by Simple Shapes, J.J. Bowman et al., Eds. (North-Holland Publishing Co., Amsterdam, 1969), p. 472.
14. D.S. Jones, The Theory of Electromagnetism (Pergamon Press, England, 1964), pp. 269 ff.
15. J.R. Wait, Electr. Lett. 15, 659 (1979).

# REFERENCES (cont'd)

16. J.R. Wait, Can. J. Phys. 33, 189 (1955); 43, 2212 (1965).
17. M.A. Ordal et al., Appl. Opt. 22, 1 (1983).
18. F. Wooten, Optical Properties of Solids (Academic Press, New York, 1972).
19. K. Fuchs, Proc. Camb. Phil. Soc. 34, 100 (1938).
20. R.B. Dingle, Proc. Roy. Soc. A201, 545 (1950).
21. C. Kittel, Introduction to Solid State Physics (John Wiley and Sons, New York, 1956), Chap. 10.
22. P.C. Waterman, J. Opt. Soc. Am. 71, 410 (1981).
23. N.E. Pedersen, J.C. Pedersen and P.C. Waterman, Final Report on Theoretical Study of Single and Multiple Scattering by Cylinders, Panametrics' Technical Report (April 1985).
24. R. Siegel and J. Howell, Thermal Radiation Heat Transfer Second edition; (McGraw-Hill, New York, 1981).
25. M. Bramson, Infrared Radiation (Plenum Press, New York, 1968).
26. G.W. Kattawar and M. Eisner, Appl. Opt. 9, 12 (1970).
27. A.B. Pluchino, Appl. Opt. 20, 17 (1981).
28. J. Aharoni, Antennae - An Introduction to Their Theory (Clarendon Press, Oxford, 1946) pp. 133-135.
29. L.L. Philipson, IRE Trans. Ant. Prop., 6, 3 (1958).
30. C. Aquista, Effects of axis wander on scattering by thin tenuous cylinders, Proc. 1980 Chemical Systems Laboratory Scientific Conference on Obscuration and Aerosol Research (June 1983), p. 17.
31. P.C. Waterman, Phys. Rev. D. 3, 825 (1971).